Summer 1999

Jet Stability and Noise Computations Using Direct Numerical Simulation

Farouk Owis
Old Dominion University

JET STABILITY AND NOISE COMPUTATIONS

USING DIRECT NUMERICAL SIMULATION

by

Farouk Owis
M.Sc. June, 1993, Aerospace Engineering Department
Cairo University, Egypt

A Dissertation Submitted to the Faculty of
Old Dominion University in Partial Fulfillment of the
Requirement for the Degree of

DOCTOR OF PHILOSOPHY

AEROSPACE ENGINEERING

OLD DOMINION UNIVERSITY
August, 1999

Approved by:

(Director) Ponnampalam Balakumar

Osama A. Kandil

Oktay Baysal

Fang Hu

ABSTRACT

JET STABILITY AND NOISE COMPUTATIONS USING DIRECT NUMERICAL SIMULATION

Farouk Owis
Old Dominion University
Director: Prof. P. Balakumar

The computations of axisymmetric jet noise with symmetric disturbances are investigated using the direct numerical simulation of the unsteady compressible Navier-Stokes equations. High order accurate numerical schemes are employed for the solution of the governing equations. The investigation shows that MacCormack schemes with operator splitting and minimum dispersion error can be used to predict noise radiated from subsonic and supersonic jets with low and high Reynolds numbers. In addition, different kinds of nonreflecting boundary conditions are used at the inflow and outflow boundaries. These boundary conditions include characteristic boundary conditions, buffer domain technique and perfectly matching layer method. The results indicate that the perfectly matching layer method is causing minimum wave reflections at the boundaries and this method is computationally less expensive than the other boundary conditions.

The computations are carried out for two and three-dimensional axisymmetric jets. Five cases for two-dimensional jets at different Mach numbers and Reynolds numbers are presented. The characteristics of the sound source in the near field are computed and the results show a good agreement with the observations. Moreover, a method is developed to compute the noise in the far field using the linearized Euler equations. The results computed in the far field agree with those obtained using Navier-Stokes equations.

ACKNOWLEDGMENTS

First and foremost, I would like to express my deep thanks and sincere appreciation to my advisor, Prof. P. Balakumar, for his strong support and profound guidance through the duration of this research. His high academic standards and goals, as well as his genuine interest in science were both very challenging and motivating, and also of a significant impact on the present work. I am truly thankful for his valuable advice and encouragement, which provided a constant source of inspiration.

Special thanks to the members of my dissertation committee, Prof. Osama Kandil, Prof. Oktay Baysal in the Aerospace Engineering Department for their valuable comments and for reviewing this dissertation. I would like to acknowledge Prof. Fang Hu at the Mathematical Department for being a member of my defense committee and for his considerable help in applying the matching layer boundary condition developed by him. It is my pleasure to thank Prof. Eli Turkel and Prof. E. Hayder for their guidance and for submitting me necessary articles.

I acknowledge the Aerodynamics and Acoustics branch at NASA Langley for funding this project under grant number NAG-1-1677. Many thanks to Michael Macaraeg at NASA for supporting this research.

I would like to give special thanks and acknowledgement to my parents and my wife for their support at all times. I am really indebted to them in every possible way.

NOMENCLATURE

English Symbols

Cp	Specific heat at constant pressure
E	Total internal energy
f	Frequency
k	Thermal conductivity
M_j	Jet Mach number
n	Azimuthal wavenumber
p,P	Pressure
Pr	Prandtl number
R	Gas constant
r	radius
Re	Reynolds number
St	Strouhal number
T	Temperature
t	Time
u,U	Axial velocity
u'	Axial velocity disturbance
v,V	Radial velocity
w	Azimuthal velocity
x	Axial distance

Greek Symbols

α	Axial wavenumber
β	Jet temperature ratio
δ_2	Momentum thicknes
ε	Disturbance amplitude at the inflow
γ	Specific heat ratio
η	Jet mean temperature
λ	Characteristic waves

ν Kinematic viscosity

μ Viscosity

ω Angular frequency

σ_x, σ_y Absorption coefficients for the matching layer

θ Azimuthal angle

Θ Dilatation

Vector Quantities

F Axial flux

G Radial flux

H Azimuthal flux

Q Conservative flow variables

S Source term

σ Stress tensor

Subscripts

avg Average

d Disturbance

dist Disturbance

j Jet conditions

t time derivative

∞ Jet freestream conditions

Superscripts

trans Transpose

* Dimensional quantities

CONTENTS

LIST OF FIGURES

Page

LIST OF TABLES

Page

Chapter 1
Introduction

Recent efforts to develop a supersonic civil transport plane and the proposed stringent community noise requirements have led to a resurgence of interest in the prediction and suppression of noise radiated by jets. Considerable attention has been focused on developing reliable prediction methods, especially for the dominant supersonic jet component.

Noise prediction has been around for more than 45 years in the form of acoustic analogy theory where the equations of fluid motion are configured as the usual acoustic wave operator with remaining terms acting as an analogous source. Much effort has been devoted to transform this source term, which includes nonlinear hydrodynamic terms and other terms involving viscous and thermal effects, into a form which is integrable. The most popular form is the one originally proposed by Lighthill (1952) which has successfully predicted global features such as the scaling of total intensity with Mach number, jet diameter and to some extent sound spectrum and directivity. The acoustic analogy yields prediction of jet noise if the source of the sound is known a priori. Detailed experimental measurements of the source and its retarded time would be very difficult. Thus simplifying assumptions about the forms of the source terms have been used to predict scaling laws and the directivity of the acoustic field.

Experiments have shown that the sound radiated from the jet is greatest within 4-6 diameters downstream and then it decays through a transition region. This region is characterized by large vortical structures and the size of these structures is of the flow geometry size. For this reason, the unsteady flow equations can be solved in the near field using direct numerical simulation to provide the sound source for acoustic computations of the far field noise.

The format of this dissertation is based on the *Journal of Fluid Mechanics* and it was typeset in Word 97 by the author.

According to Laufer (1973), the flow of the jet mixing layer during the development of the large scale structures may be divided into the following four regimes.

i) Mixing layer instability regime, where the periodic oscillations are developed.

ii)Vorticity concentration regime, where the vorticity tends to be concentrated in separated regions as a result of increasing the amplitude of oscillations.

iii)Formation of vortex ring structures: the concentrated vorticity regions display their ring-like structure as the vortex scale approaches the jet diameter.

iv)Vortex interaction and pairings: the vortex rings interact with each other and they pair to double the size of the vorticity concentration region and to double the spacing between adjacent vorticity concentration. The rate of vortex pairings determines the spreading rate of the layer and thus the length of the potential core. The pairing process is believed to be the key for understanding the turbulent mixing process and the noise generation as well.

Jet noise computations can be divided into three strategies as discussed by Lighthill (1992):

i) The computational domain includes only the near field region without attempting to resolve the acoustic waves. Subsequently an acoustic analogy is solved with the source terms that have been determined from the near field computations.

ii) The computational domain includes the near field region and, to a small extent, the acoustic region. The acoustic far field is predicted by solving the wave equation given boundary data from the near field.

iii) The computational domain includes both the near field and a significant portion of the far field. Both regions are solved using the compressible Navier-Stokes equations.

Lighthill (1992) suggests that the first strategy is suitable for low Mach numbers where the computations do not rely on resolving the acoustics. The second strategy relies on the so-called Kirchhoff surface theory to predict the far field. The third strategy has many difficulties for subsonic flows due to the large extent of the acoustic field compared

to the flow field, the errors from the numerical discretization; and the application of accurate boundary conditions at an artificial computational boundary. It may be that all three categories are useful for their own subset of problems. In the present study, the second and third strategies are adopted to compute the jet noise for subsonic and supersonic flows with detailed investigation of the numerical schemes and the numerical errors associated with these schemes. In addition, the boundary treatment is studied for different boundary conditions to ensure minimum wave reflections from the boundaries.

Due to the nature, characteristics and objectives of aerodynamic sound computation problems, which are distinctly different from those commonly encountered in aerodynamic problems, fluid dynamic methods cannot solve aeroacoustic problems. Scott (1993) identified five specific characteristics as distinguishing features between computational fluid dynamics and computational aeroacoustics:

i) The wide range of frequency scales encountered in the audible frequencies, which range from 50Hz to 20kHz with the most sensitive being near 1kHz.

ii) Pressure and density fluctuations are five orders of magnitude smaller than those of the flow field fluctuations.

iii) Dissipation and dispersion properties of numerical schemes, which tend to damp the acoustic oscillations or to generate non-physical disturbances, need to be minimal.

iv) Long time solutions for resolving tens of cycles of the lowest frequency of interest or long wave length features.

v) Boundary conditions for the unsteady flow, which will also permit accurate representation of the incoming and outgoing acoustic phenomena without generating non-physical reflections.

Thus evaluation of the sound source using the direct numerical simulation of Navier-Stokes equations requires using numerical techniques with minimum distortion and diffusive characteristics. The numerical errors get worse for high Reynolds number flow simulation. Typically, free shear layers of interest have very high Reynolds numbers.

Therefore high order accurate numerical schemes with minimum dissipation and dispersion errors are needed with a special attention to the boundary treatment.

1.1 Motivation

This research is motivated by the need to understand the mechanisms of jet development into turbulence and the noise generation process in jet mixing layers. Recently, there have been many studies on supersonic and subsonic jet noise radiation, but the role of large scale structures and the vortex pairing process on the mixing layer noise need more investigation. Understanding the noise generation process represents the key to find noise suppression methods.

The sound propagation and noise computations in the far field are issues that need to be investigated in this work. Several attempts have been directed toward calculating the radiation field generated by large-scale coherent structures. Tam and Morris (1980) adopted the view that large-scale structures can be represented by instability waves. They calculated the noise produced by linear instability waves. Mankbadi (1984) calculated the radiation field with coherent structures represented as nonlinear instability waves interacting with the mean flow and random turbulence. Lighthill's theory is then used to obtain the corresponding sound field. Some of these predictions are consistent with observations; however, the predicted directivity of sound seems to be in fair agreement with observations.

Accurate computations of the jet noise and the sound radiated from the turbulent mixing layer will help to develop suppression methods of the jet noise. One of the objectives of this research is developing an efficient numerical tool to predict the jet noise. Development of such numerical method requires using numerical schemes with high accuracy and minimum dispersion and dissipation errors. Part of this research is devoted to investigate the numerical schemes used for computational aeroacoustics and to study the effect of the boundary treatment on the solution of the unsteady flow equations. The numerical boundaries can generate spurious waves that render the computed solution entirely unacceptable. Several boundary conditions have recently been proposed for computational aeroacoustics. These boundary conditions include characteristic methods,

asymptotic analysis of the governing equations, buffer domain technique and matching layer. A comparison between these methods is needed in the current research to find out a boundary treatment that will allow the acoustic waves to pass with minimum reflections.

1.2 Objectives

The development of high-speed civil transport plane relies on suppressing the noise radiated from jet mixing layer. Suppressing jet noise requires understanding the mechanisms of noise generation process and investigating the roles of large-scale structures on noise radiation. Hence, accurate prediction tools for the jet noise are needed to estimate the sound source in the near field and to compute the noise in the far field. Development of such numerical methods for jet noise computations requires using numerical schemes with minimum dissipation and dispersion errors. In addition, a special attention to the boundary treatment is needed to ensure that the boundaries do not reflect nonphysical waves.

The objectives of the current work are developing efficient numerical tools with nonreflecting boundary conditions to compute the jet noise for subsonic and supersonic jets with low and high Reynolds numbers. Direct numerical simulation of the unsteady Navier-Stokes equations is used to compute the unsteady flow quantities. Such computations require calculating the jet mean flow and analyzing this flow using the linear stability theory. Hence, the objectives of the current work are listed as follows:

i) computing the jet mean flow using the steady boundary-layer equations.

ii) using the linear stability analysis to compute the most unstable frequency, the subharmonics, the associated eigenfunctions with these frequencies and the distance required for jet flow transition into turbulence.

iii) investigating the accuracy of MacCormack schemes for jet noise computations

iv) studying the effect of the different boundary treatment on the characteristics of the acoustic waves.

v) computing the near field source of the jet noise and part of the acoustic field using the unsteady compressible Navier-Stokes equations.

vi) developing a numerical method to compute the noise in the far field.

1.3 Present work

The present work focuses on developing numerical tools with nonreflecting boundary conditions to compute the noise radiated from subsonic and supersonic jets with high and low Reynolds numbers. With the availability of supercomputers, direct numerical simulation of unsteady compressible Navier-Stokes equations has become the tool to estimate the flow fluctuations and the acoustic field for high and low Reynolds number simulations. Direct numerical simulation is used to obtain the physical details of the flow.

In particular, chapter 2 contains a survey of the literature related to the investigation of the noise radiated from subsonic and supersonic jets. Direct numerical simulation of subsonic and supersonic jets are reviewed including the numerical boundary treatments and the numerical schemes used in jet flow simulations. In addition, examination of the noise computation methods in the far field is presented as well as experimental studies on the acoustics of mixing layers.

The jet mean flow and its variation with the axial distance needs to be precisely known in order to compute the disturbance of the flow variables. Direct numerical simulation of the compressible Navier-Stokes equations provides a good and accurate solution of the mean flow but this method will require a greater computational effort than that of the perturbed flow of interest. Instead, the boundary-layer equations are used to compute the jet mean flow as described in chapter 3.

In chapter 4, the linear stability theory analysis, which is needed in the computations of the sound field, is introduced. Global and local methods are described to solve the linearized Navier-Stokes equations. Calculation of the growth rate, eigenfuctions of the linearized equations and N-factor are presented in this chapter.

In chapter 5, discussion of the numerical simulation method and the mathematical formulations of the governing equations are described. The accuracy of the numerical schemes and the different boundary treatment methods are discussed.

In chapter 6, the results of two-dimensional axisymmetric jet simulations are presented. First, the results are shown for two-dimensional subsonic and supersonic jets for low and high Reynolds numbers. Computations of the mean flow and linear stability analysis for these jets are discussed. In addition, a comparison between MacCormack type schemes is presented as well as discussion of outflow boundary treatment results.

In chapter 7, the results of three-dimensional axisymmetric jet are presented. The computations are done for subsonic jet and the computational domain is limited to the near field. The results are analyzed using Fourier transform.

In chapter 8, the noise computations in the far field using the linearized wave equation are covered. The results are compared with those obtained by the direct numerical simulation of extended computational domain. Finally, chapter 9 concludes the present study with general remarks and recommendations for future investigations.

Chapter 2

Literature Review

2.1 Introduction

Many studies have been directed toward the jet noise computations and the stability of mixing layers. These studies include development of numerical methods and boundary conditions for computational aeroacoustics. Other efforts are directed toward using the direct numerical simulation of the governing equations as a tool to predict the jet noise rather than relying on the approximate and less costly methods such as large eddy simulation and the parabolized stability, which can only resolve large-scale structures.

More attention has been focused on evaluating the acoustic field either using the acoustic analogy method to avoid the discretization errors of the numerical schemes or using the linearized wave equation. The sound source is obtained in the near field using the direct numerical simulation and submitted to the wave equation as a Direchliet boundary condition. Other methods use the Kirchhoff's surface to integrate the sound source in the far field. Evaluation of these methods is introduced in a subsequent section. In addition, experimental studies have been conducted to measure and study the sound generated by high and low Mach number mixing layers. Some of these studies are reviewed in a subsequent section.

2.2 Theoretical and Numerical Studies

2.2.1 Numerical Schemes for Computational Aeroacoustics

Aeroacoustic problems are time dependent. So, a consistent, stable and convergent high order scheme does not guarantee a good quality of the numerical wave

solution. Analysis of Euler equation reveals that these equations support three types of waves, namely, acoustic, entropy and vorticity waves. Acoustic waves are isotropic, nondispersive, nondissipative and propagate with the speed of sound. Entropy and vorticity waves are nondispersive, nondissipative and highly directional. They propagate in the direction of the mean flow with the same speed. Finite difference equations used in CFD are dispersive, anisotropic and even highly dissipative (sometimes artificial dissipation terms are added to improve numerical stability).

Recently, many high-order finite difference schemes were suggested for the computational aeroacoustics area. These schemes support wave solutions, which have the same characteristics as those of Euler equations. Gottlieb and Turkel (1976) proposed a dissipative two-four scheme for time dependent problems. The scheme is an extension of the conventional second order accurate MacCormack scheme and it uses the operator splitting technique alternating the operators symmetrically in order to maintain the accuracy. One-sided differences are used in the scheme to add dissipation to stabilize the scheme. This scheme has been used successfully on a wide range of aeroacoustic problems. Farouk, et al (1991), Ragab and Sheen (1991), and Sankar, et al (1993) have evaluated this scheme for studying nonlinear instability problems in shear layer and aeroacoustic applications. The two-four scheme has been extended to sixth-order spatial accuracy by Bayliss, et al (1985). In addition, Viswanathan and Sankar (1995) have extended the two-four scheme to fourth-order time accuracy.

Based on the same idea of the two-four and two-six schemes, Hixon (1997) developed a new family of MacCormack schemes for aeroacoustic applications. The accuracy of these schemes has been improved by adding one point on the opposite side to each of the one sided differences. Thus, the dispersion and dissipation errors are minimized for each one sided difference. By this way, the 4/2 scheme developed by Gottlieb and Turkel has been optimized to 4/4 scheme, which has fourth order accuracy in space and fourth order dissipation in each step. In addition, Hixon improved the

accuracy of the 6/2 scheme to 6/4 and optimized the dispersion relation preserving scheme.

Lele (1992) developed compact finite difference schemes with spectral like resolution. A family of compact schemes with higher accuracy is derived through matching Taylor series coefficients of various orders. The derivatives are calculated implicitly using tridiagonal or pentadiagonal systems. These schemes are a generalization of the well-known Pade scheme.

A new optimized fourth-order finite difference scheme is introduced by Tam and Webb (1992). This scheme has the same dispersion relation of the governing partial differential equations and it is called dispersion relation preserving scheme. The dispersion relation is a functional relation between the angular frequency of the waves and the wave numbers of the spatial variables. This relation is usually obtained by taking the space and time Fourier transforms of the governing equations. The dispersivness, damping rate, isotropy or anisotropy, group and phase velocities of the waves are all determined by the dispersion relation. Hence, the dispersion relation preserving scheme is constructed so that the Fourier transform of the governing equations is preserved. In other words, the finite difference scheme has nearly the same Fourier transform in space or time as the original partial derivatives. In addition, an explicit time integration is developed based on Taylor series expansion and Laplace transform of the time discretization.

Another class of compact finite difference schemes is derived by Hixon (1998) to obtain higher order accuracy while using a very small stencil size. These schemes are based on the finite difference schemes of Lele (1992) and Pade scheme. The compact schemes by Lele require a tridiagonal matrix inversion for fourth and sixth order accurate schemes, while the eighth order scheme requires a pentadiagonal matrix inversion and it needs two boundary stencils due to its larger computational stencil. The schemes developed by Hixon, which are called compact MacCormack schemes, do not require a tridiagonal matrix inversion for fourth and sixth order schemes. The eighth order accurate

scheme developed by Hixon reduces the pentadiagonal system of the equivalent Lele scheme to tridiagonal system. These schemes are highly affected by the boundary stencil and a special treatment of the finite difference is needed at the boundaries.

2.2.2 Boundary Conditions for Computational Aeroacoustics

Several Boundary conditions are proposed for computational aeroacoustics. These boundary conditions may be classified into four categories:

2.2.2.1 Characteristic Boundary Conditions:

This method is based on the characteristic lines, i.e., on the analysis of the different waves crossing the boundary.

Engquist and Majda (1977) proposed well-posed mixed boundary value problem that lead to boundary conditions for the wave equation. This work is considered one of the early attempts to develop characteristic boundary conditions for linear time dependent hyperbolic system of equations.

Hedstrom (1979) introduced nonreflecting boundary conditions for nonlinear hyperbolic systems. His approach relies on the existence of Riemann invariants. Therefore, this method produces a reflection from outgoing strong shock waves. Based on the eigenvalues of the system, Hedstrom identified the incoming and outgoing characteristics. For simple outgoing waves, all the incoming characteristics are set equal to zero.

In order to reduce the wave reflection at the outflow boundary for Navier –Stokes calculations, Rudy and Strikwerda (1980) proposed boundary conditions based on the characteristics of the equations. The incoming characteristics are modified such that the pressure at the boundary will be kept close to the mean pressure. A term is added to the incoming characteristics and this term is proportional to the difference between the pressure at the outflow boundary and the steady state pressure.

Other characteristic boundary conditions are developed by Thompson (1987) and (1990) for time dependent hyperbolic systems and multidimensional problems. This work concentrates on specifying the characteristics of Navier-Stokes equations at the boundaries. All the incoming waves are set equal to zero while the outgoing waves are obtained from the computational domain. Thompson boundary conditions are proposed for nonrectangular as well as rectangular coordinate systems. The formulation is described for common problems in hydrodynamics, including solid wall and nonreflecting bound-aries. This type of boundary treatment is discussed in some detail through chapter 5.

Giles (1990) constructed steady and unsteady nonreflecting boundary conditions for Euler equations. This work has some success because it accounts for multidimensional effects while most of the characteristic-based methods are inherently one-dimensional and produce considerable error when oblique waves attempt to pass out of the domain. Giles boundary conditions work well at inflow as well as outflow boundaries. Only, the viscous effects are not considered in this boundary treatment.

A review of the characteristic boundary conditions is published by Poinsot and Lele (1992). Nonreflecting characteristic boundary conditions for subsonic and supersonic flows are derived. The analysis is applied for Navier-stokes and Euler equations. A subsonic inflow boundary is developed based on the characteristic of the equations where all the incoming waves are specified and the outgoing waves are computed from the interior points using the continuity equation in the characteristic form.

2.2.2.2 Radiation Boundary Conditions

Radiation boundary conditions are based on the asymptotic solution of the governing equations in the far field. One of the early attempts to develop radiation boundary conditions is done by Bayliss and Turkel (1980). They constructed boundary

conditions based on the asymptotic expansion of the solution valid for large distances. Their approach is valid only for linearized Euler equations and gives satisfactory results in the far field with hyperbolic linear equations. This boundary treatment is developed by matching the solution of the asymptotic expansion on the boundary to the solution exterior to the boundary. Another work for Bayliss and Turkel appeared in 1982. In this work, a radiation boundary condition is developed for the linearized wave equation with the existence of free stream velocity. A more general form of far field boundary conditions is derived.

Tam and Dong (1995) derived acoustic radiation boundary conditions for inflow boundaries. In addition, outflow boundary conditions are developed for Euler equations to allow the acoustic, vorticity and entropy disturbances to exit the computational domain without significant reflections. Their boundary conditions are derived for weakly non-homogenous mean flow with the assumption that the outgoing acoustic disturbances are propagating in the radial direction relative to the noise source. The position of the sound source is required for the computations of these boundary conditions.

2.2.2.3 Buffer Domain Boundary Conditions

Several buffer domain methods are proposed for the treatment of the outflow boundaries for computational aeroacoustics. One of these techniques is suggested by Street and Macaraeg (1989) for incompressible flow. The idea of these boundary conditions is based upon reducing the ellipticity of Navier-Stokes equations in a buffer region while solving the governing equations without modifications in the domain of interest. The ellipticity of Navier-Stokes equations exists due to two terms. One is due to the viscous terms and the other is due to the pressure field. Street and Macaraeg suggest that the streamwise viscous terms are smoothly reduced to zero via multiplying by an appropriate function in a buffer domain which is appended to the end of the computational domain of interest. Additionally, the convective velocity in the nonlinear advection terms is modified in the buffer domain to involve the mean flow velocity only at outflow. This is also done via a smooth coefficient function. In order to deal with the

pressure term at the boundary, the normal pressure derivative is attenuated to zero in the buffer domain. A buffer domain of the same length as the computational domain is suggested by Street and Macaraeg to study the stability of channel flow. Joslin et al (1992) used a buffer domain which is three times larger than the streamwise wave length in order to provide a smooth enough attenuation function and to avoid upstream influence. The buffer domain suggested by Joslin is employed for the direct numerical simulation of three dimensional incompressible Navier-Stokes equations.

Another attempt to apply the buffer domain technique for compressible Navier-Stokes equations is presented by Pruett and Chang (1993) to compute high speed boundary layer flows over an axisymmetric body. They suggested modifying only the streamwise viscous terms and the mean streamwise velocity profile in the buffer region. A buffer domain of length 1.8 wavelength is used in the simulation.

A different technique is used by Colonius, Lele and Moin (1997) to damp the disturbance in a sponge region. In this region, a combination of grid stretching in the streamwise direction and low-pass filtering (applied spatially) is used to effectively reduce the amplitudes of fluctuations before they interact with the downstream boundary, thus diminishing the reflections. Experiments with the sponge layer show that spurious reflections are reduced in amplitude by as many as three orders of magnitude over linearized boundary conditions alone. This method requires using very long sponge region compared with the computational domain of interest and hence more computational effort is needed.

2.2.2.4 Perfectly Matching Layer Technique

The idea of this method is to introduce a layer adjacent to the computational domain. In this layer, the outgoing waves are damped exponentially such that the amplitude of the disturbances is reduced to approximately zero at the outflow boundary.

The perfectly matching layer technique is first proposed by Berenger (1994) for the absorption of electromagnetic waves with no reflections.

Hu (1996) proposed a perfectly matching layer for absorbing outgoing waves of the linearized Euler equations for two-dimensional problems. It is proven by Hu that using the perfectly matching layer for both linear and nonlinear equations reduces to zero the reflections of incident linear waves at the interface between the interior domain and the matching layer, and the amplitude of the disturbances that enter the layer decreases exponentially. Moreover, the perfectly matching layer boundary conditions require adding very few number of points adjacent to the computational domain which makes it very efficient method relative to the buffer domain technique. In the current research, the perfectly matching layer technique is extended for the absorption of the acoustic waves of Navier-Stokes equations as explained in chapter 5.

2.2.3 Linear Stability and Large Eddy Simulation Studies

Linear stability analysis provides information about transition to turbulence in the linear region such as the most unstable frequency, growth rate at certain frequency, the amplitude of the disturbances and the distance required for the jet flow to become turbulent. In addition, the results from the linear stability analysis can be used to validate the direct numerical simulation results in the linear region.

Malik, Chuang and Hussaini (1982) and Malik (1990) studied the solution of compressible linear stability equations numerically. Second and fourth order finite difference methods as well as spectral collocation methods are used to solve the temporal and spatial stability of three dimensional compressible boundary layer flow on a swept wing. The discretized equations constitute an eigenvalue problem. Global and local methods are employed in this study to compute the eigenvalues of the discretized system. For the global method, a generalized eigenvalue problem is set up and the eigenvalues are obtained using standard algorithms, which yield all the eigenvalues of the discretized

system and a guess for the eigenvalues is not required to solve the temporal and spatial stability problem.

Khorammi (1991) studied the stability of a compressible swirling jet using the linearized Navier-Stokes equations in cylindrical coordinates. The global method is used to compute the eigenvalues of the discretized equations and Chebychev spectral collocation technique is utilized to discretize the governing equations. The effect of swirling, Mach number and Reynolds number on jet stability is discussed in this work. It is found that with addition of a modest amount of swirl, instability growth rates are substantially increasing. Additionally, rotating jets are found to be highly unstable for disturbances with high azimuthal wave numbers. Most importantly, it is found that the stabilizing influence of increasing Mach number diminished with the introduction of swirl to the jet flow.

Direct numerical simulation of jets cannot resolve all the scales of motion for high Reynolds numbers. Therefore, it is appropriate to perform a large eddy simulation to accurately predict the larger scales of motion while modeling the subgrid-scale turbulence. Mankbadi et al (1993) presented the large eddy simulation of supersonic jet with emphasis on capturing the unsteady features of the flow pertinent to sound emission. In this study, the filtered Navier-Stokes equations in polar coordinates are utilized to evaluate the near field source of axisymmetric jet. Two-four scheme by Gottlieb and Turkel is employed with characteristic boundary conditions. The results are described for high Reynolds number ($Re=1.27x10^6$) and Mach number equals 1.5. The sound radiated to the far field is computed using the acoustic analogy of Lighthill's theory.

2.2.4 Direct Numerical Simulation and Far Field Noise Computation Studies

Evaluating the sound source in the near field and computing the noise radiated from the shear layer are the main issues in the jet problem which have been studied

extensively. It is believed that direct numerical simulation is the tool which resolves all the turbulent scales by using the unsteady flow equations.

Lele (1989) studied the vortex roll up and pairing process of compressible free shear flows by using direct numerical simulation of the full unsteady equations. Compact finite difference scheme of sixth order accuracy and characteristic boundary conditions are utilized in this simulation. Both temporally and spatially growing mixing layers are treated. The compressibility effects on the spreading rate are parameterized in terms of a single Mach number, a convective Mach number, which is defined in a frame of reference moving with the dominant eddies of the flow. The spatially evolving simulations are forced at the inflow by adding inflow disturbance of the fundamental frequency and its subharmonics. The simulations are presented for Pr=0.75, Re=100-500 and for supersonic mixing layers with M_1=2.4 and M_2=1.2.

In 1990, Mankbadi examined the self-noise produced by instability waves in a round jet. Lighthill's theory is used to predict the far field sound radiated by the instability waves. The near field source is evaluated using linear instability theory. Mankbadi found that the self-noise intensity is proportional to the fourth order of the velocity amplitude saturation and the directivity becomes more pronounced and increases with increasing the jet velocity.

The unsteady behavior of the near field jet flow is investigated by Scott (1992). In this work, Scott studied the unsteady flow features of supersonic jets such as the production and interaction of the large scale vortex structures, and the presence of shock waves and their interaction with the shear layer as well as vortices. Numerical solutions of the time dependent, compressible Navier-Stokes equations are utilized and second order accurate MacCormack explicit finite difference scheme is employed for the solution of the governing equations. Time varying numerical data has been analyzed using experimental data. The results are in general agreement with experimental results.

Rai and Moin (1993) described a high order accurate finite difference approach for the direct numerical simulation of transition and turbulence in compressible boundary layers. The technique involves using a zonal grid system, upwind-biased differences for the convective terms, central differences for the viscous terms, and an iterative-implicit time integration scheme. The integration method is used to compute transition and turbulence on a flat plate. The main objective of this work is to determine the computability of such a flow with the available computer speeds and storage and to address some of the algorithmic issues such as accuracy, inlet and exit boundary conditions, and grid-point requirements. A new feature of the study is the presence of high levels of broadband free-stream fluctuations. The computational results indicate that the essential features of the transition process have been captured. In addition, the finite difference method presented can be used for complex geometry.

Using the two-four scheme developed by Gottlieb and Turkel, and outflow characteristic boundary conditions, Hayder et al (1993) presented a direct numerical simulation of high Mach number, plane and axisymmetric jets. The simulation is presented for two-dimensional disturbances with very high reynolds number ($Re=1.27x10^6$) and different grid sizes. The governing equations are the full unsteady Navier-stokes equations. Results are described for different Mach numbers and the data obtained are in good agreement with the linear stability theory.

An attempt to combine a wave solution method and unsteady flow computations to produce an integrated aeroacoustic code to predict the far field jet noise is presented by Soh (1994). An axisymmetric subsonic jet ($M_j=0.6$) is considered for this purpose. A fourth order accurate Pade compact scheme is used for the unsteady Navier-stokes solution. A kirchhoff surface integral is employed through the use of an imginary surface which is a circular cylinder enclosing the jet at a distance. Information such as pressure and its time and normal derivatives is provided on the surface. The sound prediction is performed side by side with the jet flow computation. Retarded time is also taken into consideration since the cylinder is not acoustically compact. The far field sound pressure

spectra and directivity show that low frequency peaks shift toward higher frequency region as the observation angle increases from the jet flow axis.

Viswanathan et al (1994) described a technique for the prediction of the noise characteristics of supersonic axisymmetric jets. In this approach, the jet mean flow is modeled through numerical solution of the three-dimensional compressible Navier-Stokes equations with an algebraic turbulence model. A second order MacCormack scheme with finite volume discretization is utilized for the solution of the governing equations. Inflow perturbations based on hydrodynamic stability theory are introduced at the nozzle lip. The far field sound propagation is obtained by solving the linearized Euler equations. Effects of jet temperature on the radiated sound are examined and qualitative comparisons with experiment are presented.

Mitchel, Lele and Moin (1995) computed the sound radiated by vortex pairing in the shear layer of cold subsonic and supersonic jets (M_j=0.4, 0.8 and 1.2) with low Reynolds number (Re=2500). The computational domain is extended to long distances in both axial and radial directions with grid clustering in the radial direction. The jet flow is forced at the fundamental frequency and its first two subharmonics. A compact finite difference scheme with sixth order accuracy is used with Giles inflow boundary conditions and sponge layer at the outflow boundaries. Results obtained from direct computations of Navier-Stokes equations are compared with Lighthill's acoustic analogy theory and Kirchhoff surface integral method. These predictions are in good agreement with the direct numerical simulation results. The study shows that, at low Mach number, the far field sound has distinct angles of extinction in the range of 60-70 degrees from the downstream jet axis, which can be understood with analogy to axisymmetric point quadropoles. As the Mach number is increased, the far field sound tends towards superdirectivity with the dominant sound directed at shallow angles to the downstream jet axis.

Linearized Euler equations are used by Shih and Mankbadi (1996) to simulate supersonic jet noise generation and propagation. The linearized Euler equations are

employed in this study to describe both near field where the sound is generated and the propagation of sound to the far field. The effects of a random frequency input disturbance are investigated. The radial profile of the input disturbance is a Guassian distribution centered in the shear layer. A qualitative agreement with experiment is presented in this work.

Ribner (1995) extended Lighthill's theory of jet noise to encompass refraction and shielding. The new formalism of jet noise prediction, that includes the refractive cone of silence and other effects, is derived. The key step to this form is deferral of the simplifying assumption of uniform density in the dominant source term. The main effect is to amend the Lighthill solution to allow for refraction by mean flow gradients, achieved via a frequency dependent directional factor. A general formula for power spectral density is developed as the Lighthill-based value multiplied by a squared, normalized Green's function. The normalized Green's function is near unity outside the cone of silence, which validates Lighthill's approach.

Viswanathan and Sankar (1995) predicted supersonic jet noise by using direct numerical simulation. In this approach, each flow parameter is decomposed into a time averaged mean and a time-dependent fluctuation part. The mean flow is established with the solution of the three-dimensional compressible Navier-Stokes equations in the first step. Inflow disturbance based on the solution of linearized Euler equations are introduced at the inflow boundary for the most unstable frequency and its subharmonics. Then, the wave propagation in the far field are studied through the solution of Euler equations. Some dynamic features of jet flow at high Mach number (M_j=2) are presented. Predictions of radiated noise for test cases and qualitative comparisons with experiments are made. Effects of jet temperature on the peak directivity of the radiated sound are examined.

A zonal approach for direct computation of sound generation and propagation from supersonic jet (M_j=2.1), Re=70000, is investigated by Shih, Hixon and Mankbadi (1995). In this work, the computational domain is split into a nonlinear, acoustic source

regime and a linear acoustic wave propagation regime. In the nonlinear regime, the unsteady flow is governed by the large-scale equations, which are the filtered compressible Navier-Stokes equations. Linearized Euler equations are used in the linear acoustic regime to describe the sound wave propagation. The computational results are presented and no spurious modes are generated in the matching region. Thus, the computational expense is reduced substantially as opposed to fully large-scale equations.

Shih, Hixon and Mankbadi (1995) also investigated the structure of a three-dimensional jet using the full unsteady Navier-Stokes equations in cylindrical coordinates. Numerical treatment of the singularities at the centerline is considered. Three different approaches for the centerline treatment are suggested. Some of these treatments result in the solution diverging as the amplitude of the disturbance becomes large at the centerline. Other approaches such as the asymptotic solution of the equations give satisfactory results with nonlinear development of the disturbance.

Colonius, Lele and Moin (1995) investigated the sound generated by vortex pairing in a two-dimensional compressible mixing layer. Direct numerical simulation of the Navier-Stokes equations is used to compute both the near field region and a portion of the acoustic field. The acoustic analogy due to Lilley (1974) is also solved with acoustic sources determined from the near field data of the direct numerical simulation. Additionally, the study shows that several common simplifications to the acoustic sources can lead to erroneous predictions for the acoustic field. Predictions based on the quadrupole form of source terms derived by Goldstein (1976, 1984) are in excellent agreement with the direct computations. However, despite the low Mach number of the flow, the acoustic far field generated by vortex pairings can not be described by considering compact quadrupole sources, and the acoustic far field is described by a superdirective model as discussed by Crighton and Huerre (1990). The presence of flow-acoustic interactions in the computed source terms causes the acoustic field predicted by the acoustic analogy theory to be very sensitive to small changes in the description of the source.

Direct numerical simulation of time evolving annular mixing layers, that corresponds to the early development of round jet, is used by Freund et al (1997) to study compressibility effects on turbulence dynamics and mixing in free shear flow. Nine cases are considered with convective mach numbers ranging from M_c=0.1 to 1.8 and turbulent Mach numbers reaching as high as 0.8. Sixth order compact finite difference scheme is used in this simulation and the derivatives in the azimuthal direction are calculated using Fourier Transform. The high frequency oscillations are attenuated in the azimuthal direction by eliminating these modes from the Fourier transform and severe limitations on the time step due to fine grid at the centerline is treated. Moreover, the singularities at the centerline are treated by using Cartesian-coordinates equations. Periodic boundary conditions are utilized in the axial and azimuthal directions and Giles boundary conditions are employed in the far field. The study shows that the growth rates of the simulated mixing layers are suppressed with increasing Mach number and Reynolds stresses are also suppressed. At low Mach numbers, the flow is dominated by large azimuthally correlated rollers, whereas at high Mach numbers the flow is dominated by small streamwise oriented structures. A change in turbulence structure by a breakdown across supersonically deforming eddies is found to be responsible for the suppression of pressure fluctuations.

Bayliss and Mastrello (1997) simulated the generation and propagation of sound in a high subsonic jet (M_j=0.9) that is excited by nonaxisymmetric disturbances. These disturbances are introduced by transient mass injection by a finite duration pulse via a modulated ring source. The simulation considers full nonlinear Euler equations and two-four scheme is used for the numerical solution of these equations. The study indicates that the jet is dominated by vorticity and pressure disturbances generated at the nozzle lip, which grow as they convect downstream in the jet. As a result of disturbance propagation, sound is generated. The primary effect of nonaxisymmetric disturbances is that of a flapping mode where regions of high and low pressure alternate on opposite sides of the jet. The predominant feature of this mode is the appearance of relatively large deviations of the pressure from the ambient pressure on opposite sides of the jet and the convection of these regions downstream.

Balakumar (1998) computed supersonic jet noise with M_j=2.1 by solving the wave equation analytically using the Fourier transform to avoid the numerical errors. The near field source is obtained using the parabolized stability equations and the near field data is submitted to the wave equation as Dirchliet boundary conditions. The results show good agreement with the experimental data.

Direct numerical simulation of a perfectly expanded supersonic turbulent jet (M_j=1.92) is investigated by Freund et al (1998). Solution of compressible Navier-Stokes equations in cylindrical coordinates and without modeling assumptions is considered in a computational domain that includes the near acoustic field. Low Reynolds number simulation is presented for cold jet with temperature ratio 1.12. Sixth order compact finite difference scheme is employed for the discretization in the radial and axial directions while Fourier transform is used to obtain the azimuthal derivatives and Runge-Kutta algorithm is utilized for the time advancements. Reynolds stresses, two-point correlations and turbulent energy spectra are computed and discussed. The sound field is found to be highly directional and dominant by Mach waves as observed experimentally. Analysis of the sound shows that nonlinear effects are significant away from the jet. Sound pressure levels are compared with experimental results and found to agree with jets at similar convective Mach numbers.

2.3 Experimental Work

Recently, many experimental studies have been carried out in order to measure the noise radiated from supersonic and subsonic jets. One of the early attempts to measure the sound emitted from the jet turbulence is conducted by Crow and Champagne (1971). Their experiments are undertaken on round jets with very small Mach numbers. A flow visualization technique is used to study the effect of varying Reynolds numbers on the orderly jet turbulence structure. They observed that as Reynolds number increases, jet instability evolves and the wavelength decreases. The effect of changing the amplitude

of the forcing function and the Strouhal number on the jet structure is investigated. As the amplitude of the forcing function increases, the axial velocity disturbance for the fundamental frequency and its subharmonics increases until it saturates. A maximum fluctuation amplitude is obtained at the fundamental frequency (st=0.3) while the amplitude decreases as the frequency gets away from the fundamental frequency. These results support the results presented in chapter 6 for subsonic jet.

In 1973, Massier et al conducted an experimental investigation to characterize the fluctuating density within a high temperature ($1100^{o}K$) subsonic jet and to characterize the noise radiated to the surroundings. The fluctuating components have been characterized by the use of cross-correlation that is obtained by introducing time delay to the signals detected from spatially separated crossed laser beams that are projected through the jet. The lasers are set up as a Schlieren system. The radiated noise is compared with the theory of Lighthill. In addition, the noise is characterized in terms of the noise cross-correlation coefficient and the autocorrelation function in the moving frame of reference of eddies. Correlation of the radiated noise is evaluated from the signals obtained with pairs of microphones. The jet flow is shock free and the Mach number at the nozzle exit is 0.5. Comparisons of the noise results with Lighthill's theory indicate good agreement at the lower frequencies, especially at the larger emission angles. At low angles and high frequencies, Lighthill's prediction is higher than the experimental results. Massier concludes that this difference results primarily from neglecting the effects of refraction and of limitations in the accountability of convection application in Lighthill's theory.

Another experiment has been conducted by Dankevala et al (1973) to measure the properties of density fluctuations in the turbulent regions for subsonic and supersonic jets at Mach numbers 0.7, 1.0 and 1.94. The local density correlation functions are used to predict the axial distribution of source strengths and the spectrum of noise due to a unit volume of turbulence.

Computation of the sound source for turbulent jets in the near field represents one of the big challenges in this field. An interesting method to predict the distribution of the sound source intensities by suitable acoustic measurements in the far field is developed by Grosche (1973). The sound waves emitted by a small volume of the jet are focused upon a microphone outside the flow by means of a large elliptical mirror. The distribution of the sound source intensities for subsonic and supersonic jets is investigated by moving the mirror-microphone assembly along and normal to the jet axis. The influence of the jet Mach number upon the sound source distribution is studied for subsonic jets. The sound source distributions are quite similar except for the absolute intensity and for a slight shift in the position of the maximum sound intensity. The supersonic fully expanded jet has a rather flat maximum at approximately x/d=14.

Meecham and Hurdle (1973) used the cross-correlation measurements to investigate noise-generating regions for the full-scale and model jets. The jet pressure fluctuations are measured with a microphone fitted with a nose cone. These measurements are made for various microphone positions at large number of far field positions and various angles. The measured values of the cross-correlation functions depend upon the angular position of the far field microphones, the jet exit Mach number and the position of the probe. The experiment is done for subsonic jets with Mach numbers 0.52, 0.62, 0.85 and 0.99 for the full-scale jet and Mach numbers 0.5 and 0.6 for the model jet. The results of the model jet experiment show that the turbulent volume is responsible for the major noise generating mechanisms of a free jet. This volume fluctuation is confined to a cylindrical volume centered about the jet axis and located in the general vicinity of the end of the potential core region. For high far field angles, the shear-mixing region becomes an additional, strong source region. When the jet velocity decreases, the source region shows a tendency to contract toward the jet nozzle with the shear-mixing region becoming more important for all far field angles.

Kibens (1980) has conducted an experiment to study the effect of using a symmetrical acoustic excitation chamber surrounding the nozzle on jet broadband noise. The jet Reynolds number is chosen to be 50000 for this experiment and the jet excited at

the most unstable frequency. As observed by Kibens, the phase coherent provided by the excitation signal enables the shear layer structure to develop into a sequence of periodic vortex pairing events at fixed positions in the shear layer. The resulting highly ordered vortex pairing cascades generate acoustic waves which propagate to the far field. The frequencies observed in the far field correspond exactly to the vortex formation frequencies in the flow field. This experiment shows that the broadband noise is reduced as a result of using the acoustic excitation chamber.

Another experimental investigation of the flow and acoustic properties of a moderate Reynolds number (Re=70000), Mach number (M_j=2.1), axisymmetric jet has been performed by Trout and McLaughlin (1981). The major results of the flow field measurements demonstrate that the jet shear layer is unstable over a broad frequency range. The initial growth rates and wavelengths of these instabilities as measured by a hot wire were found to be in reasonable agreement with linear stability theory predictions. Also, in agreement with subsonic jet results, the potential core of the jet was found to be most responsive to excitation at frequencies near a Strouhal number of St=0.3. The overall development of organized disturbances around St=0.2 seems to agree in general with calculations performed using the instability theory originally developed by Tam and Morris (1980). As discussed by Trout and McLaughlin, the acoustic near field is characterized in terms of sound-pressure level and directivity for both natural and excited (pure-tone) jets. In addition, the propagation direction and azimuthal character of dominant spectral components are also measured. It is determined that the large scale flow disturbances radiate noise in a directional pattern centered about 30° from the jet axis. The noise from these disturbances appears from simple ray tracing to be generated primarily near the region of the jet where the coherent fluctuations saturate in amplitude and begin to decay. It is also determined that the large-scale components of the near field sound are made up predominately of axisymmetric (n=0) and helical (n= $\pm$ 1) modes. The dominant noise generation mechanism appears to be a combination of Mach wave generation and a process associated with the saturation and disintegration of the large scale instability.

In 1982, Laufer and Yen conducted an experiment to investigate the relationship between the jet flow and its radiation field in the Mach number range $0.05 < M_j < 0.2$ and a Reynolds number range $6\times10^4 < Re < 2.3\times10^5$. The far field pressure is measured for various frequencies and Mach numbers. The nature of the source in the initial shear layer is characterized on the basis of these measurements. The principal result of this experiment is the acoustic sources are not convected but are located within a confined volume fixed with respect to the nozzle, even though they are being generated by moving disturbances in the jet. The acoustic sources are associated with the nonlinear saturation of the unstable wave amplitudes of the shear layer occurring at the vortex-pairing locations and the radiation intensity varies nonlinearly with the source strength and is highly directional in character.

Bridges and Hussain (1992) have provided a detailed evaluation of basic aeroacoustic theory applied to low Mach number (M_j =0.08) cold jets. This study compares theoretical predictions of jet noise with experimental results. A relatively complete knowledge of the flow field is used and vortex sound theory is employed for the comparison. The primary result is that the measured sound field directivity of vortex ring pairing in circular jet is very similar to that predicted by theory. The result also proves that pairing of axisymmetric coherent structures is not the dominant sound source in low Mach number jets and that vortex asymmetry must be an essential aspect of the vortex motions, which produce noise in such jets.

Noise radiated from under and over expanded jets and its suppression is investigated experimentally by Debiasi and Papamoschou (1999). The experiment has characterized the acoustics of axisymmetric high speed jets at pressure matched, over- and under-expanded conditions. The effect of an annular coflow on noise emission is also studied. The study demonstrates that addition of an annular coflow to a supersonic jet can reduce noise if the convective velocity of the jet eddies with respect to the coflow drops to subsonic values, ensuring that the coflow eddies are also subsonic with respect

to the ambient. The experiment has been conducted for supersonic jet with Mach numbers equal 1.5 and 1.75 and coflow subsonic jet with Mach numbers equal to 0.6 and 0.84. The coflow suppressed Mach wave emission from supersonic jet with the amount of 18 dB in the medium and high frequency spectral components of the far field.

2.4 Summary

To conclude the literature review, the numerical and experimental work on the jet problem are summarized as follows:

Numerical Schemes

Three different categories of numerical schemes for computational aeroacoustics are covered in this chapter. These categories include explicit MacCormack schemes with operator splitting developed by Hixon (1997), compact finite difference schemes proposed by Lele (1992) and dispersion relation-preserving scheme developed by Tam and Webb (1992). The dispersion error of MacCormack schemes are optimized and the accuracy of these schemes are increased up to sixth order. These schemes are dissipative and can solve flows with very high Reynolds number. The compact finite difference schemes show promise for resolving details of unsteady shear layers and sound generation, but is currently seem to be restricted to low Reynolds number flows. The dispersion relation-preserving scheme has the same dispersion properties as the original partial differential equations. This scheme is used to solve linear and nonlinear Euler equations. The current work focuses on using MacCormack schemes for computing the jet noise. A comparison between MacCormack schemes of different accuracy is discussed in chapter 6.

Boundary Conditions

Several boundary conditions are reviewed in this chapter including characteristic boundary conditions, radiation boundary conditions, buffer domain technique and

perfectly matching layer method. Several characteristic boundary conditions are proposed by Engquist and Majda (1977), Rudy and Strikwerda (1980), and Thompson (1987). The radiation boundary conditions are developed by matching the solution of the asymptotic expansion on the boundary to the solution exterior to the boundary. Bayliss and Turkel (1980) derived radiation boundary conditions which are valid for linearized Euler equations. Tam and Dong (1995) derived acoustic radiation boundary conditions for inflow and outflow boundaries. Their boundary conditions are used in chapter 8 to solve the linearized wave equation in the far field. In chapter 6, a comparison between the different outflow boundary conditions for Navier-Stokes computations is discussed.

Jet noise computations

The jet noise computations start with the work of Lighthill (1952) in which the jet noise is predicted using the acoustic analogy theory. During the past twenty years, there has been extensive work on supersonic and subsonic jet noise computations. Many studies are directed toward computing the sound generation in subsonic two-dimensional jets due to the vortex pairing process such as Soh (1994), Colonius et al (1995), and Mitchel et al (1995) and (1999). Compact finite difference schemes are used in these studies to compute both the near field and significant part of the acoustic field. In addition, the far field is computed using Lighthill's acoustic analogy theory and Kirchhoff's surface integral method. The results are compared with those obtained by Navier-Stokes equations. Other work is directed toward supersonic jet noise computations such as Scott (1992), Mankbadi (1994), Viswanthan et al (1994) and Shih et al (1996). Mankbadi (1994) uses the acoustic analogy to extend the solution to the far field while linearized Euler equations are used by Shih et al (1996) to simulate supersonic jet noise generation and propagation.

Chapter 3

Computations of Jet Mean Flow

Jet mean flow variables are required for the linear stability analysis and the direct numerical simulation of the noise radiated from the mixing layer. Evaluating the mean flow using the unsteady full Navier-Stokes equations needs a huge computational effort, while computing the mean flow is not the goal of the current research. Instead, the boundary-layer equations are employed to obtain an accurate and clean mean flow solution. Hence, a numerical method for solving the boundary-layer equations using two-point fourth order compact scheme is discussed in this chapter.

3.1 Governing Equations

The boundary-layer equations for axisymmetric jet, which is shown in Fig. (3.1), are used in the following form:

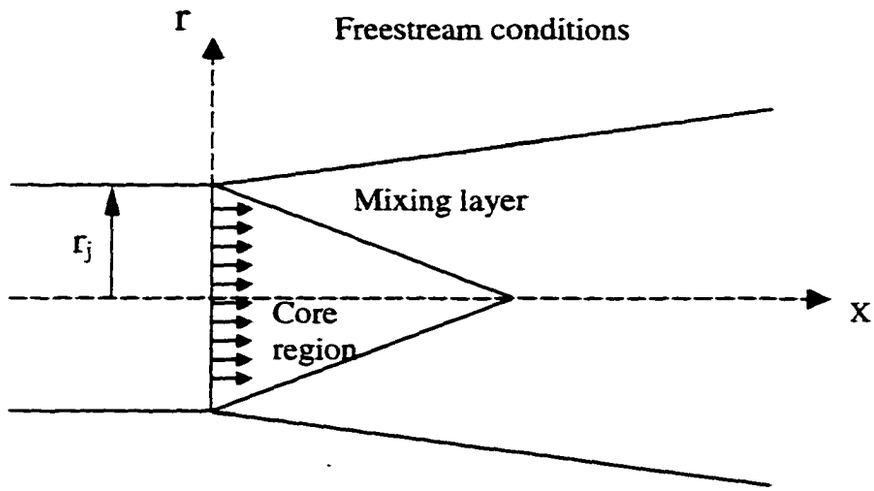

Figure (3.1) Schematic of two-dimensional axisymmetric jet

- Continuity equation

$$\frac{\partial(\rho U r)}{\partial x}+\frac{\partial(\rho V r)}{\partial r}=0 \tag{3.1}$$

- axial momentum equation

$$\rho U\frac{\partial U}{\partial x}+\rho V\frac{\partial U}{\partial r}=\frac{1}{r}\frac{\partial}{\partial r}(\mu r\frac{\partial U}{\partial r}) \tag{3.2}$$

- energy equation

$$\rho U C_p\frac{\partial T}{\partial x}+\rho V C_p\frac{\partial T}{\partial r}=\frac{1}{r}\frac{\partial}{\partial r}(k r\frac{\partial T}{\partial r})+\mu(\frac{\partial U}{\partial r})^2 \tag{3.3}$$

where ρ, U, V and T are density, axial velocity, radial velocity and temperature respectively.

The boundary-layer equations are used along with the equation of state to compute density, axial and radial velocities, and temperature. The mean pressure is assumed to be constant. The equation of state is used in this form:

$$P=\rho R T \tag{3.4}$$

The viscosity is calculated using Sutherland's law and the thermal conductivity is determined from the definition of Prandtl number.

$$\mu=1.458\times10^{-6}\frac{T^{3/2}}{T+110.4}\quad(\text{Newton.Sec/m}^2) \tag{3.5}$$

$$\text{Pr}=\frac{\mu Cp}{k} \tag{3.6}$$

Where μ is the viscosity, k the thermal conductivity and Cp the specific heat at constant pressure. Equations (3.1)-(3.5) are non-dimensionalized using the jet exit velocity (U_j^*), freestream temperature (T_∞^*) and freestream density (ρ_∞^*). The jet radius (r_j^*) is used to normalize the axial variables whereas the viscous length scale is used to normalize the variables in radial direction due to the different scales of jet problem in axial and radial directions. Thus, the following non-dimensional variables are used:

$$V=\frac{V^*\sqrt{\frac{r_j^*\,U_j^*}{v_\infty^*}}}{U_j^*},\qquad x=\frac{x^*}{r_j^*},\qquad r=\frac{r^*}{\sqrt{\frac{r_j^*\,v_\infty^*}{U_j^*}}},$$

$$U=\frac{U^*}{U_j^*},\qquad T=\frac{T^*}{T_\infty^*},\qquad p=\frac{p^*}{p_\infty^*},\qquad (3.7)$$

$$\rho=\frac{\rho^*}{\rho_\infty^*},\qquad M=\frac{U_j^*}{\sqrt{\gamma R T_\infty^*}},$$

where asterisks denote dimensional quantities, the subscript j defines the jet inlet conditions, ∞ denotes the freestream conditions and M is the jet Mach number. Using the above definitions of the non-dimensional quantities, Equations (3.1)-(3.5) are rewritten as:

$$\frac{\partial V}{\partial r}+\frac{V}{r}+\frac{\partial U}{\partial x}+\frac{U}{\rho}\frac{\partial \rho}{\partial x}+\frac{V}{\rho}\frac{\partial \rho}{\partial r}=0 \qquad (3.8)$$

$$\rho U\frac{\partial U}{\partial x}+\rho V\frac{\partial U}{\partial r}=\frac{1}{r}\frac{\partial}{\partial r}(\mu r\frac{\partial U}{\partial r}) \qquad (3.9)$$

$$\rho U\frac{\partial T}{\partial x}+\rho V\frac{\partial T}{\partial r}=\frac{\mu}{\mathrm{Pr}}\frac{\partial^2 T}{\partial r^2}+\frac{\mu}{\mathrm{Pr}}\frac{\partial T}{\partial r}\frac{1}{r}+\frac{1}{\mathrm{Pr}}(\frac{\partial T}{\partial r})^2\frac{d\mu}{dT}+\mu(\gamma-1)M^2(\frac{\partial U}{\partial r})^2 \qquad (3.10)$$

$$\rho\ T=1 \qquad (3.11)$$

$$\mu=T^{3/2}(\frac{1+110.4/T_o}{T+110.4/T_o}) \qquad (3.12)$$

$$\mu=\frac{k}{\mathrm{Pr}} \qquad (3.13)$$

3.2 Boundary Conditions

Since the boundary-layer equations are parabolic differential equations, no outflow boundary conditions are needed to compute the jet mean flow. Boundary

conditions at the inflow boundary and in the far field as well as symmetrical boundary conditions at the jet centerline are required for the solution of the jet boundary-layer equations.

At x=0, axial, radial velocity profiles are specified as a function of the radial distance:

$$U = f(r) \tag{3.14}$$

$$V = 0 \tag{3.15}$$

The temperature is calculated from Crocco's relation:

$$T = T_\infty + (T_j - T_\infty)\frac{(U - U_\infty)}{(U_j - U_\infty)} + 0.5\,T_j\,(\gamma\text{-}1)\,\mathrm{M}^2(U_j - U)\frac{(U - U_\infty)}{(U_j - U_\infty)^2} \tag{3.16}$$

The density is obtained from the equation of state, Eq. (3.11):

$$\rho = \frac{1}{T} \tag{3.17}$$

At $r=r_{max}$, temperature and axial velocity are specified as:

$$T = 1 \tag{3.18}$$

$$U = U_\infty \tag{3.19}$$

At the centerline, the following symmetric boundary conditions are used:

$$\frac{\partial U}{\partial r} = 0 \tag{3.20}$$

$$\frac{\partial T}{\partial r} = 0 \tag{3.21}$$

$$V = 0 \tag{3.22}$$

3.3 Solution Procedures

The boundary-layer equations, Eqs. (3.8)-(3.10), equation of state, Eq. (3.11) and the fluid flow transport equations, Eqs. (3.12)-(3.13), are solved numerically with the boundary conditions, Eqs. (3.14)-(3.22), to obtain laminar jet mean flow. Two-point fourth order accurate compact scheme, which is Euler-MacLaurin formula, is used in the radial direction and three-point backward difference formula is employed in the axial direction as presented in Fig. (3.2). This numerical discretization method is used by Spall and Malik (1989), and Malik (1990). The advantage of this scheme is that fourth order accuracy is achieved with two points. Thus, non-uniform grid can be utilized in the radial direction without the need to use Jacobian transformations.

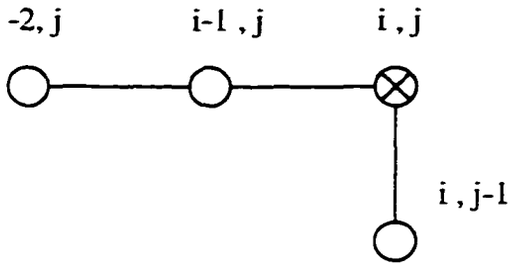

Figure (3.2) Computational stencil used for the solution of boundary-layer equations.

In order to apply this scheme, the equations should be written as a system of first order differential equations. Hence, the axial derivatives in the boundary-layer equations has to be treated first by using a second order accurate, three-point upwind finite difference scheme where the coefficients of discretization are written in terms of Lagrangian interpolation which allows utilizing non-uniform grid in the axial direction. In addition, the boundary-layer equations are linearized around the initial conditions in order to use Euler-McLaurin formula.

The continuity Equation, Eq. (3.8), is written in terms of the velocities and temperature as follows:

$$\frac{\partial V}{\partial r}+\frac{V}{r}+\frac{\partial U}{\partial x}-\frac{U}{T}\frac{\partial T}{\partial x}-\frac{V}{T}\frac{\partial T}{\partial r}=0 \qquad (3.23)$$

Discretizing the derivatives in x-direction yields this equation to the form:

$$\frac{\partial V}{\partial r}+\frac{V}{r}+(a_1 U_2+a_2 U_1+a_3 U)-\frac{U}{T}(a_1 T_2+a_2 T_1+a_3 T)-\frac{V}{T}\frac{\partial T}{\partial r}=0 \tag{3.24}$$

where a_1, a_2, a_3 are Lagrangian interpolation coefficients and U_1, U_2, U_3 are the axial velocity at mesh points i-2, i-1, i respectively. Similarly, the axial momentum and energy equations are rewritten as:

$$\frac{\partial^2 U}{\partial r^2}=-\frac{1}{r}\frac{\partial U}{\partial r}-\frac{1}{\mu}\frac{d\mu}{dT}\frac{dT}{dr}\frac{\partial U}{\partial r}+\frac{U}{\mu T}(a_1 U_2+a_2 U_1+a_3 U)+\frac{V}{\mu T}\frac{\partial U}{\partial r} \tag{3.25}$$

$$\begin{aligned}\frac{\partial^2 T}{\partial r^2}=&-\frac{1}{r}\frac{\partial T}{\partial r}+\frac{\mathrm{Pr}\,U}{\mu\ T}(a_1 T_2+a_2 T_1+a_3 T)\\&+\frac{\mathrm{Pr}\,V}{\mu\ \mathrm{T}}\frac{\partial T}{\partial r}-\frac{1}{\mu}\left(\frac{\partial T}{\partial r}\right)^2\frac{d\mu}{dT}-\mathrm{Pr}\,(\gamma-1)M^2\left(\frac{\partial U}{\partial r}\right)^2\end{aligned} \tag{3.26}$$

Equations (3.24)-(3.26) are expressed in the following first-order system of differential equations:

$$\frac{d\psi}{dr}=f(\psi,r) \tag{3.27}$$

$$\text{Where, } \psi=\begin{bmatrix} U \\ \frac{\partial U}{\partial r} \\ V \\ T \\ \frac{\partial T}{\partial r} \end{bmatrix} \tag{3.28}$$

The nonlinear system of ordinary differential Equations, Eq. (3.27), is linearized around an initial guess (ψ_i) and the variables are written in terms of the incremental values $\Delta\psi$:

$$\overset{\circ}{\Delta\psi} = [f(\psi) - \overset{\circ}{\psi}]_i + [\frac{df}{d\psi}]_i \Delta\psi \tag{3.29}$$

Rewriting Eq. (3.29) in matrix form yields:

$$\overset{\circ}{\Delta\psi} = D\,\Delta\psi + F \tag{3.30}$$

Where, $D = [\frac{df}{d\psi}]_i$ (3.31)

$$F = [f(\psi) - \overset{\circ}{\psi}]_i \tag{3.32}$$

The coefficients of the matrices D and F are presented in appendix A. Similarly, the second derivative of $\Delta\psi$ is obtained from Eq. (3.27) as follows:

$$\overset{\circ\circ}{\psi} = f\frac{df}{d\psi} + \frac{df}{dr} \tag{3.33}$$

Linearizing Eq. (3.33) around an initial guess yields the following equation

$$\overset{\circ\circ}{\Delta\psi} = [f\frac{df}{d\psi} + \frac{df}{dr} - \overset{\circ\circ}{\psi}]_i + \frac{d}{d\psi}[f\frac{df}{d\psi} + \frac{df}{dr}]\Delta\psi \tag{3.34}$$

Hence, the linearized Eq. (3.34) for $\overset{\circ\circ}{\Delta\psi}$ is expressed as:

$$\overset{\circ\circ}{\Delta\psi} = G\,\Delta\psi + H \tag{3.35}$$

$$G = \frac{df}{d\psi}\frac{df}{d\psi} + f\frac{d^2 f}{d\psi^2} \tag{3.36}$$

$$H = [f\frac{df}{d\psi} + \frac{df}{dr} - \overset{\circ\circ}{\psi}]_i \tag{3.37}$$

The boundary-layer equations are singular at the centerline. Hence, a new set of equations is derived using L'Hospital rule and the same procedures are followed to get the matrices D, F, G and H.

Using Euler-McLaurin formula, the governing equations are discretized in the radial direction to obtain the incremental values $\Delta\psi$. The discretized equations are written as:

$$\Delta\psi_j - \Delta\psi_{j-1} = \frac{h_j}{2}(\Delta\overset{\circ}{\psi}_j + \Delta\overset{\circ}{\psi}_{j-1}) - \frac{h_j^2}{2}(\Delta\overset{\circ\circ}{\psi}_j - \Delta\overset{\circ\circ}{\psi}_{j-1}) \tag{3.38}$$

Substituting from Eqs. (3.30) and (3.37) into Eq. (3.38) yields:

$$A_{j-1}\Delta\psi_{j-1} + B_j\Delta\psi_j = S_j \tag{3.39}$$

where, $A_{j-1} = -I - \frac{h_j}{2}D_{j-1} - \frac{h_j^2}{12}G_{j-1}$ (3.40)

$$B_j = I - \frac{h_j}{2}D_j + \frac{h_j^2}{12}G_j \tag{3.41}$$

$$S_j = \frac{h_j}{2}(F_j + F_{j-1}) - \frac{h_j^2}{12}(H_j - H_{j-1}) \tag{3.42}$$

$$h_j = r_j - r_{j-1}, \quad j = 2,3,\ldots\ldots, N \tag{3.43}$$

, and I is the identity matrix.

At a station (i) in the axial direction and for N points in the radial direction, Eq. (3.39) constitutes a system of (5N-5) equations in 5N unknowns. Hence, five more equations are needed in order to complete the system. These equations are obtained from the boundary conditions at the centerline and at the far field, Eqs. (3.18)-(3.22), and may be expressed in the following matrix form.

For the boundary conditions at the centerline:

$$E_1\,\Delta\psi_1 = 0 \tag{3.44}$$

$$\text{where, } E_1 = \begin{bmatrix} 0 & 0 & 0 & 0 & 0 \\ 0 & 0 & 0 & 0 & 0 \\ 0 & 1 & 0 & 0 & 0 \\ 0 & 0 & 1 & 0 & 0 \\ 0 & 0 & 0 & 0 & 1 \end{bmatrix}$$

In the far field,

$$E_N \, \Delta\psi_N = Q_N \tag{3.45}$$

$$\text{where, } E_N = \begin{bmatrix} 1 & 0 & 0 & 0 & 0 \\ 0 & 0 & 0 & 1 & 0 \\ 0 & 0 & 0 & 0 & 0 \\ 0 & 0 & 0 & 0 & 0 \\ 0 & 0 & 0 & 0 & 0 \end{bmatrix}, \; Q_N = \begin{bmatrix} U_\infty \\ 1 \\ 0 \\ 0 \\ 0 \end{bmatrix}$$

A block tridiagonal system is constructed using Eqs. (3.39), (3.44) and (3.45) as explained by Malik, Chuang and Hussaini (1982). Then the block tridiagonal system is solved to obtain $\Delta\psi$ and new values for ψ are calculated. The solution is repeated iteratively until $\Delta\psi$ reaches certain prescribed accuracy.

Chapter 4

Linear Stability Analysis

In this chapter, the transition region of the jet-mixing layer is studied by using locally parallel linear stability theory. The linear stability analysis provides information about the disturbance growth or decay in the mixing layer. In order to investigate the linear region of the transition, linearized Navier-Stokes equations are utilized to compute temporal and spatial stability of jet flows. Different numerical techniques such as global and local methods are presented and the solution of the eigenvalue problem is explained. Some parameters such as the most unstable frequency of the jet flow, the eigenfunctions associated with the most unstable frequency and its subharmonics, and the N-factor are computed using the linear stability theory. Moreover, these results are introduced to the direct numerical simulation code as an inflow disturbance.

4.1 Mathematical Formulation of the stability problem

The stability problem is formulated using Navier-Stokes equations in cylindrical coordinates $(r,6,x)$. The linearized stability equations are then derived using Fourier decomposition of the flow variables. Each flow variable is assumed to consist of a mean flow component and a small perturbation component as presented in eq. (4.1). Second order perturbation terms are neglected in order to linearize the equations and the flow variables are written as:

$$\begin{bmatrix} u_r \\ u_\theta \\ u_x \\ \tilde{P} \\ \tilde{T} \\ \tilde{\rho} \end{bmatrix} = \begin{bmatrix} U(r) \\ V(r) \\ W(r) \\ \pi(r) \\ \eta(r) \\ \rho(r) \end{bmatrix} + \begin{bmatrix} F(r) \\ G(r) \\ H(r) \\ P(r) \\ T(r) \\ \delta(r) \end{bmatrix} e^{i(\alpha x + n\theta - \omega t)} \tag{4.1}$$

where α and n are the axial and azimuthal wavenumbers respectively and ω is the angular frequency. The mean flow variables are U,V,W,π,η and ρ and the corresponding disturbances are F,G,H,P,T and δ.

Substituting from Eq. (4.1) into Navier-Stokes equations results in the linearized equations in terms of perturbation eigenfunctions. In addition, the equation of state is employed to eliminate density perturbation from the linearized equations. Perturbations in the flow properties such as viscosity μ and thermal conductivity k are related to temperature disturbance via Sutherland's law and Prandtl number. The linearized Navier-Stokes equations are given in appendix B and the equations are normalized with respect to jet centerline mean flow variables and jet radius. Hence, flow parameters such as Reynolds number, Prandtl number and Mach number are defined as:

$$\mathrm{Re} = \frac{W_j \rho_j r_j}{\mu_j} \tag{4.2}$$

$$M_j = \frac{W_j}{\sqrt{\gamma R T_j}} \tag{4.3}$$

$$Pr = \frac{\mu C_p}{k} \tag{4.4}$$

where the subscript j denotes the jet centerline conditions.

4.1.1 Boundary Conditions

For a well-posed problem, a set of boundary conditions at the jet centerline and at the far field boundary are needed to close the system. The boundary conditions at the centerline are obtained from the linearized equations such that the singularities are removed from the equations and the solution is single valued, while the disturbances are forced to approach zero in the far field. The conditions at the centerline depend on the azimuthal wavenumber (n) as follows:

$$
\begin{aligned}
&\text{if } n = 0 \\
&F(0) = G(0) = 0 \\
&\frac{dH(0)}{dr} = \frac{dT(0)}{dr} = 0 \\
&\text{if } n = \pm 1 \\
&F(0) \pm iG(0) = 0 \\
&\frac{dF(0)}{dr} = 0 \\
&H(0) = T(0) = 0 \\
&\text{if } |n| > 1 \\
&F(0) = G(0) = 0 \\
&H(0) = T(0) = 0
\end{aligned}
\tag{4.5}
$$

In the far field:

$$F(rmax) = G(rmax) = H(rmax) = T(rmax) = 0 \tag{4.6}$$

4.2 Solution procedures

There are two classes of numerical methods that can be used for solving the linear stability problem. One of these techniques is the global method where a generalized eigenvalue problem is constructed and the eigenvalues are obtained by using standard algorithms. These algorithms yield all the eigenvalues of the discretized system and an initial guess for the eigenvalues is not required. The second technique is the local method, which requires an initial guess for the eigenvalue. Only the eigenvalue, which happens to lie in the neighborhood of the guessed value, is computed using iterative techniques such as Newton's method. Two different numerical schemes are employed for discretizing the global and local stability problems.

The global stability method is computationally much more expensive than the local method since all the eigenvalues of the discretized system are computed using this method. Thus, the only rationale for using the global method is if no guess for the eigenvalue is available or if the whole spectrum of eigenvalues is desired.

4.2.1 Global Method

The global method is limited to the temporal stability problem since the spatial eigenvalue (α) appears nonlinearly in the stability equations and the equations are not directly amenable to global analysis using the generalized eigenvalue approach. One of the alternatives, that is discussed by Khorami, Malik and Ash (1989), is to consider a transformation for the variables such that the nonlinear terms are treated for the stability problem. This technique will increase the order of the matrices and hence the computational effort is certainly very high compared with the temporal solution.

In order to construct the eigenvalue problem for temporal stability, the linearized Navier-Stokes equations are written in the following form:

$$A_1 \frac{d^2\phi}{dr^2} + B_1 \frac{d\phi}{dr} + C_1 \phi = \omega C_2 \phi \tag{4.7}$$

$$\text{where, } \phi = \begin{bmatrix} F \\ G \\ H \\ P \\ T \end{bmatrix} \tag{4.8}$$

The matrices A_1, B_1, C_1 and C_2 are (5x5) matrices and their coefficients are obtained from the linearized Navier-Stokes equations. In addition, Eq. (4.7) is transformed to new coordinates ξ to allow for grid clustering at the critical layer. Hence, Eq. (4.7) becomes:

$$\overline{A} \frac{d^2\phi}{d\xi^2} + \overline{B} \frac{d\phi}{d\xi} + C_1 \phi = \omega C_2 \phi \tag{4.9}$$

$$\text{where, } \overline{A} = A_1 \left(\frac{d\xi}{dr}\right)^2 \tag{4.10}$$

$$\overline{B} = A_1 \frac{d^2\xi}{dr^2} + B_1 \frac{d\xi}{dr} \tag{4.11}$$

Equation (4.9) is discretized using fourth-order central finite difference. One-sided difference is used at the boundaries and at points near the boundaries. Hence, the discretized equations are expressed in the following form:

$$\overline{\overline{E}}_j \phi_{j+2} + \overline{\overline{D}}_j \phi_{j+1} + \overline{\overline{C}}_j \phi_j + \overline{\overline{B}}_j \phi_{j-1} + \overline{\overline{A}}_j \phi_{j-2} = C_{2,j}\, \omega \phi_j \quad , j=2,3,\ldots\ldots, N-1 \tag{4.12}$$

For N points, Eq. (4.12) constitutes a system of (5N-10) equations in (5N) unknowns. Hence, 10 more equations are needed to complete the system. The boundary conditions at the centerline and in the far field, Eqs. (4.5) and (4.6), constitute 8 equations and another two boundary conditions for the pressure are added.

In the far field,

$$P=0 \tag{4.13}$$

At the centerline,

$$\text{For } n=0, \quad \frac{dP}{dr} = 0 \tag{4.14}$$

For $|n|>0$, $P = 0$

A pentadiagonal system for the generalized eigenvalue problem is constructed using Eq. (4.12) and the discretized boundary conditions, and may be expressed as:

$$A_o\, \Phi = \omega\, B_o\, \Phi \tag{4.15}$$

where A_o and B_o are the global matrices of the problem and their dimensions are (5Nx5N).

4.2.2 Local Stability Method

Both spatial and temporal stability problems are solved using the local method where an eigenvalue problem is constructed and solved iteratively using Newton's method. The solution is started from an initial guess, which is obtained from the global method.

The two-point fourth order compact finite difference scheme, which is derived by means of the Euler-Maclaurin formula, is utilized to solve the eigenvalue problem. This scheme requires representing the stability equations as a system of first-order ordinary differential equations as described in chapter 3. In order to write the linearized Navier-Stokes equations as a system of eight first-order equations, the second-order normal momentum equation is reduced to first-order by using the continuity equation. The continuity equation is differentiated with respect to (r) and the resulting equation is used to replace the second derivative of the normal velocity disturbance in the normal momentum equation. Thus, the continuity equation, the first order normal momentum equation, the second order axial and azimuthal momentum equations and the energy equation constitute eight first-order ordinary differential equations. This first-order system is expressed in this form

$$\frac{d\psi}{dr} = A\psi \tag{4.16}$$

$$\text{where } \psi = \left[H \quad \frac{dH}{dr} \quad F \quad P \quad T \quad \frac{dT}{dr} \quad G \quad \frac{dG}{dr} \right]^t \tag{4.17}$$

The matrix A is 8x8 matrix and its coefficients depend on mean flow variables, frequency, azimuthal and axial wavenumbers. Discretizing Eq. (4.16) using Euler-Maclaurin formula results in

$$\psi_j - \psi_{j-1} = \frac{h_j}{2}\{(\frac{d\psi}{dr})_j + (\frac{d\psi}{dr})_{j-1}\} - \frac{h_j^2}{2}\{(\frac{d^2\psi}{dr^2})_j - (\frac{d^2\psi}{dr^2})_{j-1}\} \tag{4.18}$$

where $h_j = r_j - r_{j-1}$

The second derivative of ψ is obtained by differentiating Eq. (4.16). Substituting into Eq. (4.18) yields this two-point equation for the discretized system.

$$D_{j-1}\,\psi_{j-1} + G_j\,\psi_j = 0 \tag{4.19}$$

Where, $D_{j-1} = -I - \frac{h_j}{2}A_{j-1} - \frac{h_j^2}{12}\{(\frac{dA}{dr})_{j-1} + A_{j-1}^2\}$ (4.20)

$$G_j = I - \frac{h_j}{2}A_j + \frac{h_j^2}{12}\{(\frac{dA}{dr})_j + A_j^2\} \tag{4.21}$$

At the jet centerline, the matrix A and its derivative matrix are singular. Hence, a new set of equations is derived at the centerline using L'Hospital rule. In addition, the finite difference is reduced to second-order accurate by dropping the fourth-order term $(d^2\psi/dr^2)$ from the numerical discretization in order to simplify the equations at the centerline. Hence, Eq. (4.19) is expressed in this form at j=2

$$\psi_2 - \psi_1 = \frac{h_2}{2}(A_2\,\psi_2 + A_1\,\psi_1) \tag{4.22}$$

The equations derived at the centerline have another singularities at certain azimuthal wavenumbers. The axial momentum and energy equations are singular for $|n| = 2$. Hence, these equations are replaced by Eqs. (4.23) and (4.24).

$$(\frac{dH}{dr})_{j=1} = 0 \tag{4.23}$$

$$(\frac{dT}{dr})_{j=1} = 0 \tag{4.24}$$

For $|n| = 1$ or $|n| = 3$, the azimuthal momentum is singular and it is replaced by this condition

$$(\frac{dG}{dr})_{j=1} = 0 \tag{4.25}$$

Thus, the matrix A_1 in Eq. (4.22) is modified at the centerline using Eqs. (4.23)-(4.25). Moreover, the boundary conditions at the centerline and in the far field are used to complete the system. Hence, a block tridiagonal system is constructed using Eq. (4.19) and the boundary conditions as explained in section 3.2.1. This method is discussed in some details by Malik et al (1982) and the block tridiagonal system can be rewritten as

$$\overline{A}_j \psi_{j-1} + \overline{B}_j \psi_j + \overline{C}_j \psi_{j+1} = \overline{H}_j \tag{4.26}$$

where $\overline{A}_j, \overline{B}_j, \overline{C}_j$ are 8×8 matrices and $\overline{H}$ is an 8×1 null matrix.

Equation (4.26) is homogenous and it yields the trivial solution. In order to avoid the trivial solution, non homogenous boundary conditions are imposed at jet centerline. By examining the boundary conditions at the centerline, it is appropriate to replace one of the boundary conditions by P(0)=1. This is equivalent to normalizing the eigenfunctions by the pressure at the centerline. The pressure perturbation at the centerline does not vanish for azimuthal wavenumbers equal zero and one. Hence, it is appropriate to use the normalizing condition P(0)=1 for these azimuthal wave number. Since all the perturbations at the centerline vanish for absolute values of azimuthal wavenumbers greater than one, the normalizing condition is not suitable. Instead, one of the discretized equations at a point in the middle is replaced by the unity condition. In the current research, the continuity equation at N/2 is replaced by the pressure condition. Thus, Eq. (4.26) becomes nonhomogenous and a nontrivial solution may be obtained for the guessed eigenvalue $\alpha = \alpha_0$. Newton's method is then used to iterate on α such that the missing equation is satisfied. The iteration process is illustrated as follows:

1. Starting from an initial guess α_0, the missing boundary condition η is calculated,

at n=0, $\eta = F(0)$ (4.27)

at $|n| > 1$, $\eta = f(N/2)$ (4.28)

where *f(N/2)* denotes the value of the continuity equation at node (*N/2*).

2. Step 1 is repeated with increasing α_0 by a small amount to α_1, and η_1 is calculated

3. The correction of $\Delta\alpha$ is calculated from Eq. (4.27)

$$\Delta\alpha = \frac{-\eta_0}{(\frac{\partial\eta}{\partial\alpha})} \tag{4.29}$$

$$\text{where, } \frac{\partial\eta}{\partial\alpha} = \frac{\eta_0 - \eta_1}{\alpha_0 - \alpha_1} \tag{4.30}$$

4. New value of α is calculated by

$$\alpha = \alpha_1 + \Delta\alpha \tag{4.31}$$

5. Steps 2 to 4 is repeated until η vanishes within preassigned tolerance.

4.3 Validation of the Global Method

In this section, the results obtained using the global method for temporal stability problem are compared with those computed by Khorrami (1991) for the stability of a compressible swirling jet. The same mean flow field employed by Khorrami is used to obtain these results. The following axial and azimuthal velocity profiles are assumed in order to study the stability of swirling jet

$$W = \frac{1}{(1+r^2)^2} \tag{4.32}$$

$$V = \sigma\frac{r}{(1+r^2)^2} \tag{4.33}$$

where the parameter σ is related to the swirl ratio q via

$$q=0.32475\ \sigma \tag{4.34}$$

The normal velocity component U is assumed to be zero for very high Reynolds number jet and the mean pressure is considered to be constant. The temperature is obtained from Crocco's relation for Pr=1

$$\eta(r) = \beta + (1-\beta)W + (\gamma-1)M^2 W(1-W) \tag{4.35}$$

where $\beta = \dfrac{\eta_\infty}{\eta_j}$ (4.36)

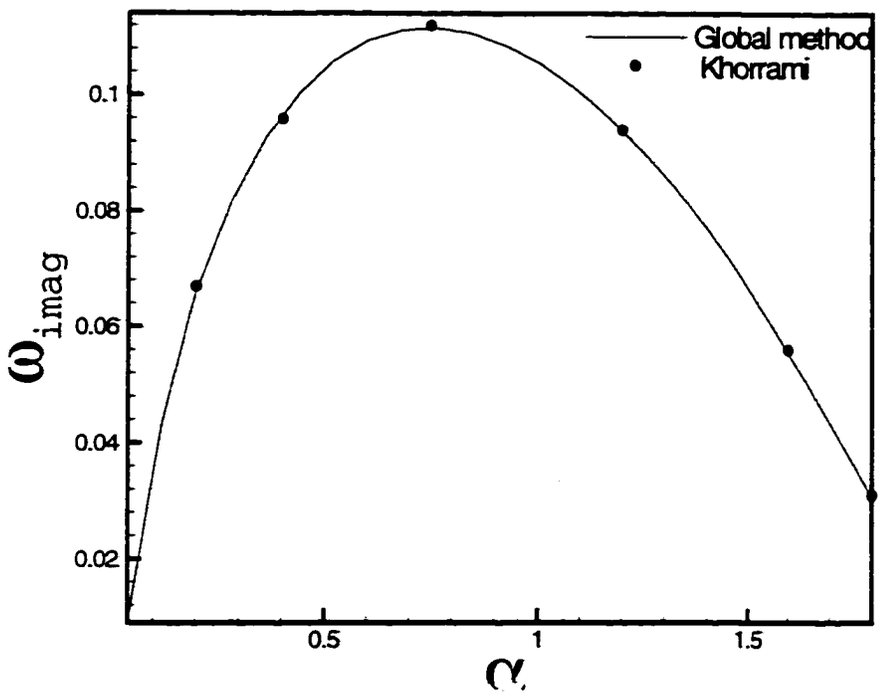

Figure (4.1) Variation of temporal growth rate with spatial wavenumber for swirling jet with M=0.8, Re=1000 and n=-1.

The results are calculated for a swirling jet (q=0.04) with M=0.8, Re=1000 and azimuthal wavenumber (n=-1). The variation of the growth rate ω_i and the frequency ω_r with the axial wavenumber α are presented in Figs. (4.1) and (4.2). The results indicate good agreement with Khorrami's results.

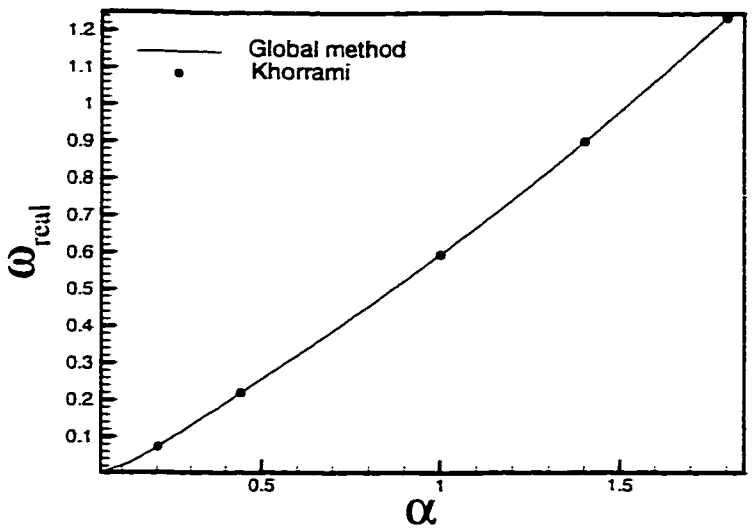

Figure (4.2) Variation of real part of the frequency with the spatial wavenumber for swirling jet with M=0.8, Re=1000 and n=-1.

4.4 Local Stability Results

In order to compute the jet stability using the linear theory, the mean flow is obtained first using the solution of the boundary layer equations as presented in chapter 3. Spatial stability is used to determine the spatial growth rate variation with the frequency and hence the most unstable frequency is estimated. The results are obtained for subsonic and supersonic jets with low and high Reynolds numbers. Moreover, the N-factor, which gives an indication about the length of the transition region, is computed at different frequencies. The N-factor is defined as

$$\text{N-Factor} = \int_{x_n}^{x} -\alpha_i \, dx_i \tag{4.37}$$

4.4.1 Subsonic Jets

The spatial stability for low subsonic jet ($M_j = 0.6$) and low Reynolds number (Re=2500) is studied using the local stability method. The mean flow is obtained first by specifying the axial velocity at the inlet station in the boundary-layer code with the following hyperbolic profile

$$U = 0.5[(1+U_\infty)-(1-U_\infty)\tanh\{\beta(r-1)\}] \tag{4.38}$$

The parameter β, which expresses the momentum thickness of the jet shear layer, is assumed to be 6 and Prandtl number is taken to be 1. The temperature is considered to be nearly constant in the shear layer. The mean flow parameters are presented in table (4.1).

Table (4.1) Jet mean flow parameters

$M_j = \frac{U_j}{\sqrt{\gamma R T_j}}$	$\mathrm{Re} = \frac{U_j \rho_j r_j}{\mu_j}$	$\frac{U_\infty}{U_j}$	$\frac{T_\infty}{T_j}$	Pr	β
0.6	2500	0	1	1	6

The computational domain is extended to 55 jet radius in the axial direction and 25 radius in the radial direction with uniform grid in the axial direction and the grid is clustered at the critical layer. The variation of axial velocity, radial velocity and jet temperature with downstream position are shown in Fig. (4.3). The jet is spreading strongly with the downstream axis because Reynolds number is very low. The temperature variation in the shear layer is small and higher radial velocity is obtained due to low Reynolds number.

The variation of spatial growth rate with the frequency is calculated at different downstream locations as shown in Fig. (4.4). As a result of mean flow variations with axial position, the growth rate for high frequencies decreases significantly as the jet develops downstream. However, the growth rate changes slightly at different axial locations for low frequencies. In addition, the growth rate varies with the frequency and it peaks at certain frequency. The frequency, which generates maximum growth rates decreases as the jet mean flow develops downstream. Hence, calculation of N-Factor is needed in order to determine the most-unstable frequency.

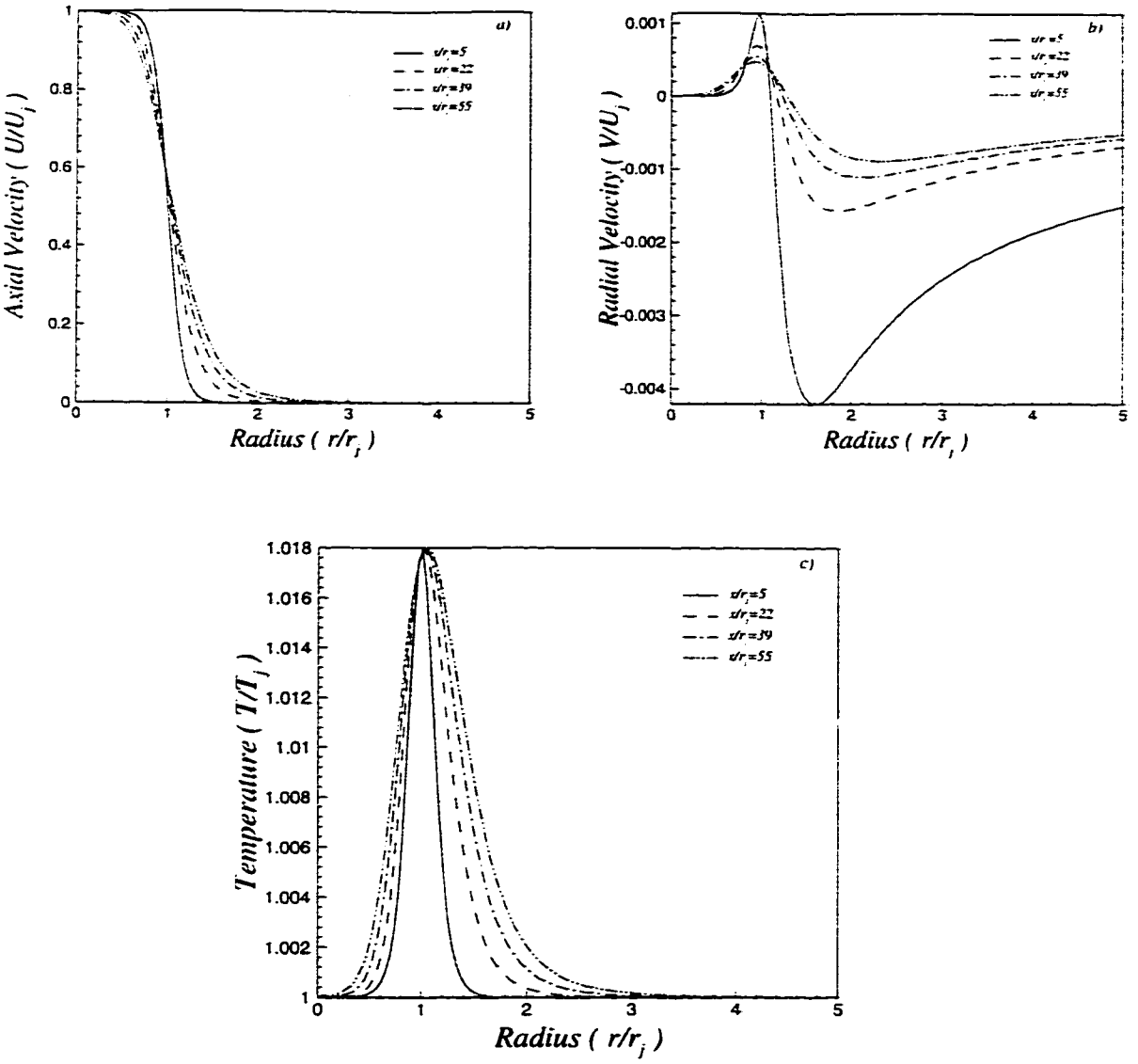

Figure (4.3) Mean flow for subsonic jet (M_j=0.6) and Re=2500
a) axial velocity b) radial velocity c) temperature

The real part of the spatial wavenumber, which expresses the spatial wave length, is plotted in Fig. (4.5). The graph indicates that the spatial wave length decreases with the increasing frequency of the disturbance and the wave length changes slightly as the jet evolves downstream for disturbances of low frequencies while the change in the wave length is clear for higher frequencies.

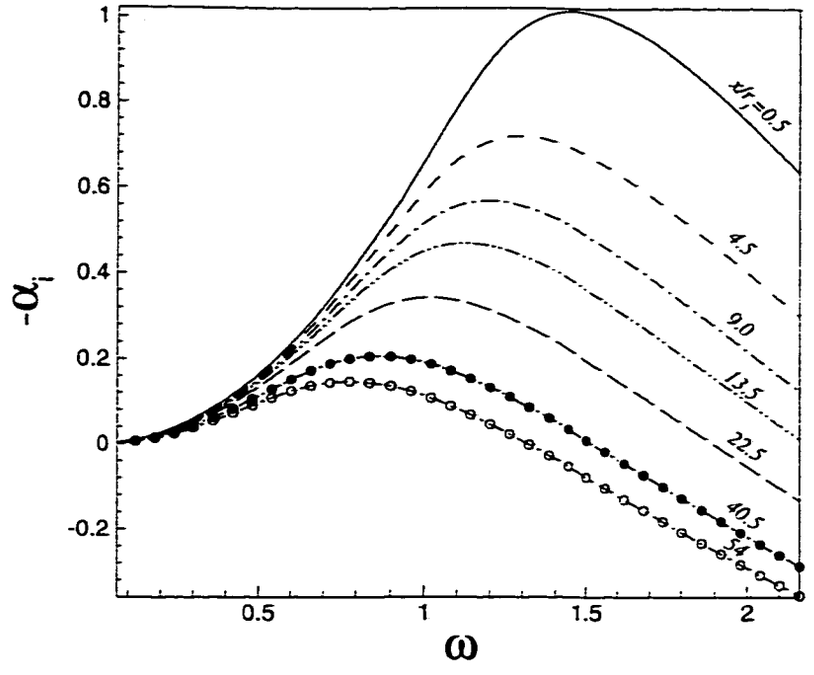

Figure (4.4) Disturbance growth rate versus frequency at different axial locations

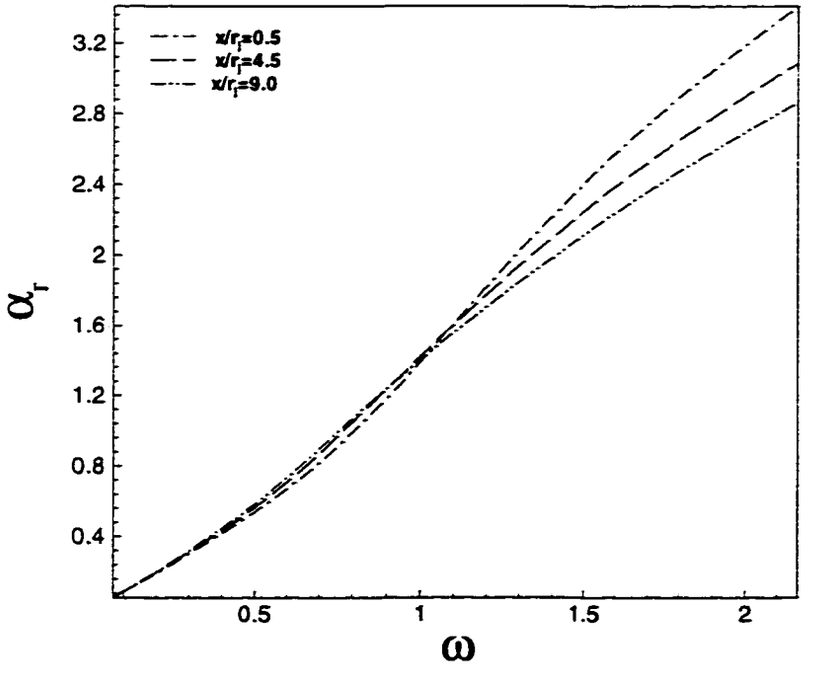

Figure (4.5) Wave number versus frequency at different axial locations for subsonic jet (M_j=0.6) and Re=2500

The N-Factor is calculated using Eq. (4.37) at different frequencies in order to estimate the fundamental frequency and the axial distance required for the disturbance to reach certain amplitude. The length of the transition region can be determined from the N-Factor. This information determines the length of the computational domain in the axial direction for Navier-Stokes computations. In addition, the fundamental frequency is used as the forcing function at the inflow boundary as discussed in chapter 5. The results for a subsonic jet with M_j=0.6 is introduced in Fig. (4.6). The N-Factor increases with the axial distance, which means that the amplitude of the disturbance is still increasing as a result of jet flow instabilities. After certain distance, the N-Factor decreases due to jet flow development. N-Factor is dependent upon the frequency and the axial position. In order to obtain N-Factor of 9, an axial distance of 14 radius is required for the disturbance at a frequency of 1.25 which means Strouhal number 0.398. Hence, the fundamental frequency for this jet is 1.25 and the transition occurs at x/r_j=14.

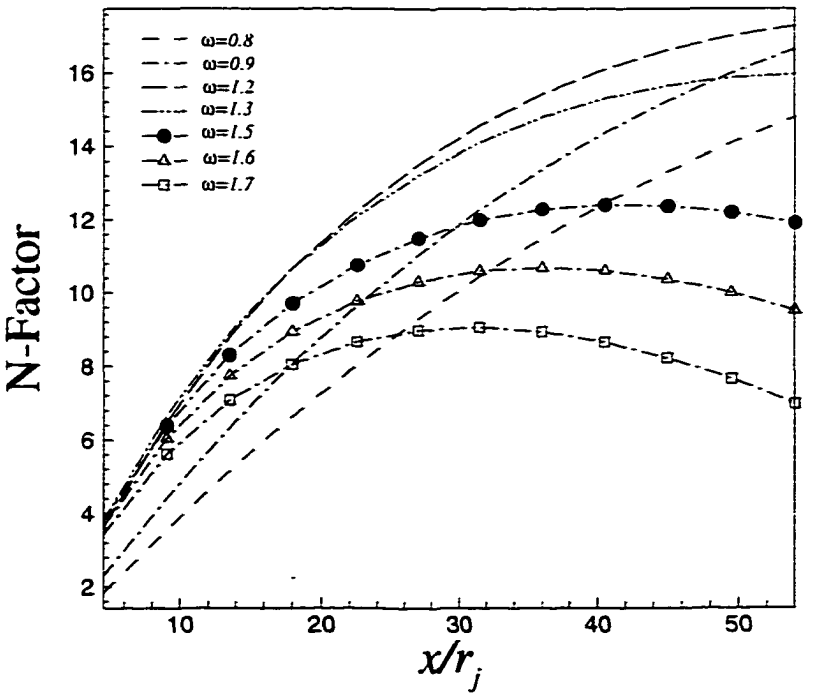

Figure (4.6) N-factor versus downstream position at different frequencies

The eigenfuctions of the disturbance are computed at the fundamental frequency ($\omega = 1.25$) and the first two subharmonics ($\omega = 0.625, 0.3125$) because these

eigenfunctions are needed for the computations of the direct numerical simulation in order to investigate the vortex roll-up and pairings for jet flow as discussed in chapter 5. The results are shown in Fig. (4.7) for the amplitudes of the eigenfunctions at the fundamental frequency only. Similar eigenfunctions are obtained for the first two subharmonics with different amplitudes. The eigenfunctions presented here are normalized with the maximum amplitude of the axial velocity disturbance. The amplitudes of the disturbances peaks around the shear layer ($r/r_j=1$) and decays in the far field as clear from Fig. (4.7).

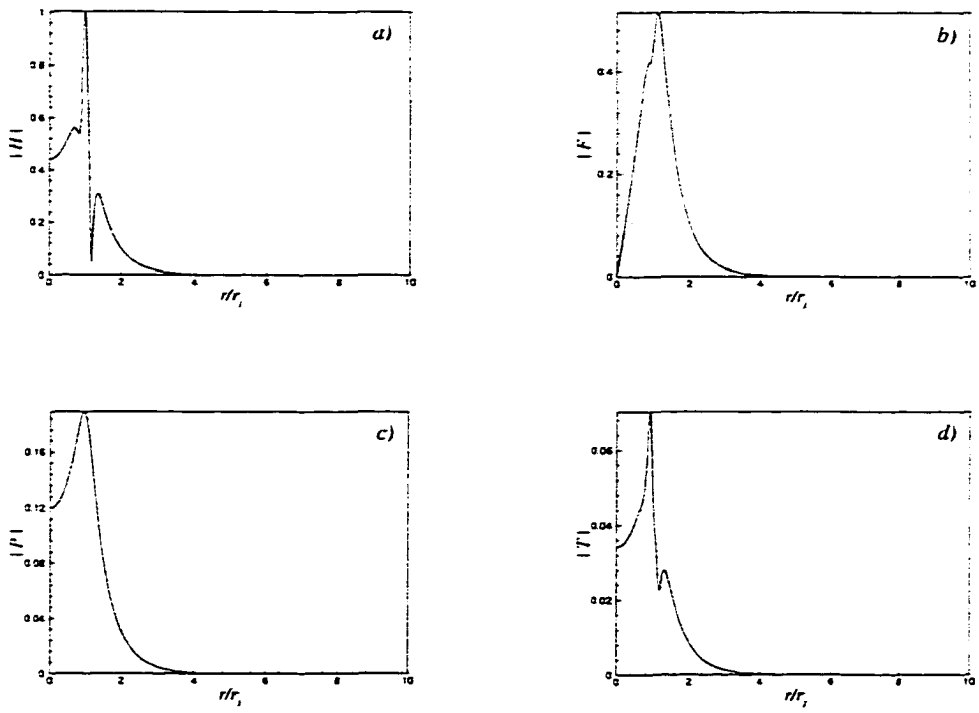

Figure (4.7) amplitudes of the eigenfunctions versus radial position for the most unstable frequency ($\omega = 1.25$) a) axial velocity b) radial velocity c) pressure d) temperature

The linear stability of high subsonic jet ($M_j = 0.85$) with higher Reynolds number ($Re=10^5$) is calculated using the local method. Hot jet is used for the computations with free stream temperature to the jet temperature ratio of 0.365. The mean flow parameters are presented in table (4.2). A computational domain of 55 radius in the axial direction and 27 in the radial direction with 1224×191 grid size are used for

the mean flow and linear stability calculations. The grid is clustered near the shear layer with clustering parameter 4.3.

Table (4.2) Jet mean flow parameters for high subsonic jet (M_j=0.85)

$M_j = \frac{U_j}{\sqrt{\gamma R T_j}}$	$\mathrm{Re} = \frac{U_j \rho_j r_j}{\mu_j}$	$\frac{U_\infty}{U_j}$	$\frac{T_\infty}{T_j}$	Pr	β
0.85	100000	0	0.365	0.72	5

The mean flow variables are plotted in Fig. (4.8) and the results indicate that the jet develops slowly in the axial direction because the Reynolds number is very high and no turbulence models are included in the mean flow computations. Only, laminar boundary-layer equations are solved to compute the jet mean flow.

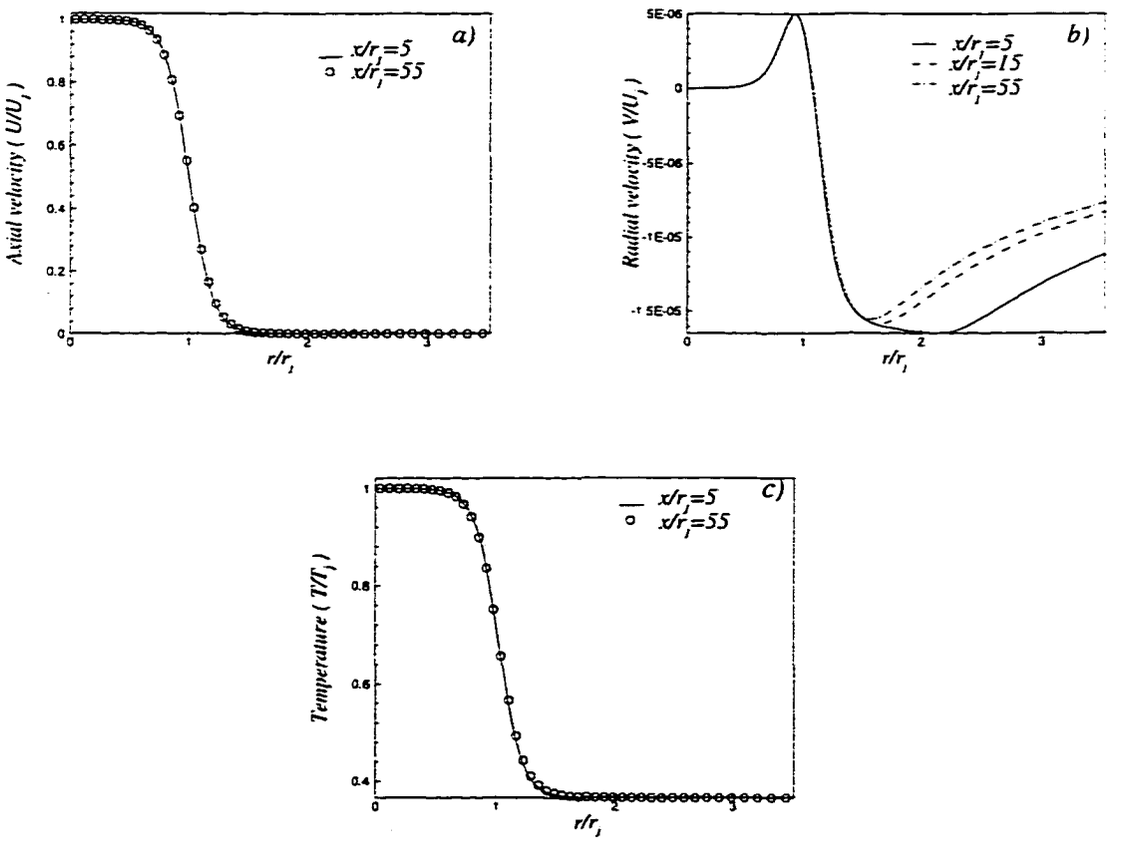

Figure (4.8) Mean flow for subsonic jet (M_j=0.85) and Re=10^5

a) axial velocity b) radial velocity c) Temperature

The results of the spatial stability analysis are presented in Figs. (4.9) and (4.10). A small variation of the growth rate with the downstream position is noticed as a result of the small changes in the jet mean flow. Although, the Reynolds number and the jet temperature ratio are very high, the growth rate is smaller than the growth rate of the lower Mach number jet specially at axial positions close to the nozzle where the mean flow for the lower Reynolds number jet is still undeveloped. Hence, increasing the jet Mach number stabilizes the jet flow. As the axial distance is increased downstream, the growth rate of the lower Reynolds number jet decreases significantly while the change is very small for the higher Reynolds number jet. Hence, a shorter distance is required for the higher Reynolds number jet in order to become turbulent.

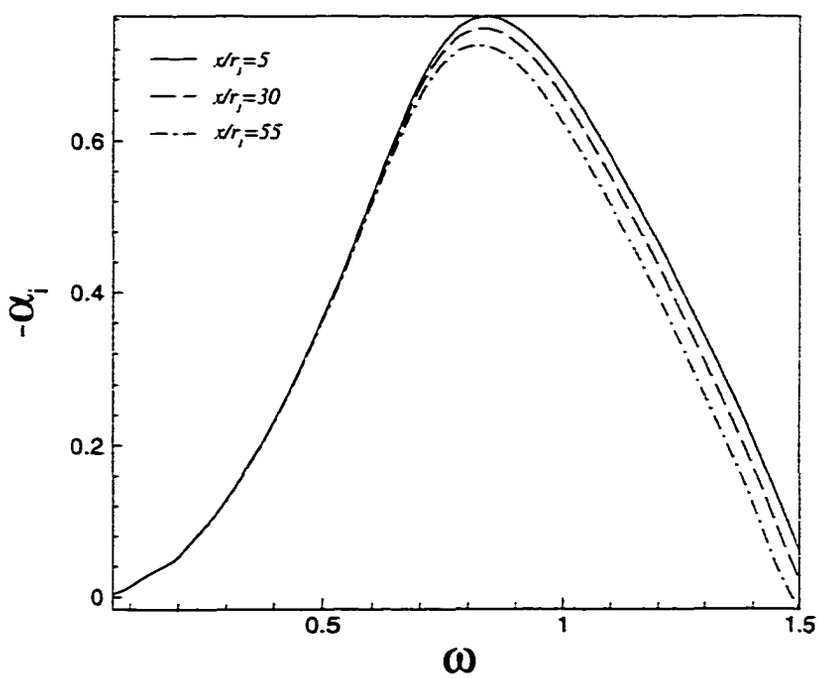

Figure (4.9) Disturbance growth rate versus frequency at different axial locations for subsonic jet (M_j=0.85) and Re=10^5

As a result of low changes of the growth rate with the axial direction for the high Reynolds number jet, the N-Factor varies linearly with the axial distance. The value of N-factor reaches 9 at 12 radius in the axial direction for frequency of 0.85. Hence, the

fundamental frequency for this flow is 0.85, which equals Strouhal number 0.27 and Strouhal number is defined as.

$$St = \frac{f\, d_j}{U_j} = \frac{(\omega^* r_j / U_j)}{\pi} = \frac{\omega}{\pi} \tag{4.39}$$

where, ω is the non-dimensional frequency

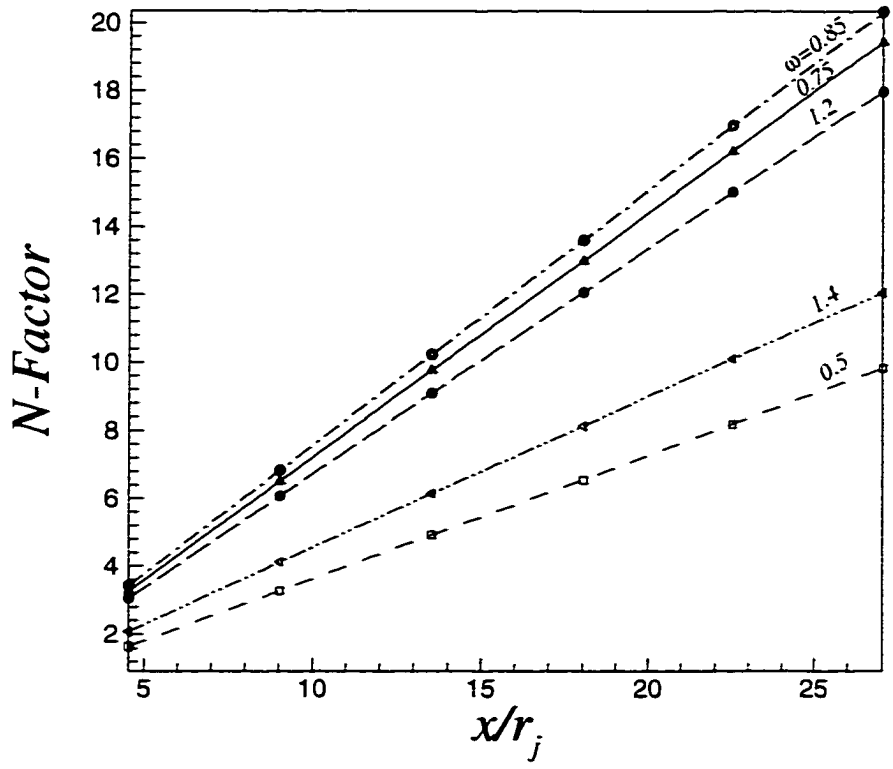

Figure (4.10) N-factor versus axial distance at different frequencies for subsonic jet (M_j=0.85) and Re=10^5

4.4.2 Supersonic Jet

The linear stability of supersonic jet (M_j=2.5) with the low Reynolds number (Re=4350) is introduced in this section. The mean flow parameters are shown in table (4.3). A Cold jet is considered with free stream to jet temperature ratio 2.25 and the momentum thickness of the jet flow is assumed to be very small by assuming the parameter β for the hyperbolic velocity profile to be 11. Higher values for β are

considered and it is found that the results are nearly independent. The Prandtl number is assumed to be constant with the value of 0.72.

Table (4.3) Jet mean flow parameters for supersonic jet (M_j=2.5)

$M_j = \frac{U_j}{\sqrt{\gamma R T_j}}$	$\mathrm{Re} = \frac{U_j \rho_j r_j}{\mu_j}$	$\frac{U_\infty}{U_j}$	$\frac{T_\infty}{T_j}$	Pr	β
2.5	4350	0	2.25	0.72	11

The variation of the growth rate and the wave number with the frequency are presented in Figs. (4.11) and (4.12). As the Mach number is increased to 2.5, the growth rate is decreased which means that increasing the jet Mach number stabilizes the flow. Maximum growth rate (-0.1392) is obtained at frequency 1.103.

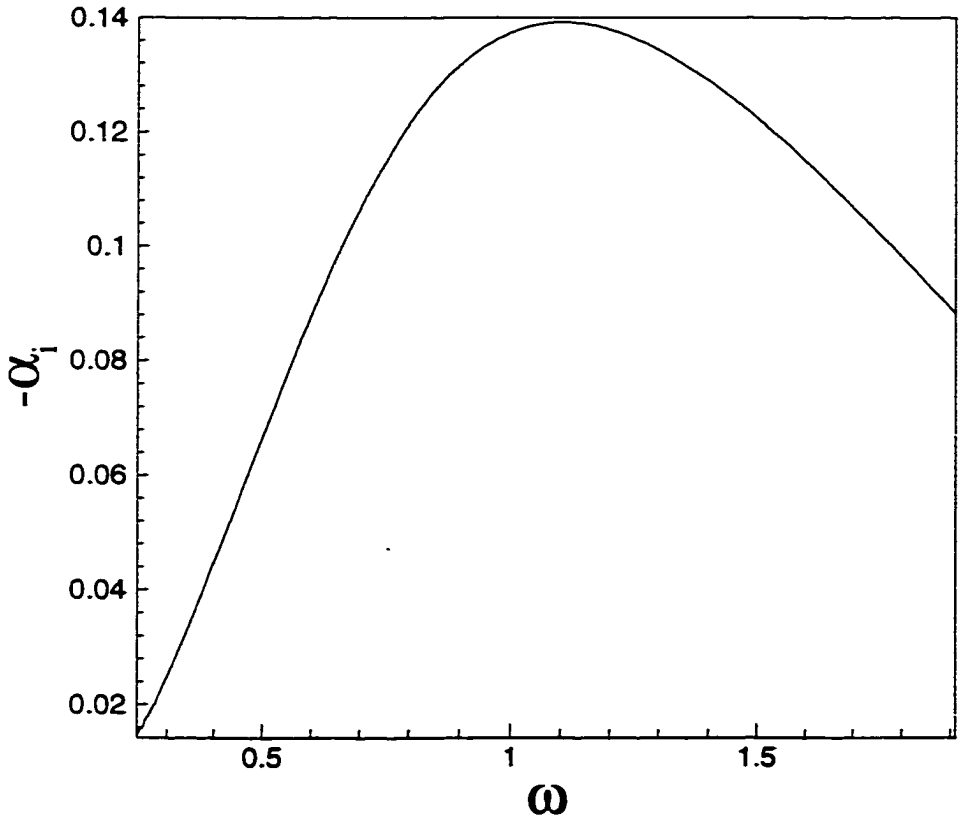

Figure (4.11) Growth rate versus frequency for supersonic jet (M_j=2.5) and Re=4350

The wave number of the disturbance increases with the frequency while the phase speed remains approximately constant. In addition, the results indicate that the phase speed increases slightly as the jet Mach number is increased.

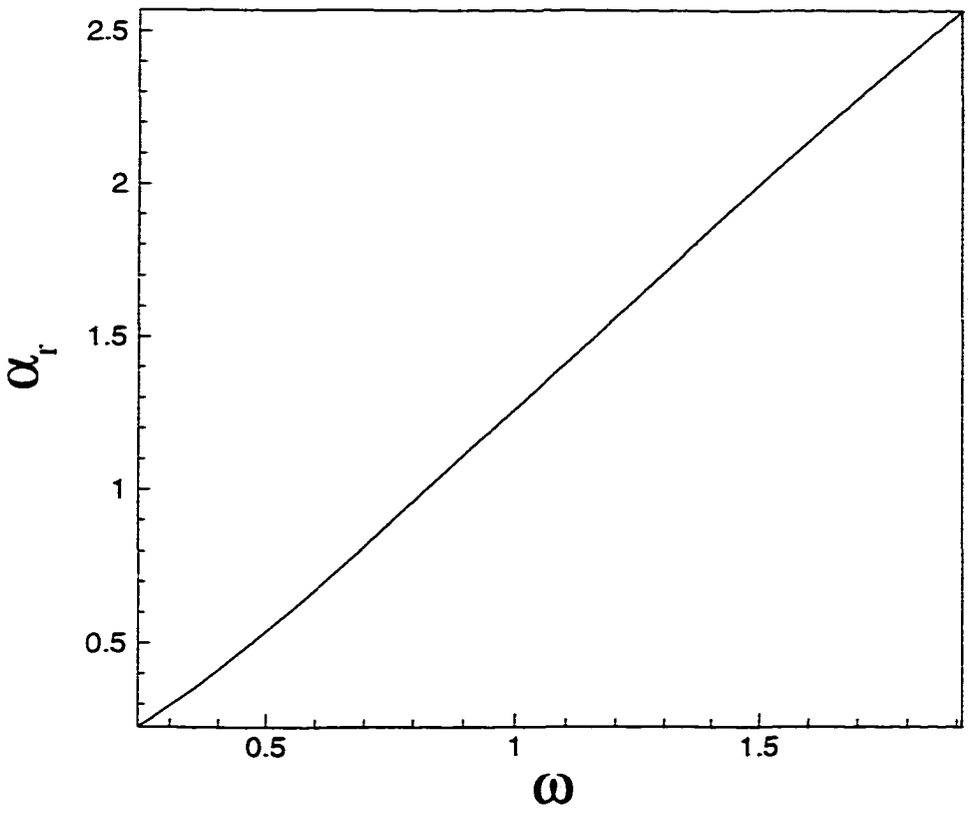

Figure (4.12) Wavenumber versus frequency for supersonic jet (M_j=2.5) and Re=4350

Next, the real values of the disturbances are presented at Strouhal number 0.552 and this Strouhal number is chosen for comparing the direct numerical simulation results with the experimental results where the disturbances are needed at the inflow boundary. The eigenfunctions are normalized with the amplitude of the axial velocity disturbance. Maximum amplitudes of the disturbances are obtained near the critical layer and the disturbances oscillate as they propagate to the far field as shown in Fig. (4.13).

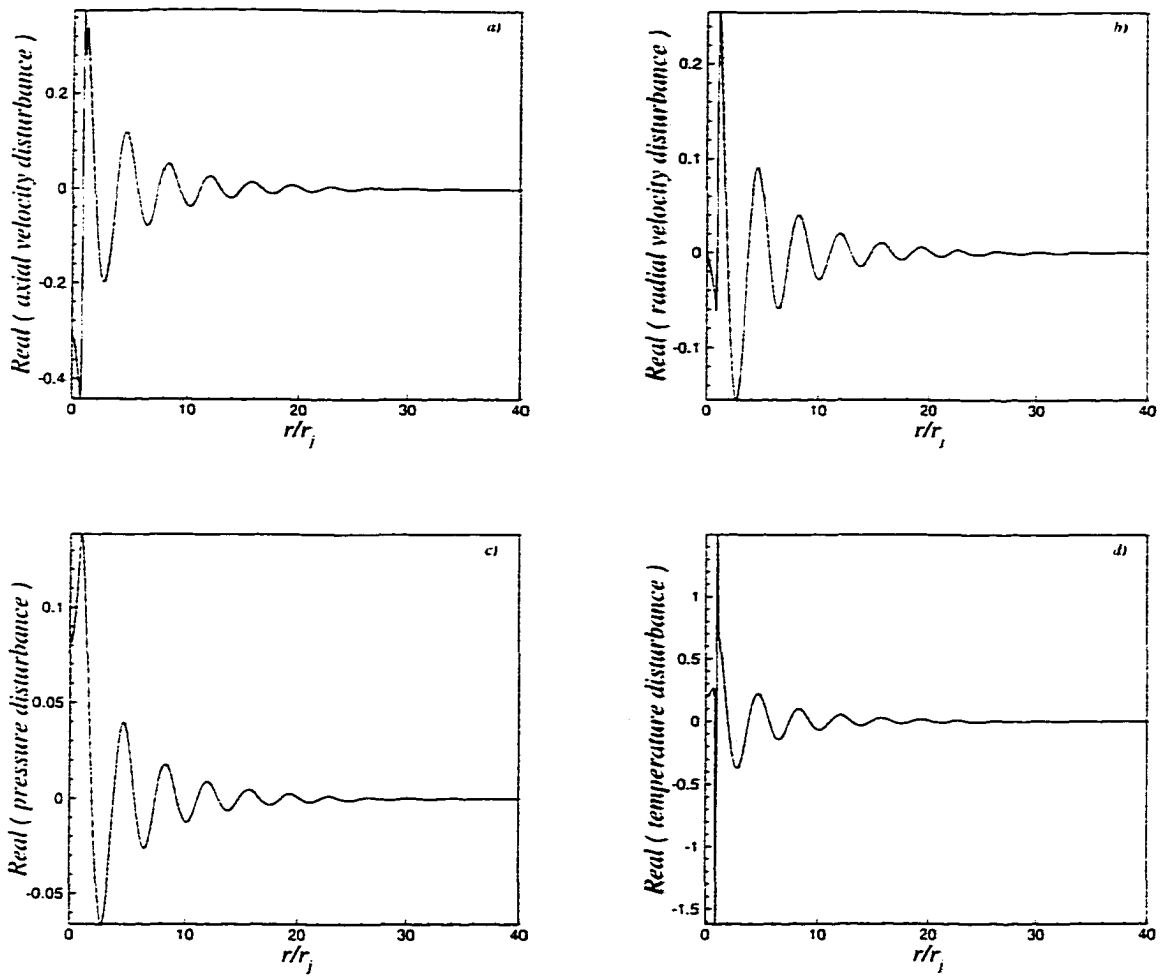

Figure (4.13) Real part of eigenfunctions versus radius for supersonic jet (M_j=2.5) and Re=4350 a) axial velocity b) radial velocity c) pressure d) temperature

Chapter 5

Direct Numerical Simulation

5.1 Introduction

Computations of the noise radiated from the jet mixing layer may be divided into two parts. The first part is the evaluation of the near-field source and the second part is the computations of noise in the far field. Direct numerical simulation (DNS) of the unsteady full Navier-stokes equations is used to obtain the sound source in the near field and part of the acoustic field which can be compared with the linearized wave equation solution.

Experiments have shown that the sound power emitted from the jet is greatest within 4 to 5 diameters downstream and it then decays through a transition region. This region is characterized by large vortical structures and is not fully turbulent, which gives the motivation to solve the unsteady flow equations in the near field to provide the sound source for an acoustic computation of the far field noise. Due to the limitations of the computational facilities available at the present time, the linearized Euler equations or the linearized wave equation are used to calculate the noise in the far field. The linearized Euler equation approach neglects both viscous and nonlinear effects. The viscous effects can be neglected since the free shear layer in the far field is essentially inviscid (Mankbadi 1992). The nonlinear flow effects and source generation are confined to the near field (Shih 1995) and sound propagation in the far-field can be modeled by the linearized Euler equations.

In order to evaluate the sound source using DNS, the simulation must be performed using numerical techniques with minimum distortion and diffusive characteristics. The numerical errors get worse for high Reynolds number flow simulations. Typically, free shear layer flows of interest have very high Reynolds numbers. Therefore, high-order accurate numerical schemes with minimum dissipation

and dispersion errors are needed. Part of the current research is devoted to the investigation of the different numerical schemes for computational aeroacoustics.

The treatment of the boundaries is very important in getting an accurate solution of the Navier-stokes equations. Various computational techniques have been developed to minimize the reflections of the out-going waves. In the current research, different inflow and outflow boundary conditions are used and the results are compared for these methods.

5.2 Governing Equations

Navier-Stokes equations are used to evaluate the near field source of jet noise and to compute the linear and nonlinear instability waves of the mixing layer. The equations are written in conservative form, cylindrical coordinates and for 3-d axisymmetric jet. The jet radius, exit velocity, temperature and density are used to normalize the equations.

$$\frac{\partial Q}{\partial t}+\frac{\partial F}{\partial x}+\frac{1}{r}\frac{\partial (rG)}{\partial r}+\frac{1}{r}\frac{\partial H}{\partial \theta}=S \tag{5.1}$$

$$Q=\begin{bmatrix}\rho\\ \rho u\\ \rho v\\ \rho w\\ \rho E\end{bmatrix}$$

$$F=\begin{bmatrix}\rho u\\ p+\rho u^2-\sigma_{xx}\\ \rho u v-\sigma_{xr}\\ \rho u w-\sigma_{x\theta}\\ (\rho \mathrm{E}+\mathrm{p})u-u\sigma_{xx}-v\sigma_{xr}-w\sigma_{x\theta}-k\dfrac{\partial T}{\partial x}\end{bmatrix}$$

$$G=\begin{bmatrix} \rho v \\ \rho u v-\sigma_{xr} \\ p+\rho v^2-\sigma_{rr} \\ \rho vw-\sigma_{r\theta} \\ (\rho \mathrm{E}+\mathrm{p})v-u\sigma_{xr}-v\sigma_{rr}-w\sigma_{r\theta}-k\dfrac{\partial T}{\partial r} \end{bmatrix}$$

$$H=\begin{bmatrix} \rho w \\ \rho u w-\sigma_{x\theta} \\ \rho vw-\sigma_{r\theta} \\ p+\rho w^2-\sigma_{\theta\theta} \\ (\rho E+p)w-u\sigma_{x\theta}-v\sigma_{r\theta}-w\sigma_{\theta\theta}-\dfrac{k}{r}\dfrac{\partial T}{\partial 6} \end{bmatrix} \qquad S=\frac{1}{r}\begin{bmatrix} 0 \\ 0 \\ p+\rho w^2-\sigma_{\theta\theta} \\ -\rho vw+\sigma_{r\theta} \\ 0 \end{bmatrix}$$

$$p=(\gamma-1)\rho\left[E-\frac{1}{2}(u^2+v^2+w^2)\right] \tag{5.2}$$

$$T=\frac{p}{\gamma M_j^2 \rho} \tag{5.3}$$

Here Q is the unknown vector, F, G, and H are the fluxes in x, r, θ directions, respectively; S is the source term. The shear stresses are expressed as follows

$$\sigma_{xx}=\frac{2\mu}{3\mathrm{Re}}(2\frac{\partial u}{\partial x}-\frac{v}{r}-\frac{\partial v}{\partial r}-\frac{1}{r}\frac{\partial w}{\partial 6})$$

$$\sigma_{rr}=\frac{2\mu}{3\mathrm{Re}}(2\frac{\partial v}{\partial r}-\frac{v}{r}-\frac{\partial u}{\partial x}-\frac{1}{r}\frac{\partial w}{\partial 6})$$

$$\sigma_{\theta\theta}=\frac{2\mu}{3\mathrm{Re}}(2\frac{\partial w}{\partial 6}+\frac{2v}{r}-\frac{\partial u}{\partial x}-\frac{\partial v}{\partial r})$$

$$\sigma_{xr}=\frac{\mu}{\mathrm{Re}}(\frac{\partial u}{\partial r}+\frac{\partial v}{\partial x})$$

$$\sigma_{x\theta} = \frac{\mu}{\mathrm{Re}}\left(\frac{1}{r}\frac{\partial u}{\partial \theta} + \frac{\partial w}{\partial x}\right)$$

$$\sigma_{r\theta} = \frac{\mu}{\mathrm{Re}}\left(\frac{1}{r}\frac{\partial v}{\partial \theta} + \frac{\partial w}{\partial r} - \frac{w}{r}\right) \tag{5.4}$$

$$\text{and} \quad \mathrm{Re} = \frac{\rho_j u_j r_j}{\mu_j}, \quad M_j = \frac{u_j}{\sqrt{\gamma R T_j}} \tag{5.5}$$

The viscosity is calculated using Sutherland's law and the thermal conductivity is obtained by assuming the Prandtl number is constant.

$$\mu = T^{3/2}\frac{1 + 110.4/T_j}{T + 110.4/T_j} \tag{5.6}$$

$$k = \frac{\mu}{(\gamma - 1)M_j^2 \,\mathrm{Pr}\,\mathrm{Re}} \tag{5.7}$$

5.3 Numerical Schemes

The numerical schemes for computational aeroacoustics are expected to propagate waves accurately for long distances over long periods of time. Thus, a certain number of points are required per wave length in order to model all the scales of the unsteady flows and a certain size of time steps is required in order to model the wave movement in time. From the computational standpoint, it is desirable to reduce the number of points required per wave length and to increase the size of the time step. Recently, many numerical schemes have been developed for the computational aeroacoustics. One of the well-known schemes is the two-four dissipative scheme which is developed by Gottlieb and Turkel (1976). This scheme is a modification of the second order MacCormack scheme and it is fourth order accurate in space and second order accurate in time. The two-four scheme has been used successfully by Farouk and Oran (1991), Ragab and Sheen (1991), Mankbadi et al (1994) and many others for solving fluid and aeroacoustic problems. The scheme uses operator splitting for the flux and the operators are alternated symmetrically to maintain the fourth order accuracy. Thus, the operators will be alternated with symmetrical variants. Let L_1 be the operator with forward finite difference in the first step and backward finite difference in the second step, then L_2 is the operator with backward

finite difference in the first step and forward finite difference in the second step. The operators are applied in the following symmetric way:

$$Q^{n+2} = L_{2x}L_{2r}L_{2\theta}L_{1\theta}L_{1r}L_{1x}Q^{n} \tag{5.8}$$

Where n, $n+2$ denote the time levels; L_x, L_r and L_θ are one-dimensional operators in x, r and θ directions that are applied to the following one-dimensional equations

$$Q_t = - F_x \tag{5.9}$$

$$Q_t = - G_r + S \tag{5.10}$$

$$Q_t = - H_\theta \tag{5.11}$$

Using second-order Runge Kutta for the time integration and fourth-order accurate finite difference for the flux terms, the operator L_{1x} is used to applied to Eq. (5.9) as follows:

$$\begin{aligned} Q^{*} &= Q^{n} - \frac{\Delta t}{6\Delta x}[7F_i - 8F_{i+1} + F_{i+2}]^{n} \\ Q^{**} &= \frac{1}{2}\{Q^{*} + Q^{n} - \frac{\Delta t}{6\Delta x}[-7F_i + 8F_{i-1} - F_{i-2}]^{*}\} \end{aligned} \tag{5.12}$$

Similar equations are written for the operators L_{1r} and $L_{1\theta}$ to discretize the fluxes in r and θ directions and the operator L_{2x} is used in the following way:

$$\begin{aligned} Q^{o} &= Q^{n+1} - \frac{\Delta t}{6\Delta x}[-7F_i + 8F_{i-1} - F_{i-2}]^{n+1} \\ Q^{oo} &= \frac{1}{2}\{Q^{o} + Q^{n+1} - \frac{\Delta t}{6\Delta x}[7F_i - 8F_{i+1} + F_{i+2}]^{o}\} \end{aligned} \tag{5.13}$$

The two-four scheme has been extended to two-sixth by Bayliss (1985). Thus, the spatial accuracy of the scheme is increased to sixth order by adding another point to the finite difference of the fluxes as follows:

$$Q^{*} = Q^{n} - \frac{\Delta t}{30\Delta x}[37F_i - 45F_{i+1} + 9F_{i+2} - F_{i+3}]^{n}$$
$$Q^{**} = \frac{1}{2}\{Q^{*} + Q^{n} - \frac{\Delta t}{30\Delta x}[-37F_i + 45F_{i-1} - 9F_{i-2} + F_{i-3}]^{*}\} \tag{5.14}$$

Using the basic methodology of the 2-4 and 2-6 schemes, a new family of MacCormack type schemes has been developed by Hixon (1997) to optimize the dispersion error and to reduce the dissipation of the schemes. By adding a point to the one-sided difference in the opposite direction with the unknown (a_{-1}) and using optimized dispersion relation, three new schemes are developed as shown in table (5.1). The finite difference of the flux for these schemes is written in this form.

$$\left(\frac{dF}{dx}\right)^{f} = a_{-1}F_{i-1} + a_0F_i + a_1F_{i+1} + a_2F_{i+2} + a_3F_{i+3}$$
$$\left(\frac{dF}{dx}\right)^{b} = a_{-1}F_{i+1} + a_0F_i + a_1F_{i-1} + a_2F_{i-2} + a_3F_{i-3} \tag{5.15}$$

Table (5.1) Coefficients for MacCormack type schemes

Scheme	a_{-1}	a_0	a_1	a_2	a_3
2/4	*0*	$\frac{-7}{6\Delta x}$	$\frac{8}{6\Delta x}$	$\frac{-1}{6\Delta x}$	*0*
2/6	*0*	$\frac{-37}{30\Delta x}$	$\frac{45}{30\Delta x}$	$\frac{-9}{30\Delta x}$	$\frac{1}{30\Delta x}$
4/4	$\frac{-2}{6\Delta x}$	$\frac{-3}{6\Delta x}$	$\frac{6}{6\Delta x}$	$\frac{-1}{6\Delta x}$	*0*
4/6	$\frac{-9}{30\Delta x}$	$\frac{-19}{30\Delta x}$	$\frac{36}{30\Delta x}$	$\frac{-9}{30\Delta x}$	$\frac{1}{30\Delta x}$
DRP/opt	$\frac{-.30874}{\Delta x}$	$\frac{-.63254}{\Delta x}$	$\frac{1.2330}{\Delta x}$	$\frac{-.3334}{\Delta x}$	$\frac{.04168}{\Delta x}$

Moreover, the accuracy of the time integration for MacCormack schemes has been increased up to fourth-order accurate in time by using Runge Kutta method as follows:

$$Q_t = -\frac{d}{dx}[F(Q)]$$

$$h_1 = -\Delta t \frac{d}{dx}^{f} [F(Q^n)]$$

$$h_2 = -\Delta t \frac{d}{dx}^{b} [F(Q^n + \alpha_2 h_1)]$$

$$h_3 = -\Delta t \frac{d}{dx}^{f} [F(Q^n + \alpha_3 h_2)]$$

$$h_4 = -\Delta t \frac{d}{dx}^{b} [F(Q^n + \alpha_4 h_3)]$$

$$h_5 = -\Delta t \frac{d}{dx}^{f} [F(Q^n + \alpha_5 h_4)]$$

$$h_6 = -\Delta t \frac{d}{dx}^{b} [F(Q^n + \alpha_6 h_5)]$$

$$Q^{n+1} = Q^n + \beta_1 h_1 + \beta_2 h_2 + \beta_3 h_3 + \beta_4 h_4 + \beta_5 h_5 + \beta_6 h_6 \qquad (5.16)$$

Table (5.2) Coefficients for Runge Kutta time integration

	α_2	α_3	α_4	α_5	α_6	β_1	β_2	β_3	β_4	β_5	β_6
Second order	*1*	*0*	*0*	*0*	*0*	*1/2*	*0*	*0*	*0*	*0*	*0*
Fourth order	*1/2*	*1/2*	*1*	*0*	*0*	*1/6*	*1/3*	*1/3*	*1/6*	*0*	*0*
(4-6) First step	*1/2*	*1/2*	*1*	*0*	*0*	*1/6*	*1/3*	*1/3*	*1/6*	*0*	*0*
Second step	*.353*	*.999*	*.152*	*.534*	*.604*	*.047*	*.137*	*.171*	*.197*	*.282*	*.165*

5.4 Boundary conditions

Direct numerical simulation of the unsteady full Navier-Stokes equations is strongly dependent on the boundary conditions and on their treatment. An accurate control of wave reflections from the boundaries of the computational domain is required for the unsteady computations. Several methods have been suggested for the treatment of the inflow and outflow boundaries. These methods include characteristic boundary conditions, buffer domain and perfectly matching layer technique. Some of these boundary conditions are examined in the next subsections.

5.4.1 Inflow Boundary Conditions

Nonreflecting inflow boundary conditions are based on specifying the incoming and the outgoing characteristics. For supersonic flow, all the characteristics are incoming and hence all the flow variables are specified at the inflow boundary as mean flow Q_m and disturbance Q_{dist} which is obtained from the linear stability analysis at certain frequency ω. In some cases, the disturbances are introduced at the inflow boundary for the fundamental frequency ω and its first two subharmonics $\omega/2$ and $\omega/4$ in order to investigate the sound generated by vortex roll-up and pairings.

$$Q = Q_m + \varepsilon Q_{dist}$$

$$Q_{dist} = \sum_{k=1}^{3} Real\,[\,Q_k(r)e^{-i\omega t/2^{k-1}+in\theta}\,] \qquad (5.17)$$

$$\varepsilon << Q_k(r)$$

where $Q_k(r)$ are the eigenfunctions of the flow variables which are obtained from the linear stability code for the most unstable frequency ω and its subharmonics $\omega/2$ and $\omega/4$ and n is the azimuthal wave number; ε is the amplitude of the disturbance at the inflow boundary.

For subsonic flow, one flow variable is obtained from the interior domain using the continuity equation and the rest of the flow variables are specified at the boundary as

in Eq. (5.17). The continuity equation is used in the characteristic form to obtain the density at the inflow boundary.

$$\frac{\partial \rho}{\partial t}+[\lambda_2+\frac{1}{2}(\lambda_1+\lambda_5)]/c^2+\frac{\partial \rho v}{\partial r}+\frac{1}{r}\frac{\partial \rho w}{\partial \theta}=-\frac{\rho v}{r} \tag{5.18}$$

where,

$$\lambda_1=(u-c)(\frac{\partial p}{\partial x}-\rho u\frac{\partial u}{\partial x})$$

$$\lambda_2=u(c^2\frac{\partial \rho}{\partial x}-\frac{\partial p}{\partial x}) \tag{5.19}$$

$$\lambda_5=(u+c)(\frac{\partial p}{\partial x}+\rho c\frac{\partial u}{\partial x})$$

For non-reflecting inflow boundary conditions, $\lambda_2=\lambda_5=0$ and λ_1 is calculated from the interior points.

5.4.2 Centerline Conditions

At the centerline, the governing equations are singular and a treatment for the equations is required to overcome the singularities. For two-dimensional axisymmetric jet, a new set of equations is easily derived at the centerline using L'Hospital rule. These equations require using the following symmetrical conditions, which are used to obtain the flux at the ghost points near the centerline.

$$\frac{\partial p}{\partial r}=\frac{\partial u}{\partial r}=\frac{\partial \rho}{\partial r}=0 \tag{5.20}$$

$$v=0$$

Different techniques have been used to overcome the singularity at the centerline for the three-dimensional Navier-Stokes equations in polar coordinates. Shih, Hixon and Mankbadi (1995) used three different methods for the jet centerline treatment. One of these method is using the average values of the flow variables on the ring r=Δr. Prior to taking the average on the ring r=Δr, some conditions have to be imposed on the ring r=0

based on the physics of the flow at the centerline. The first condition is obtained by noticing that the multivalued nature of the flowfield doesn't extend to pressure, temperature, density and axial component of the velocity. The radial and azimuthal components of velocity have multivalued at the centerline (Griffin et al 1979). The second condition is derived from the fact that true velocity vector through any point can have only one direction in physical space, since in the jet problem there is a symmetry plane (x, r plane) through which there can be no mass flow. If the velocity vector at a given point x on the centerline has the value U_{avg} , then the radial and azimuthal components (v , w) must be calculated from.

$$\begin{aligned} v(x,r,\theta) &= U_{avg}\cos\theta \\ w(x,r,\theta) &= -U_{avg}\sin\theta \end{aligned} \tag{5.21}$$

To determine U_{avg} , one computes the average of the velocity vector U on the ring using

$$U(x,r,\theta) = v(x,r,\theta)\cos\theta - w(x,r,\theta)\sin\theta \tag{5.22}$$

The average on the ring r=Δr is computed using the equation:

$$q_{i,1,l} = \frac{1}{k\max}\sum_{k=1}^{k\max} q_{i,2,k} \quad , \; i=1,imax \text{ and } l=1,kmax \tag{5.23}$$

where, $q = (\rho\, u\, U\, p\, T\, E)^t$ (5.24)

Another technique, which is used by Shih et al (1995), is to consider the centerline as an interior point with very small radius $r=\varepsilon$ and the same governing equations are used. A severe restriction on the time step is caused by this method due to stability requirements of the numerical schemes and larger values for ε should be used.

A different method is used by Freund et al (1997), which is adopted also in the current research due to its accuracy. The singularity at the centerline is treated in this technique

by using Navier-stokes equations in Cartesian coordinates at the centerline only. Therefore, a transformation between the two coordinates for the flow variables is required. The Cartesian grid is formed at the centerline with grid points coinciding with those at $\theta=0,\ \pi/2,\ \pi,\ 3\pi/2$ of the cylindrical grid as shown in Fig. (5.1).

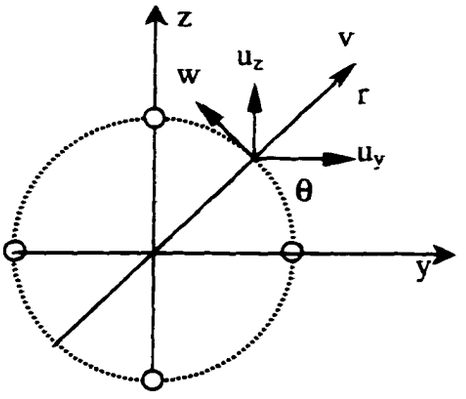

Figure (5.1) Coordinate systems used at the centerline.

The following transformations are used to switch between the two coordinates:

$$\begin{bmatrix} u_y \\ u_z \end{bmatrix} = \begin{bmatrix} \cos\theta & -\sin\theta \\ \sin\theta & \cos\theta \end{bmatrix} \begin{bmatrix} v \\ w \end{bmatrix} \quad , \quad \begin{bmatrix} v \\ w \end{bmatrix} = \begin{bmatrix} \cos\theta & \sin\theta \\ -\sin\theta & \cos\theta \end{bmatrix} \begin{bmatrix} u_y \\ u_z \end{bmatrix} \tag{5.25}$$

For an axisymmetric jet with symmetric disturbances, the normal velocity component, u_z, is zero and hence the z-momentum equation at the centerline is replaced by the mentioned condition. Thus, the radial and azimuthal velocity components are calculated from

$$\begin{aligned} v &= \cos\theta\ u_y \\ w &= -\sin\theta\ u_y \end{aligned} \tag{5.26}$$

All other flow variables are single valued at the centerline and no transformations for these variables are needed to switch between the two systems.

5.4.3 Outflow Boundary Conditions

5.4.3.1 Thompson's Characteristic Boundary Conditions

The characteristic boundary conditions are specified at the outflow boundary by writing the governing equations in a characteristic form and specifying the outgoing and incoming waves to the computational domain. The outgoing waves are defined by the solution at and within the boundary, and no boundary conditions can be specified for them. The incoming waves depend on the solution exterior to the boundary and therefore require boundary conditions to complete the specification of their behavior. Hence, the governing Eqs. (5.1) are written at the outflow boundary in the following characteristic form.

$$\frac{\partial Q}{\partial t}+d+\frac{1}{r}\frac{\partial rG}{\partial r}+\frac{1}{r}\frac{\partial H}{\partial \theta}=C_x+S \tag{5.27}$$

where, d is the amplitude of the characteristic waves and C_x is the shear stresses in x-direction.

$$d_1=[\lambda_2+(\lambda_1+\lambda_5)/2]/C^2 \tag{5.28a}$$

$$d_2=ud_1+(\lambda_5-\lambda_1)/2C \tag{5.28b}$$

$$d_3=vd_1+\rho\,\lambda_3 \tag{5.28c}$$

$$d_4=wd_1+\rho\,\lambda_4 \tag{5.28d}$$

$$d_5=\frac{1}{2}(u^2+v^2+w^2)*d_1+\rho\,ud_2+\rho\,vd_3+\rho\,wd_4+(\lambda_5+\lambda_1)/[2(\gamma-1)] \tag{5.28e}$$

The characteristic waves (λi) represent acoustic, entropy and vorticity waves, and are described by these equations

$$\lambda_1=(u-c)(\frac{\partial p}{\partial x}-\rho\,c\frac{\partial u}{\partial x}) \qquad \lambda_2=u(c^2\frac{\partial \rho}{\partial x}-\frac{\partial p}{\partial x})$$

$$\lambda_3=u\frac{\partial v}{\partial x} \qquad \lambda_4=u\frac{\partial w}{\partial x} \tag{5.29}$$

$$\lambda_5=(u+c)(\frac{\partial p}{\partial x}+\rho\,c\frac{\partial u}{\partial x})$$

For nonreflecting outflow boundary conditions, all the incoming characteristics are set equal to zero and the outgoing characteristics are calculated from the interior points. Hence, for supersonic outflow, all the characteristics are running out of the domain and no boundary conditions are needed, while for subsonic outflow, λ_1 is coming into the domain and it is set equal to zero. Similar equations are obtained for the characteristics running in r-direction at r_{max}.

5.4.3.2 Outflow Boundary [proposed by Rudy and Strikwerda (1980)]

In these boundary conditions, a pressure correction term is added to the incoming waves in order to keep the pressure at the outflow close to the mean value. The wave reflection from the outflow boundary is determined by specifying the incoming wave. Hence, the incoming wave is corrected as follows:

$$\lambda_1 = K(p - p_m) \tag{5.30}$$

$$K = \frac{\sigma(1-M_{\max}^2)C}{L} \tag{5.31}$$

where, M_{max} is the maximum Mach number in the flow field, C is the local speed of sound, L is a characteristic dimension of the domain, and σ is nonreflecting parameter ranges between zero and one.

5.4.3.3 Buffer Domain Boundary conditions

The buffer domain technique is proposed by Streett and Macaraeg (1989). The technique is based on gradually reducing the ellipticity of the Navier-Stokes equation in a buffer region while solving the governing equations without modifications in the domain of interest. The sources of the ellipticity in the equations are the streamwise shear stresses and the pressure terms. To deal with these sources, the streamwise viscous terms and the pressure derivative in the streamwise direction are smoothly reduced to zero through multiplication by the following attenuation function:

$$S_j = \frac{1}{2}[1+\tanh\{4(1-2\frac{j-N_b}{N_x-N_b})\}] \tag{5.32}$$

where N_b marks the beginning of the buffer domain and N_x marks the outflow boundary location.

Additionally, the convective velocity in the nonlinear advection terms is modified in the buffer domain to involve the mean flow velocity only at outflow. This is also done via a smooth coefficient function.

5.4.3.4 Perfectly Matching Layer

This method is first proposed by Berenger (1994) for the absorption of electromagnetic waves and applied by Hu (1995) for Euler equations. In this technique, a region is attached to the computational domain at the boundaries as shown in Fig. (5.2) where exponential damping terms are added to the governing Eq. (5.1) to damp the disturbance.

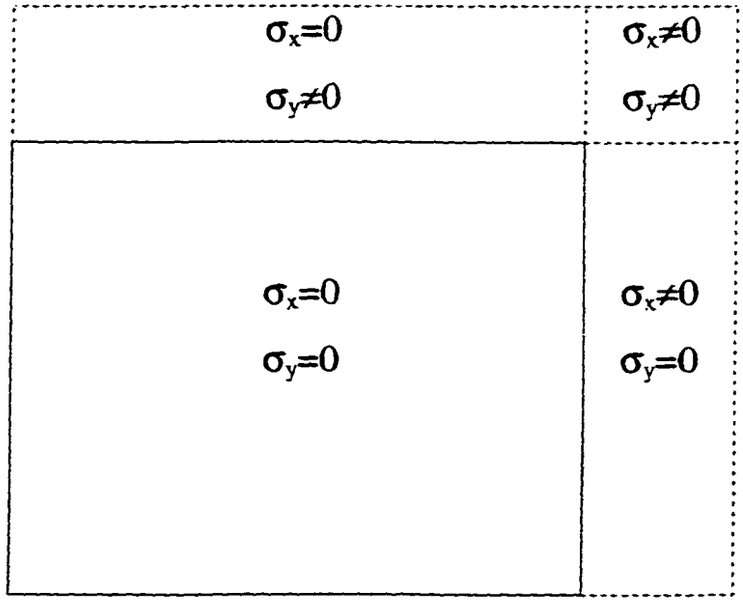

Figure (5.2): Computational Domain

For two-dimensional axisymmetric jet, the governing equations are divided into two equations; one for the disturbance which is produced by the axial flux and the other for the radial flux.

$$\frac{\partial Q_1}{\partial t}+\frac{\partial (F-F_m)}{\partial x}+\sigma_x Q_1 = 0$$

$$\frac{\partial Q_2}{\partial t}+\frac{1}{r}\frac{\partial r(G-G_m)}{\partial r}+\sigma_y Q_2 = (S-S_m) \qquad (5.33)$$

$$Q = Q_1 + Q_2 + Q_m$$

where, $\sigma_x = \sigma_{mx}(\frac{x-x^*}{L_b})^{\beta_x}$ (5.34)

σ_{mx} is the maximum value of the absorption coefficient σ_x, L_b is the length of PML and x^* is the beginning of the Layer. Q_m, F_m, G_m and S_m denote the mean flow variables.

The parameters, σ_{mx} and L_b, of the layer can be adjusted for the desired absorption. The choice of β_x depends on the balance of two factors, namely, the variation of σ_x in the layer and the effectiveness of the layer [Hu (1996)]. Experience suggests that a value of $\sigma_{mx}(\frac{L_b}{\beta_x+1}) \approx 8$ would give satisfactory results.

5.5 Numerical Filtering

For high Reynolds number simulations, the high frequency oscillations grow without limit and cause the numerical schemes to be unstable. Hence, it is desirable to damp the amplitudes of the short waves only without affecting the accuracy of the solution. A sixth order numerical filter is used in the current research for some cases to eliminate the high frequency oscillations. Using the Fourier transform, the following filter is proposed by Hu (1996).

$$\overline{Q}_i = Q_i - [\frac{5}{16}(Q_i - Q_{i,m}) - \frac{15}{64}(Q_{i+1} - Q_{i+1,m}) - \frac{15}{64}(Q_{i-1} - Q_{i-1,m}) + \frac{3}{32}(Q_{i+2} - Q_{i+2,m})$$
$$+ \frac{3}{32}(Q_{i-2} - Q_{i-2,m}) - \frac{1}{64}(Q_{i+3} - Q_{i+3,m}) - \frac{1}{64}(Q_{i-3} - Q_{i-3,m})] \quad (5.36)$$

where $\overline{Q_i}$ is the filtered total conservative variables and $Q_{i,m}$ is the mean conservative variables.

Chapter 6

Two-Dimensional Axisymmetric Jet Simulations

This chapter presents the results of the jet noise computations in the near field and part of the acoustic field which are obtained using the direct numerical simulation of the unsteady full Navier-Stokes equations. The results are first introduced for numerical schemes and boundary conditions comparisons. Then, simulations of two-dimensional subsonic and supersonic jets with axisymmetric disturbances are presented and the data are analyzed in the near and far fields using the Fourier transform of the time signals.

6.1 Numerical Schemes Comparison

MacCormack schemes with different accuracy are introduced for the jet simulation in chapter 5. A comparison between these schemes is presented for a different number of points per wavelength. A two-dimensional axisymmetric jet with supersonic Mach number (M_j =1.5) and very high Reynolds number (Re=1.27×10^6) is considered for the comparison. The jet freestream velocity is assumed to be 0.7 with temperature ratio equals one. The following initial mean velocity profile is assumed for the mean flow calculations:

$$U = 0.5[1.7 - 0.3\tanh\{4(r-1)\}] \tag{6.1}$$

The results obtained from the linear stability analysis show that the fundamental frequency for this jet is 1.6375, the growth rate is - 0.09554 and the spatial wave length is 3.4. Hence, inflow disturbances for axial and radial velocities, pressure, and temperature are introduced at the fundamental frequency to the direct numerical simulation code and the amplitude of the inflow disturbance is taken 0.006. Two different cases are investigated for the different numerical schemes with different number of points per wavelength. A computational domain of 50 radius in the axial direction and 5 radius in the radial direction is used for the jet simulation. The grid size is 251×111 for the first

case which corresponds to 17 points per wavelength in the axial direction and the grid is clustered in the radial direction at the critical layer. The number of points per wavelength is decreased to 9 points for the second case.

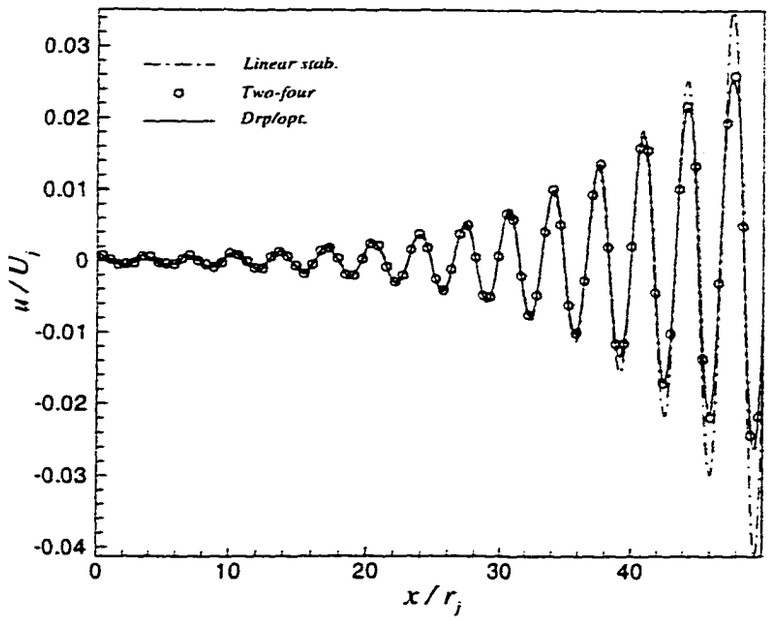

Figure (6.1) Axial velocity disturbance versus axial distance for different numerical schemes with 17 points per wavelength (M_j=1.5, Re=1.27×10^6)

A comparison between MacCormack type schemes and the linear stability is shown in Figs. (6.1) and (6.2). The results indicate that there is an excellent agreement between the two-four scheme, the optimized dispersion relation preserving scheme and the linear stability for a grid size of 17 points per wavelength in the axial direction. As the amplitude of the disturbance grows, the linear stability results deviate from the results obtained using MacCormack schemes because the linear stability theory is not valid for high disturbances. Similar results for the pressure disturbance growth with the axial distance is presented in Fig. (6.2). The graph indicates that the dispersion and dissipation errors are minimized as the number of points are increased in the axial direction and the low accuracy schemes have the same behavior as high accuracy MacCormack schemes with enough number of points per wavelength.

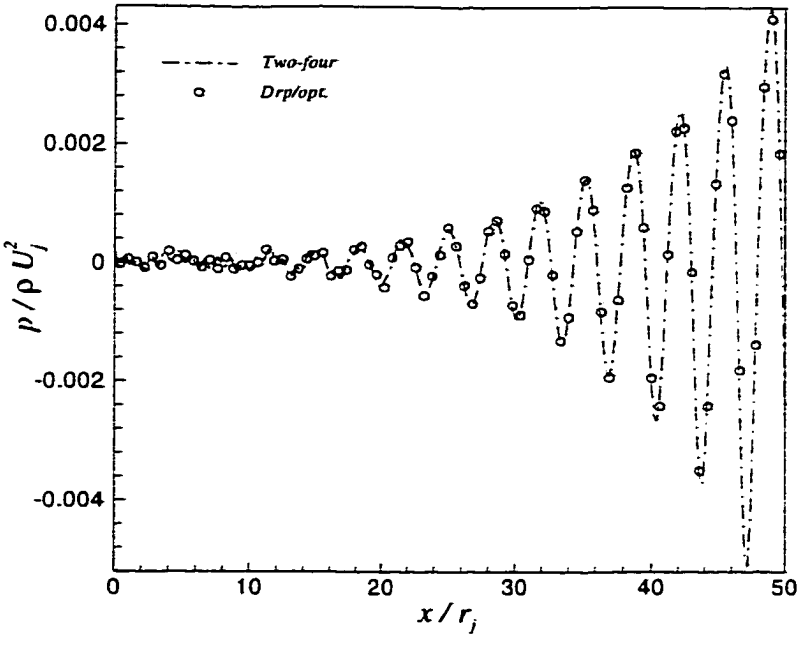

Figure (6.2) Pressure disturbance versus axial distance for different numerical schemes with 17 points per wavelength (M_j=1.5, Re=1.27×10^6)

The dispersion relation preserving scheme results for 17 points are taken as a reference solution for the comparison with the other schemes at the coarser grid. As the grid size in the axial direction is reduced to 9 points per wavelength, the two-four scheme has a high dispersion error compared with the optimized dispersion relation preserving scheme. In addition, the amplitude of the axial velocity disturbance for the two-four scheme is higher than that obtained by DRP scheme as shown in Fig. (6.3). The numerical errors of the two-four scheme get worse as the number of points per wavelength is reduced. Fig. (6.4) presents the dispersion preserving scheme results for two different grid sizes. No phase error is noticed for the dispersion preserving scheme with 9 points per wavelength while a small change in the disturbance amplitude is obtained as a result of the dissipation error. The results are still very good compared with the two-four scheme for 9 points.

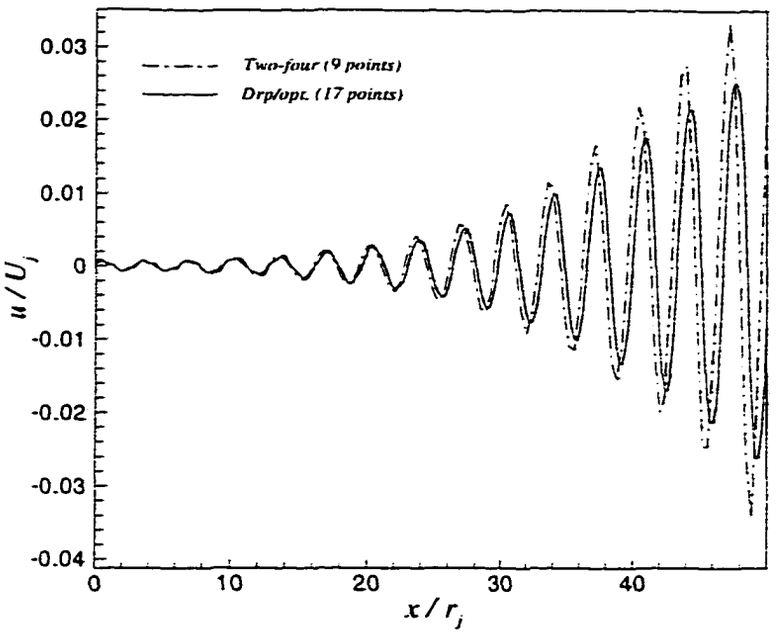

Figure (6.3) Axial velocity disturbance versus axial distance for 2-4 and DRP schemes with different grid size

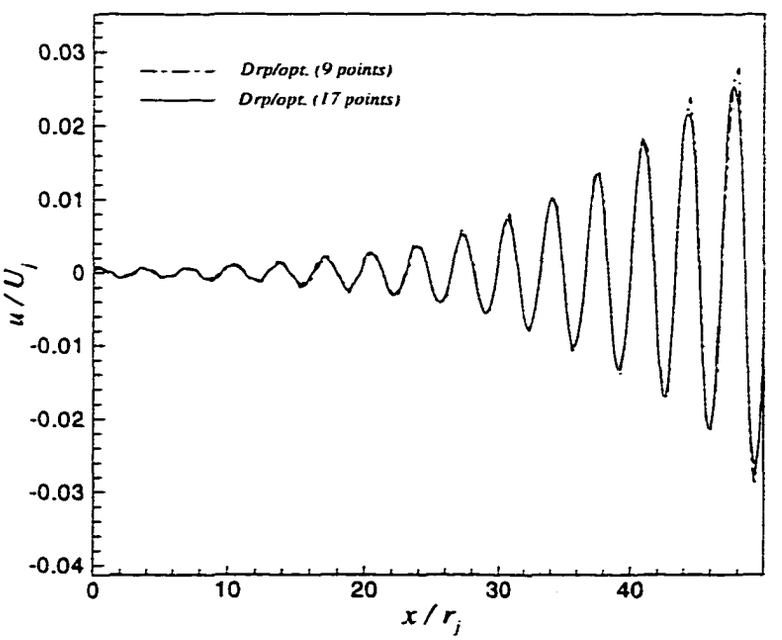

Figure (6.4) Axial velocity disturbance versus axial distance for DRP scheme

A comparison between the two-six scheme and the dispersion preserving scheme is introduced in Fig. (6.5). The results indicate that the dispersion error for the two-six scheme with the coarse grid is lower than that of the two-four scheme with the same grid size and the amplitude of the axial velocity disturbance is relatively higher than that of the dispersion preserving scheme for the fine grid. A higher dispersion error is obtained for the two-six scheme compared with the dispersion preserving scheme.

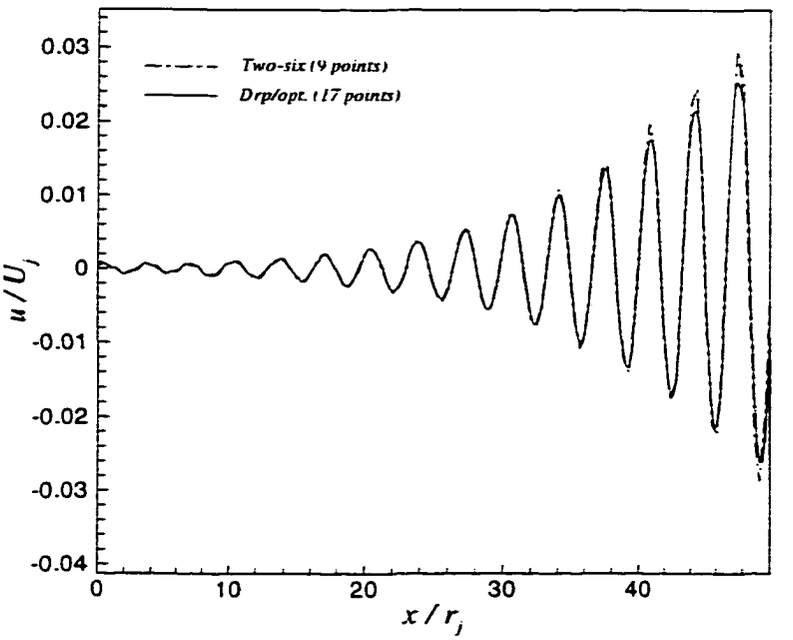

Figure (6.5) Axial velocity disturbance versus axial distance for 2-6 and DRP schemes with different grid size

Although, the four-six scheme is an optimized version of the two-six scheme, similar results of the disturbance growth are predicted for both schemes and the results presented in Fig. (6.6) indicate that a small dispersion error is obtained with the four-six scheme. In addition, the amplitude of the disturbance is relatively different than the reference solution. However, the two-six and four-six schemes are much better than the two-four scheme, the best results are predicted with the optimized dispersion-preserving scheme. All the comparisons are done in the linear stability region whereas a higher number of points per wavelength is required in the nonlinear region where the disturbance amplitude is very high.

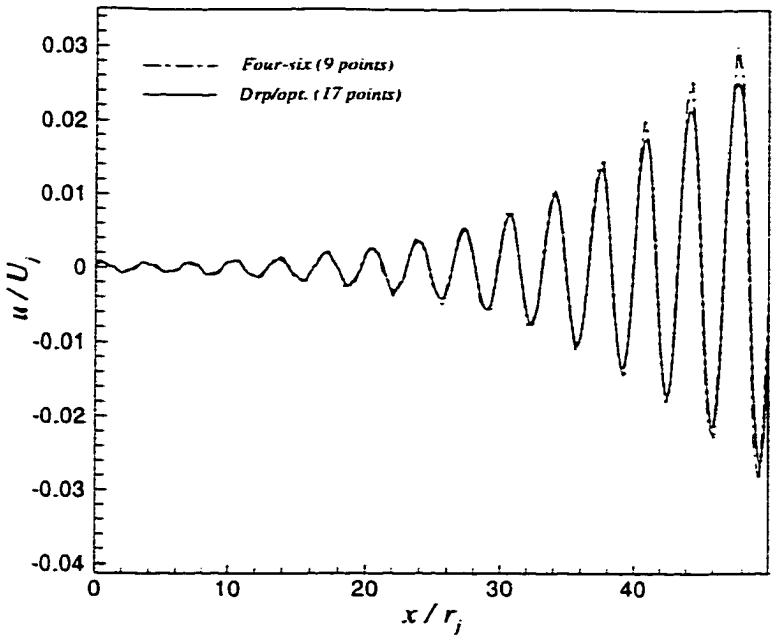

Figure (6.6) Axial velocity disturbance versus axial distance for 4-6 and DRP schemes with different grid size

6.2 Boundary Conditions Comparison

The results of the boundary treatments for the jet problem are introduced in this section. Different boundary conditions such as characteristic boundary conditions, buffer domain method and perfectly matching layer technique are compared with a reference solution obtained from long domain simulation. The computational domain for the reference solution is chosen very long in the axial direction in order to ensure that no waves are reflected from the boundaries. The results for the long domain are compared with other boundary conditions only in the computational domain of interest, which is one half the long domain.

A subsonic cold jet with M_j =0.85 and Reynolds number 2500 is considered for the comparisons. The mean flow parameters are presented in table (6.1) and the jet mean flow solution is calculated using the boundary layer equations as discussed in chapter 3. The linear stability analysis for this jet indicates that the fundamental frequency is 0.944, which means that the Strouhal number is 0.3. Inflow disturbances are introduced at the jet

inflow boundary with the fundamental frequency ω and the first subharmonic $\omega/2$. The shape of the disturbances is obtained from the linear stability analysis and the amplitude is assumed 0.001.

Table (6.1) Jet mean flow parameters

$M_j = \frac{U_j}{\sqrt{\gamma R T_j}}$	$\mathrm{Re} = \frac{U_j \rho_j r_j}{\mu_j}$	$\frac{U_\infty}{U_j}$	$\frac{T_\infty}{T_j}$	Pr	β
0.85	2500	0	0.5	0.72	5

The computational domain of interest is extended to 50 radius in the axial direction and 15 radius in the radial direction with grid dimensions 500×200 points. A uniform grid is used in the axial direction and the grid is clustered in the radial direction at $r=1$ with clustering parameter 4.5. Table (6.2) presents the dimensions of the computational domains and the grid sizes that are used for the different boundary treatments. For the perfectly matching layer technique, a layer of 7 radius length and of 70 grid points is attached close to the outflow boundary at the downstream location. Another layer with the same thickness is added at the radiation boundary and 30 grid points are used for this layer and the maximum value of the absorption coefficients (σ_{mx} and σ_{my}) are assumed 2. While, a buffer domain with 12 radius thickness and 120 points is used only in the axial direction.

Table (6.2) Grid dimensions for different boundary conditions

	Computational domain (x,r)	Grid size
Long domain	100×15	1000×200
Characteristic B.CS	50×15	500×200
Buffer domain	62×15	620×200
Matching layer	57×15	570×200

The time signal of the pressure disturbances at different positions in the computational domain is presented in Fig. (6.7) for different boundary conditions. The results indicate that maximum wave reflections are caused by the characteristic boundary conditions. As a result of the characteristic boundary treatment, the phase and amplitude of the pressure disturbances are completely different from those of the long domain simulation. The buffer domain technique caused some changes of the predicted disturbance amplitude but the results are still better than those predicted by the characteristic boundary conditions. Maximum wave reflections are obtained at the jet centerline for both boundary conditions and the reflections decrease near the inflow boundary.

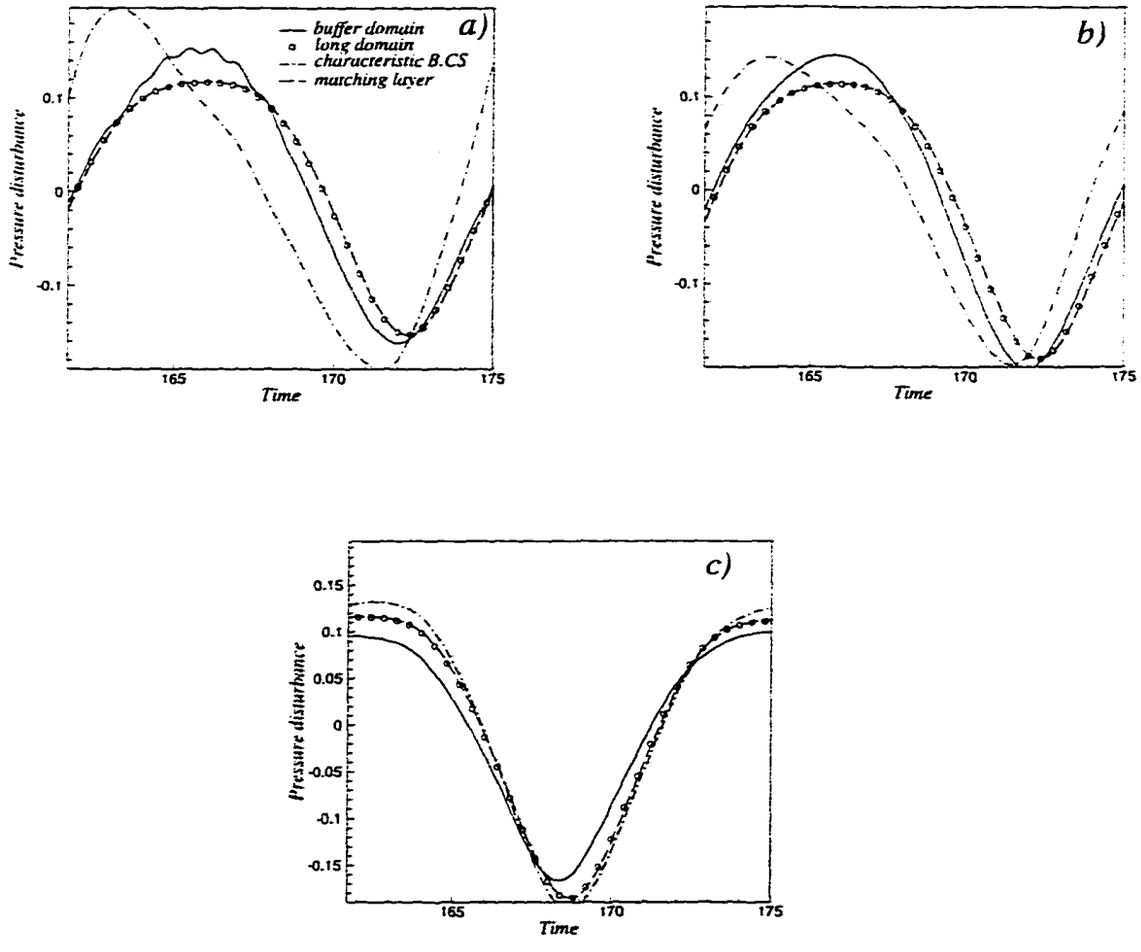

Figure (6.7) Time history of the pressure disturbance for one periodic cycle a) $x=50, r=0$ b) $x=50, r=1$ c) $x=48, r=1$

Minimum reflections are caused by the matching layer technique at the outflow boundaries. The results obtained by the perfectly matching layer are in excellent agreement with the reference solution for the whole computational domain except near the inflow boundary where some reflections are caused as shown in Fig. (6.8) for the time history of the total axial velocity.

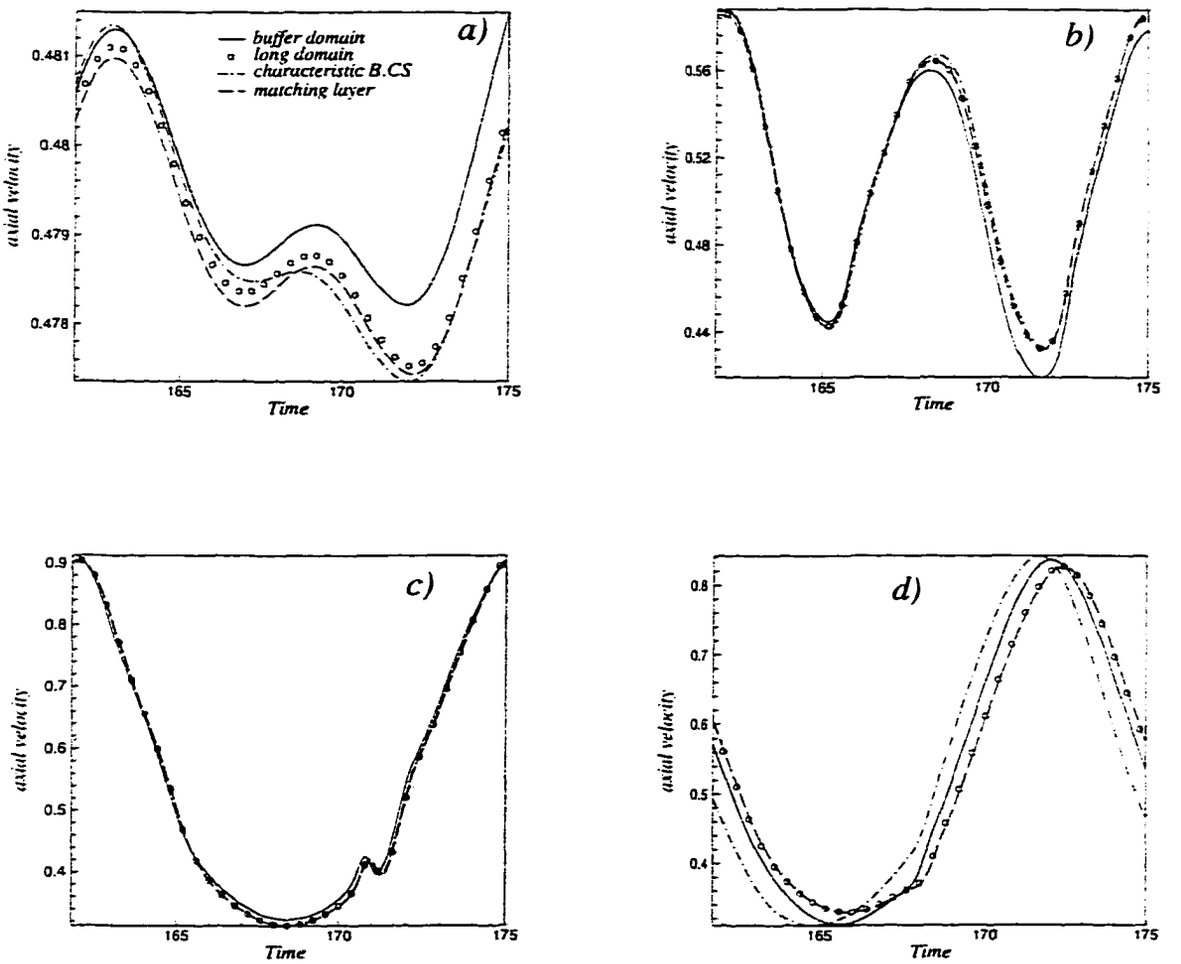

Figure (6.8) Time history of the axial velocity for one periodic cycle at r=1
a) *x=0* b) *x=10* c) *x=30* d) *x=50*

Although, the reflections caused by the characteristic boundary conditions and the buffer domain decrease as the waves travel upstream, both boundary conditions give higher reflections than the matching layer at the inflow and outflow boundaries. The variation of the pressure disturbance amplitude with the axial distance for the first

subharmonic ($\omega/2$) is introduced in Fig. (6.9). It is clear from the graph that minimum reflections are caused by the matching layer technique while the characteristic boundary conditions render the solution completely different from the reference solution. Thus, the matching layer technique is the kind of boundary treatment that one might rely on for the jet noise simulations since it is not as computationally expensive as the buffer domain technique and it is nearly perfect for the outflow boundary treatments.

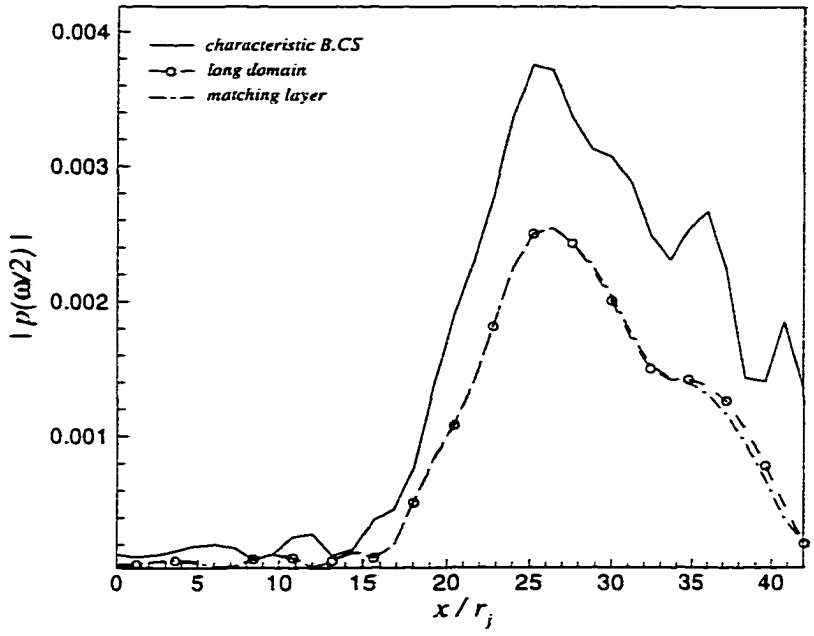

Figure (6.9) Amplitude of the pressure disturbance at r=7.5versus axial distance

Decreasing the length of the perfectly matching layer causes some reflections at the outflow boundary. In order to determine the length of the matching layer required for minimum wave reflections, a comparison between two matching layer results with different lengths is shown in Fig. (6.10). Two jet simulations are done to calculate the variation of the pressure disturbance amplitude with the axial distance. The first simulation is done with a layer of 15 radius length in the axial direction and the second simulation is computed for a layer of 4 radius length. The same absorption coefficients are used for both layers. The results indicate that some reflections are caused by the shorter layer specially near the outflow boundary. However, the wave reflections are still

very small and the amount of wave reflection does not exceed four percent of the pressure disturbance amplitude.

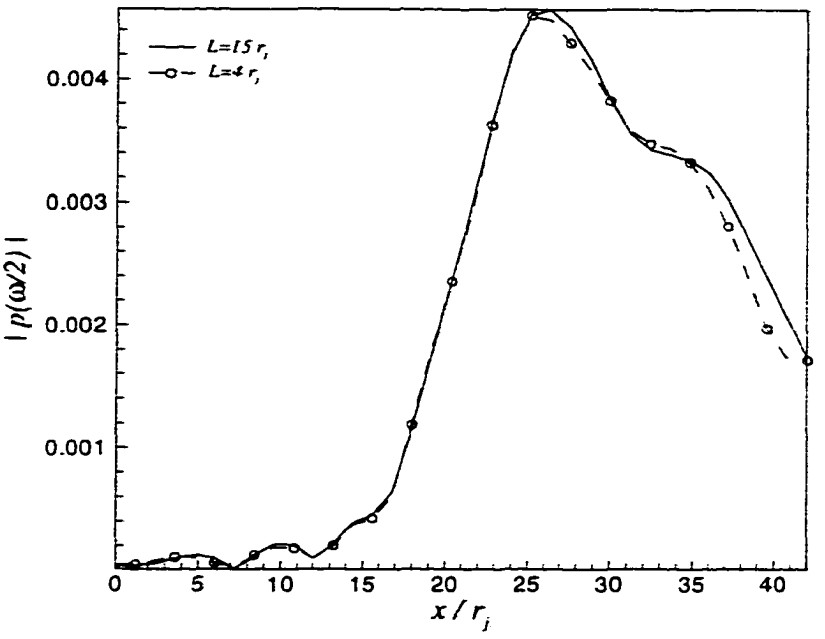

Figure (6.10) Amplitude of the pressure disturbance at r=6 versus axial distance for two matching layer.

6.3 Subsonic Jet simulations

Direct numerical simulation of subsonic jets for various Mach numbers is presented in this section with emphasis on the near field results and analyzing the acoustic field data using the Fourier transform. Three different cases are computed at low and high Reynolds numbers. The sound generated by vortex roll-up and pairings is investigated for the subsonic jets by forcing the inflow disturbance at the fundamental frequency and its first two subharmonics.

Case 1:

The first simulation is done for Mach number 0.6 and Reynolds number 2500. The mean flow parameters for this jet are presented in table (6.3). An initial axial velocity profile with momentum thickness 0.08334 (β =6) is used to obtain the jet mean flow.

Table (6.3) Jet mean flow parameters for case 1

$M_j = \frac{U_j}{\sqrt{\gamma R T_j}}$	$\mathrm{Re} = \frac{U_j \rho_j r_j}{\mu_j}$	$\frac{U_\infty}{U_j}$	$\frac{T_\infty}{T_j}$	Pr	β
0.6	2500	0	1	1	6

The fundamental frequency, which is obtained from the linear stability analysis as discussed in chapter 4, is 1.25 (St=0.398) and the first two subharmonics are 0.625 and 0.3125. The wave periods for these frequencies are 5.027, 10.05 and 20.1 respectively. The amplitude of the inflow disturbance is assumed 0.0015 and the eigenfunctions of the inflow disturbances are normalized with respect to the maximum amplitude of the axial velocity disturbance. The linear stability results for this jet are introduced in chapter 4.

Table (6.4) Grid parameters for case 1

Parameter	Value
X_{max}/r_j (including matching layer)	55
R_{max}/r_j (including matching layer)	25
Maching layer in x-direction (L_{bx})	5
Maching layer in r-direction (L_{br})	7
Number of points in x-direction (*IMAX*)	1225
Number of points in r-direction (*JMAX*)	161
Number of points in axial matching layer	111
Number of points in radial matching layer	14
$\Delta x/r_j$	0.0449
$(\Delta r/r_j)_{\min}$ at $r=1$	0.0398
$(\Delta r/r_j)_{\max}$ at $r=r_{max}$	0.594

The computational domain dimensions and the grid parameters are summarized in table (6.4). Giles inflow boundary conditions are used at the inflow boundary and the matching layer technique is employed at the outflow boundaries with maximum

absorption coefficient equals two. Axisymmetric jet is considered for the simulation and symmetrical boundary conditions are applied at the jet centerline.

A total time of 40 periods of the fundamental frequency is computed until the entire domain is settled into its nearly periodic steady state and the data are stored in the last four cycles for analysis using the discrete Fourier transform. Time history of the total axial velocity and pressure are presented in Figs. (6.11) and (6.12).

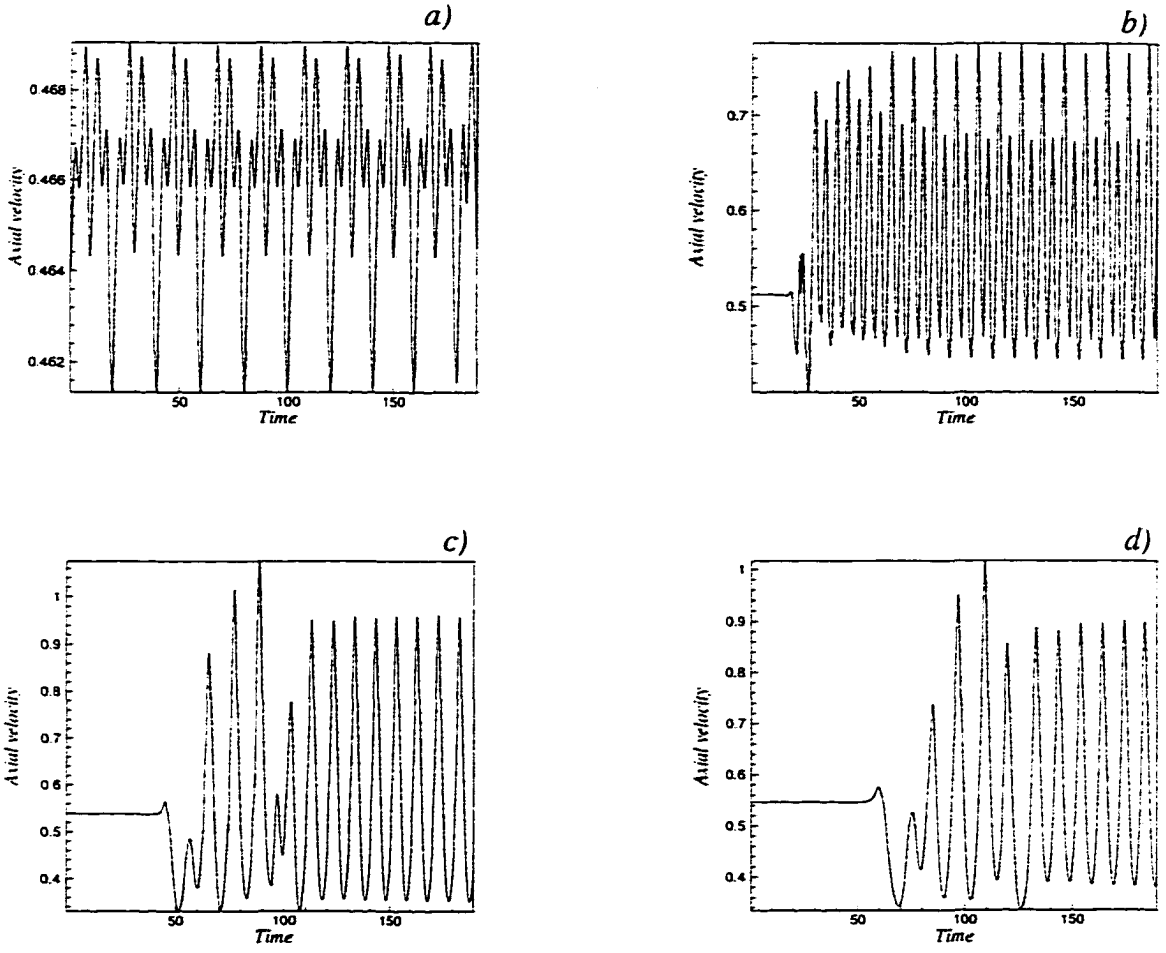

Figure (6.11) Time history of total axial velocity for $M_j=0.6$ at $r=1$ and a) $x=0$, b) $x=13$, c) $x=36$, d) $x=50$

The streamwise velocity is plotted at different axial positions downstream of the inflow boundary. At the first position, x=0, the disturbance is felt instantly and all the components of the inflow disturbance are felt equally. The start up transient is seen to

arrive at different downstream points at progressively later times. As the disturbance moves downstream, the first subharmonic is dominant and the amplitude of the disturbance grows with the axial distance until it saturates.

It is evident from Fig. (6.12) that the flow becomes nearly periodic at time equals 180, which corresponds to 36 cycles of the fundamental frequency. In the near field (r=0 and r=1), the pressure disturbances are dominated by the frequency of the vortex pairings which is the frequency of the first subharmonic and in the acoustic field (r=17) the amplitude of the first subharmonic is large compared with second subharmonic.

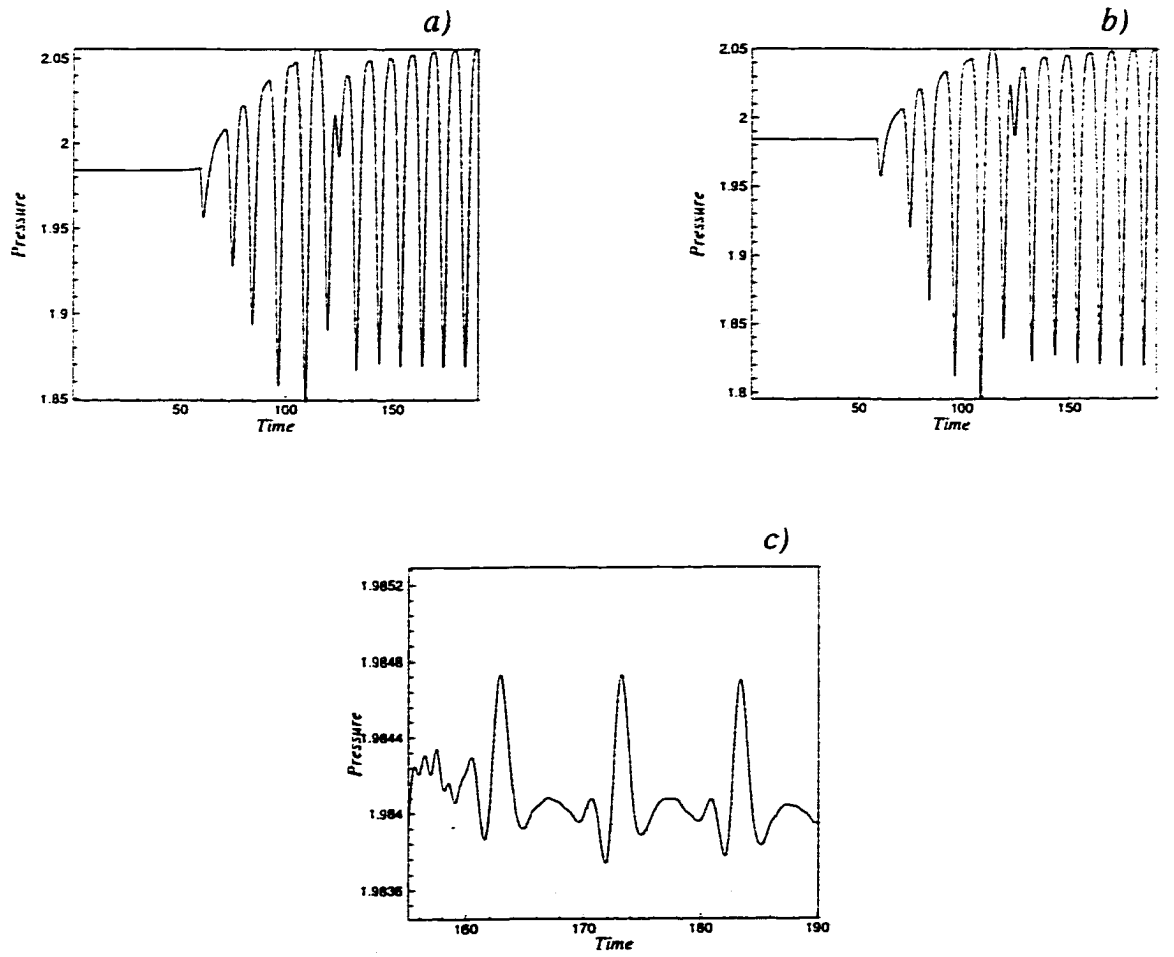

Figure (6.12) Time history of the total pressure at x=50 and a) *r=0,* b) *r=1,* c) *r=17*

As a result of the inflow disturbance, the shear layer rolls-up and discrete vortices are developed in the mixing layer and these discrete vortices pair further downstream. The evolution of the near field vorticity with time at subsequent equally spaced time intervals of one periodic cycle of the second subharmonic ($T=8\pi/f$) is presented in Fig. (6.13). The vortex pairing process appears downstream the vortex roll-up and two subsequent pairings at different axial positions are obeserved. Multiple pairing processes is also reported for thin shear layers by Mitchel et al (1999). The pairing process is complete at downstream distance (x=24) where the amplitude of the axial velocity disturbance at f/2 reaches a maximum value as shown in Fig. (6.14). A third vortex pairing may be caught if the computational domain is extended very long in the streamwise direction. After the pairing process is complete, the vortices convect downstream with viscosity acting to reduce the peak levels of vorticity in vortex cores.

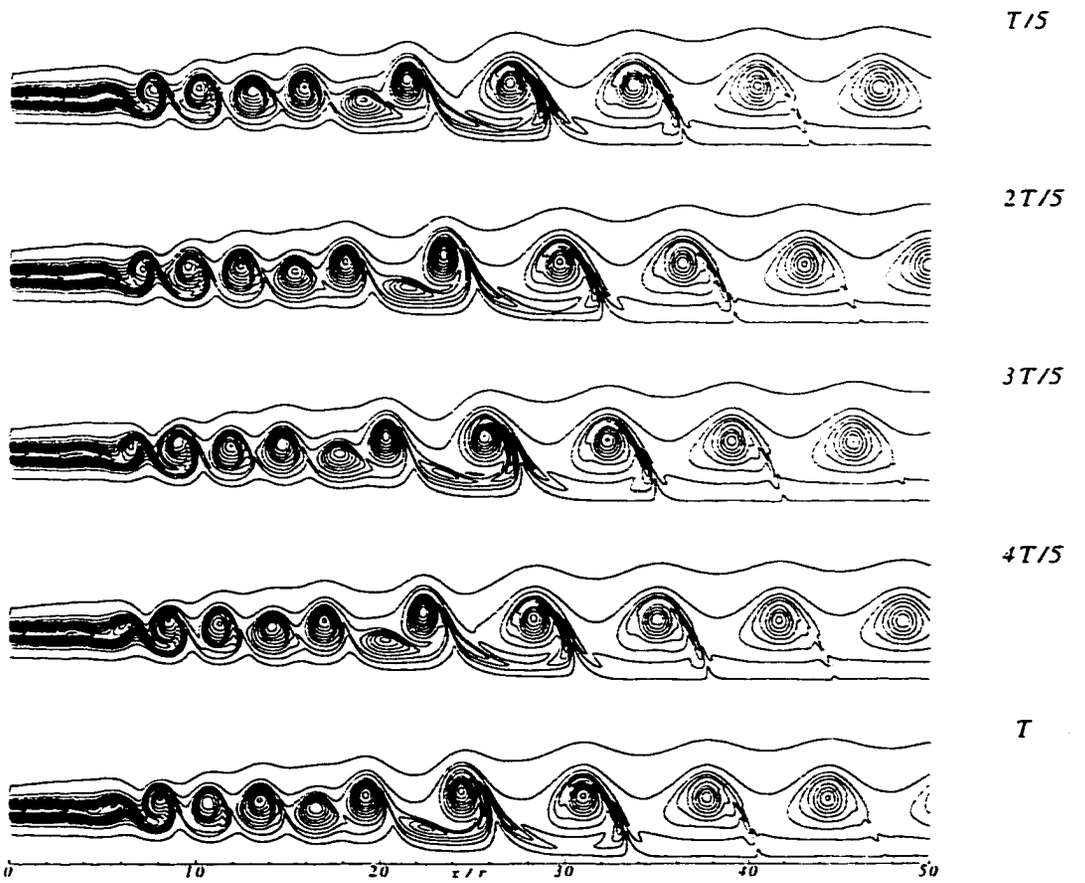

Figure (6.13) Evolution of vorticity with time at various equally spaced intervals (M_j=0.6). The contour levels ranges from 0 to 2.83 U_j/R_j with increment 0.236 U_j/R_j and 12 contour levels for each plot.

Using the discrete Fourier transform of the data stored during the last four cycles, the amplitude of the disturbances at different frequencies is estimated from Eq. (6.2) and the average amplitude of the axial velocity disturbance is calculated at different downstream positions using Eq. (6.3)

$$u(m\omega)=\frac{1}{k_{max}}\sum_{i=1}^{k_{max}}u(i)\,e^{-2\pi j(i-1)(m-1)/k_{max}} \tag{6.2}$$

$$u'(\omega)=\left(\frac{1}{U_j^2 r_j^2}\int_{r=0}^{r_{max}}2\pi r u^2 dr\right)^{\frac{1}{2}} \tag{6.3}$$

where $j=\sqrt{-1}$, k_{max} is the total number of samples per period of the second subharmonic and $u(i)$ is the disturbance at sample i.

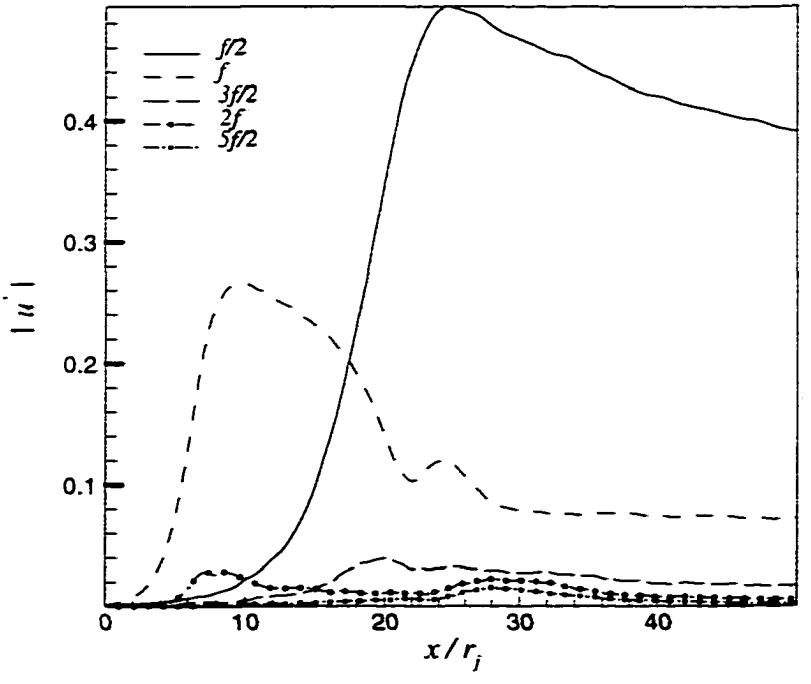

Figure (6.14) Amplitude of axial velocity disturbance versus downstream position at various frequencies (M_j=0.6)

The growth of the axial velocity disturbances at various frequencies, which corresponds to the vortex roll-up and pairing is shown in Fig. (6.14). One concludes from the figure that the maximum amplitude of the disturbance occurs at frequency f/2 which is the frequency of the first subharmonic. The amplitude of the first subharmonic grows until it peaks at downstream location where the vortex pairing process is complete. The correspondence of the saturation position and the completion of the vortex pairing process is also observed by Ho and Huang (1982) and Mitchel, Lele and Moin (1999). Additionally, the amplitude of the disturbances at the fundamental frequency saturates in the region of the vortex roll-up and it grows again until it saturates at the end of the vortex pairing process. The multiple saturation is observed by Colonius et al (1995). Other frequencies are plotted but they have small amplitudes with respect to the fundamental frequency and the first subharmonic.The amplitude of disturbances at even frequencies of the second subharmonic, which is defined as ($n\ f\ /4$), is very large compared with the odd frequencies which means that the sound source is characterized by even frequencies. The dominant source frequencies and their saturation positions are summarized in table (6.5).

Table (6.5) Source frequencies and saturation positions for (M_j=0.6)

Frequency	Position of max. amplitude	Amplitude
f/4	21.5	0.00866
f/2	24.7	0.49396
3f/4	20	0.01694
f	10	0.26527
6f/4	20	0.03957
2f	9	0.02878
10f/4	28	0.01554
3f	9	0.01371

The momentum thickness of the jet shear layer, which is defined by Eq. (6.4), is computed using the Fourier transform of axial velocity and the results are presented in

Fig. (6.15). Comparing the variation of the momentum thickness at no inflow disturbance with that of the disturbed flow, one notes that the vortex roll-up has no effect on the momentum thickness. In addition, the momentum thickness seems to have a step-like increase at x=5 which is the position of the first pairing process and then the momentum thickness saturate at the end of the first pairing process. This result of the step-like increase in the momentum thickness is noted experimentally by Laufer and Zhang (1983). Another step-like increase appears at approximately x=18 which is the beginning of the second vortex pairing and the increase is complete at x=24 which is end of the second pairings. The growth of the momentum thickness starts to decrease as a result of the viscosity acts inside the vortices.

$$\delta_2(x) = \int_{r=0}^{r\max} \frac{u(x,r)}{U_j}\left(1-\frac{u(x,r)}{U_j}\right) dr \tag{6.4}$$

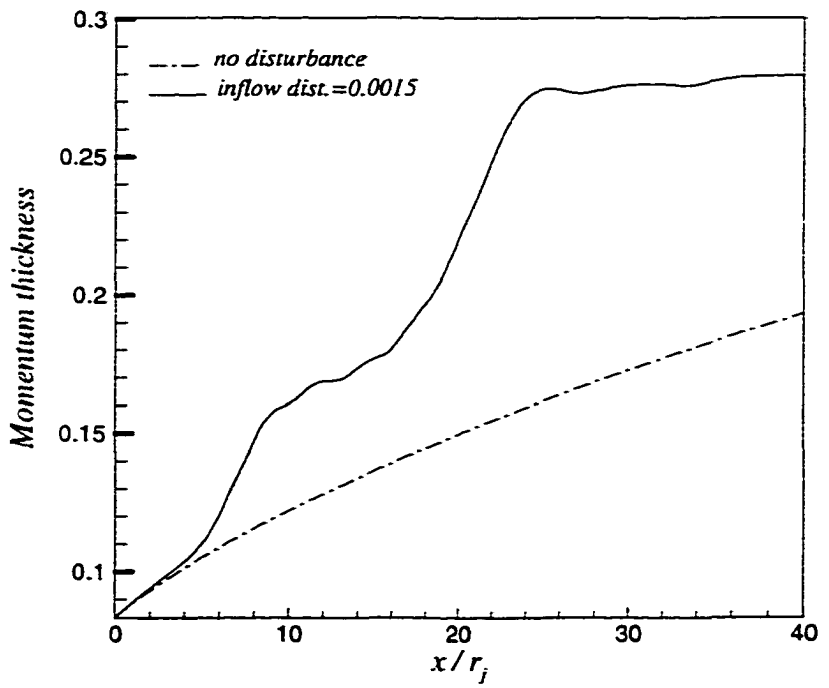

Figure (6.15) Variation of jet momentum thickness with the downstream position (M_j=0.6)

The variation of the pressure disturbance amplitudes at different frequencies with the radial direction is shown in Fig. (6.16). The pressure disturbances reaches its maximum value near the shear layer (r=1). This result is also predicted by the linear stability theory as presented in chapter 4. The largest amplitude is obtained for the first subharmonic and higher frequencies have small amplitude in the near field.

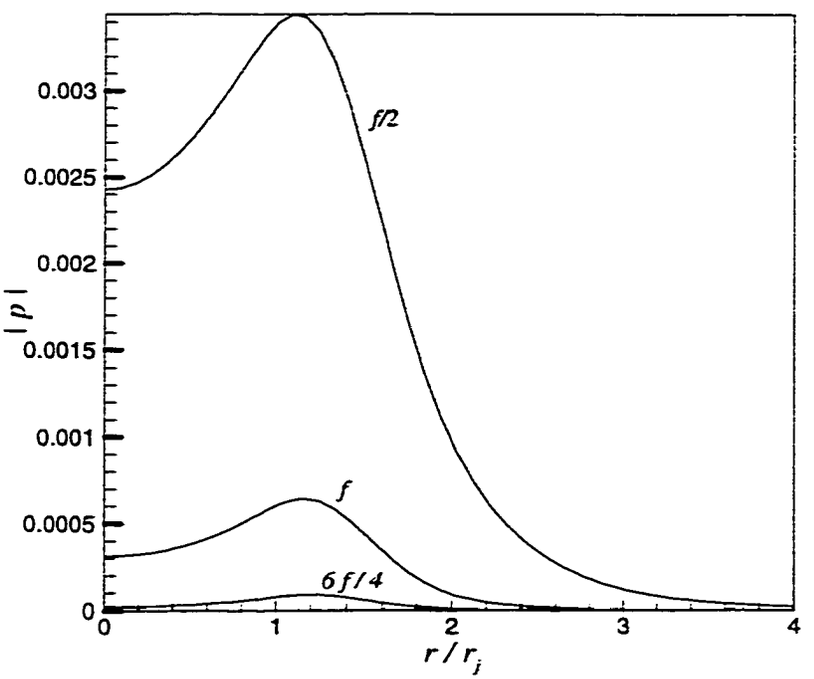

Figure (6.16) Amplitude of the pressure disturbance at different frequencies versus radial distance at x=36 (M_j=0.6)

Contours for the Fourier components of the pressure disturbances at the fundamental frequency and the first subharmonic are plotted away from the shear layer as shown in Fig. (6.17). It is noted that the pressure waves at the fundamental frequency emanate from the region of the layer where the amplitude of the disturbances saturates (x=10) and the pressure waves at the first subharmonic are radiated from downstream distance where the second vortex pairings are complete. The pressure disturbances are radiated to the far field with the same frequency of the near field.

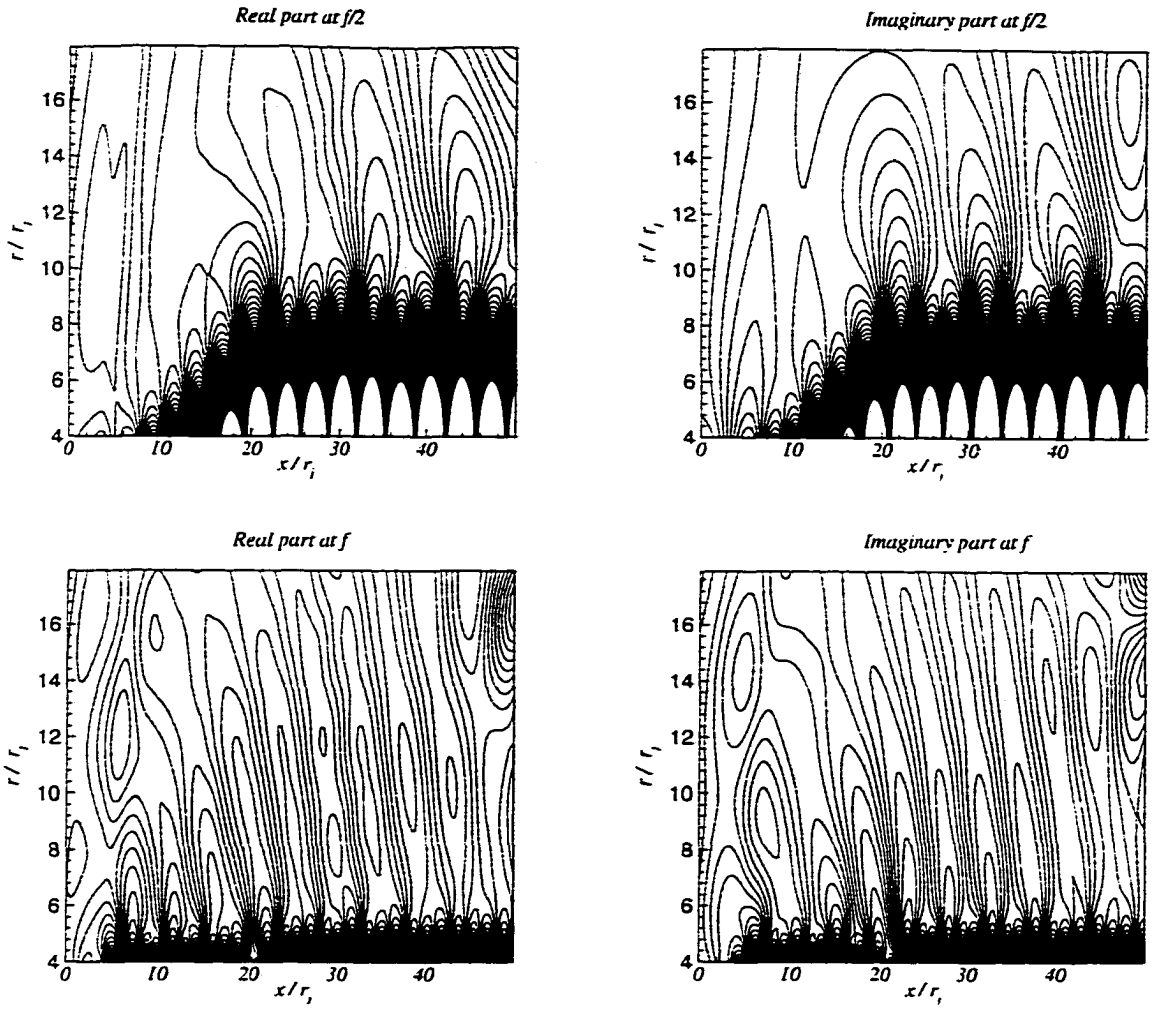

Figure (6.17) Pressure contours in the acoustic field at different frequencies (M_j=0.6) Maximum and minimum contour values are $\pm 5.812\times10^{-4}$ and 120 contour levels are used in the graphs.

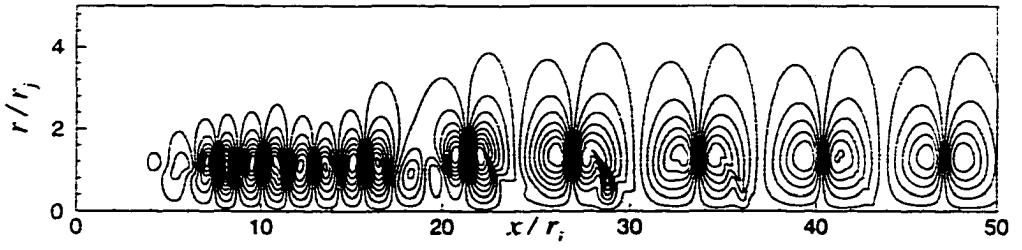

Figure (6.18) Contours of instantaneous total normal velocity in the near field (M_j=0.6). The maximum contour value is 0.27 and the minimum value is –0.214 and 16 levels are used in the graph.

Case 2:

In order to investigate the effect of increasing the Mach number on the sound radiated from subsonic jets, another case is computed at higher Mach number (M_j= *0.8*) and Reynolds number 2500 The same initial axial velocity profile with momentum thickness 0.08334 (β =6) is also used for this simulation to obtain the jet mean flow. The fundamental frequency obtained using the linear stability theory is 1.3195 (St=0.42) and the first two subharmonics are 0.66 and 0.33. The amplitude of the inflow disturbance is assumed 0.0015 and the eigenfunctions of the inflow disturbances are normalized with respect to the maximum amplitude of the axial velocity disturbance.

The computational domain for this case is extended to a longer distance in the radial direction in order to compute part of the acoustic field for the sake of comparison with the computations of the linearized wave equation in the far field. The dimensions of the domain and the grid parameters are summarized in table (6.6).

Table (6.6) Grid parameters for case 2 (M_j=0.8)

Parameter	Value
X_{max}/r_j (including matching layer)	55
R_{max}/r_j (including matching layer)	70
Maching layer in x-direction (L_{bx})	5
Maching layer in r-direction (L_{br})	8
Number of points in x-direction (*IMAX*)	1225
Number of points in r-direction (*JMAX*)	451
Number of points in axial matching layer	111
Number of points in radial matching layer	14
$\Delta x/r_j$	0.0449
$(\Delta r/r_j)_{min}$ at $r=1$	0.03
$(\Delta r/r_j)_{max}$ at $r=r_{max}$	0.611

The computations are run until the entire domain is settled into its nearly periodic steady state. Time history of the axial velocity at different downstream positions indicates

that the flow becomes periodic at the outflow boundary after approximately 40 cycles of the fundamental frequency. The last 12 cycles of the computations are presented in Fig. (6.19). The axial velocity disturbances near the inflow boundary are dominated by all the excitation frequencies as shown in Fig. (6.19a) while the flow near the outflow boundary is dominated by the frequency of the first subharmonic which is the frequency of the vortex pairing process.

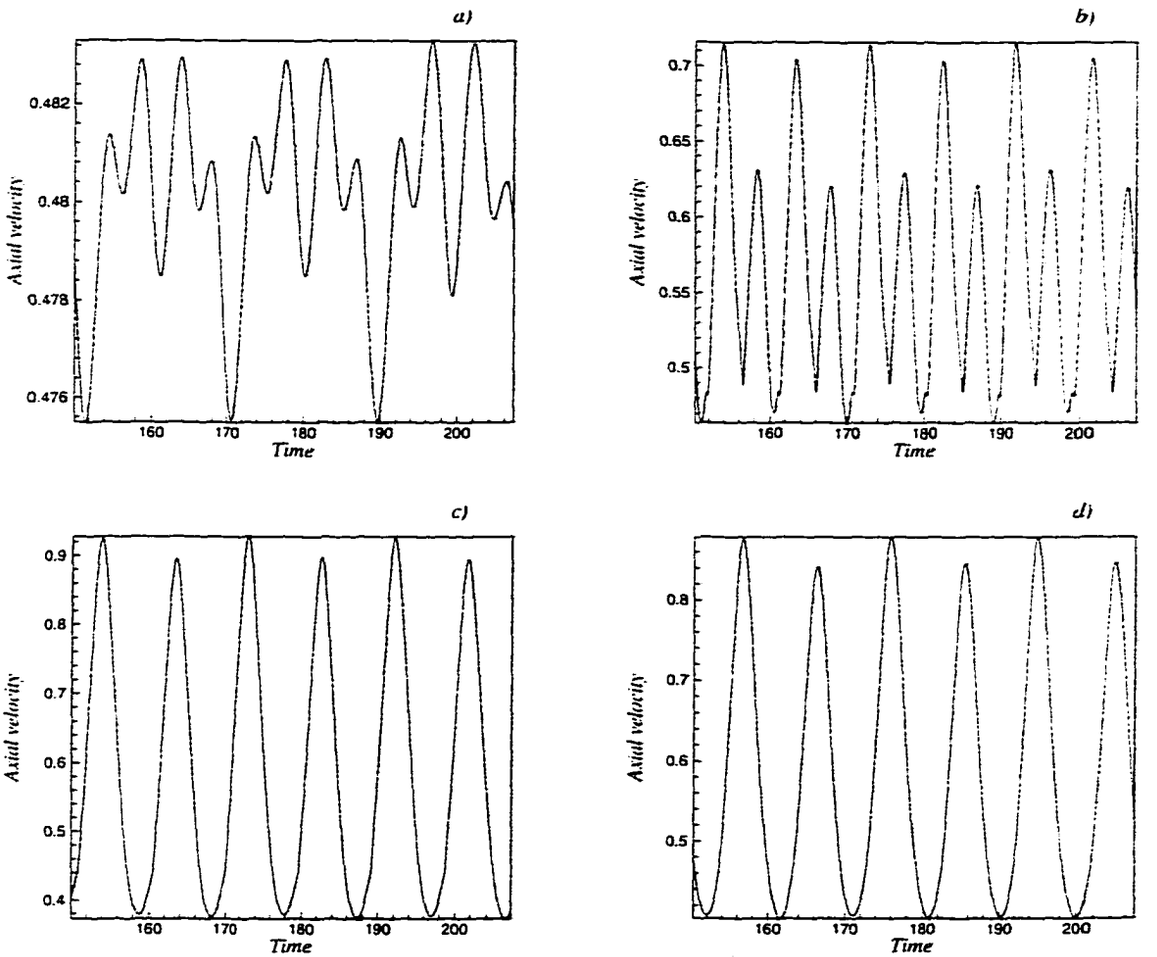

Figure (6.19) Time history of total axial velocity for $M_j=0.8$ at $r=1$ and a) $x=0$, b) $x=13$, c) $x=36$, d) $x=50$

The near field vorticity contours are plotted in Fig. (6.20) at five equally spaced instants within a periodic cycle of the second subharmonic of period (T). The jet shear layer roll-up is clear near the inflow and the vortex pairing is captured at two different

downstream positions. As the flow moves downstream, the vorticity is reduced due to the effect of the viscosity.

The amplitude of the axial velocity disturbance at different frequencies is computed using the Fourier transform of the time signal of the last cycle of the second subharmonic and the results are shown in Fig. (6.21). As predicted by the linear stability theory, the amplitude of the disturbances of different frequencies is reduced as a result of increasing the jet Mach number.

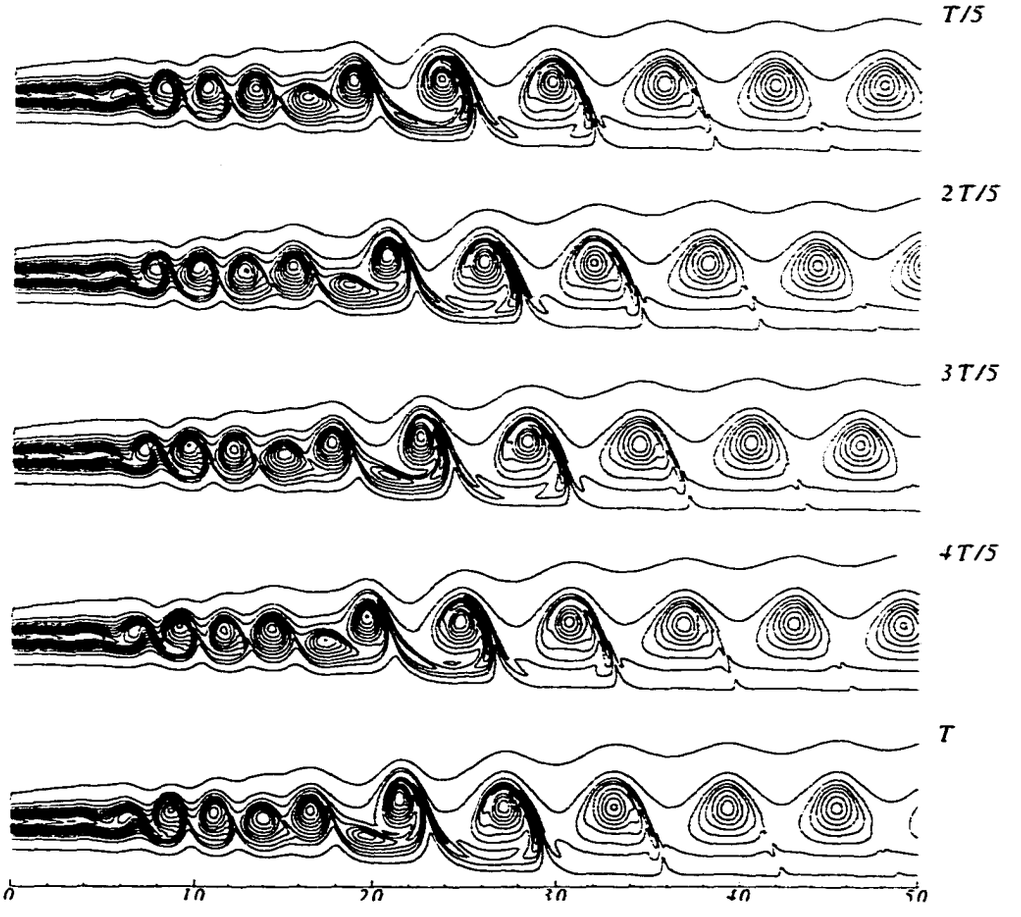

Figure (6.20) Evolution of vorticity with time at different equally spaced intervals (M_j=0.8). The contour levels range from 0 to 2.84 U_j/R_j with increment 0.236 U_j/R_j and 12 contour levels for each plot.

The maximum amplitude of the disturbance for the first subharmonic is 0.406 while it is 0.494 for Mach number 0.6. The first subharmonic (f/2) peaks at downstream position (x=22) where the vortex pairing process is complete. The amplitude of the fundamental frequency grows and peaks at x=11 and then decays until it grows again at x=19. The amplitude of the second subharmonic grows slowly and no saturation is observed for this frequency which means that a third pairing process may be obtained further downstream.

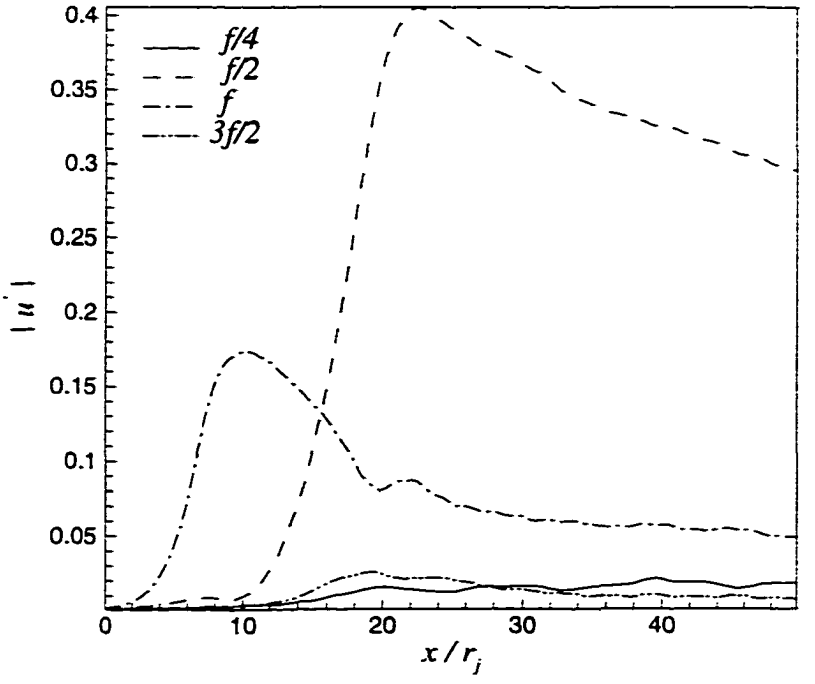

Figure (6.21) Amplitude of axial velocity disturbance versus downstream position at various frequencies (M_j=0.8)

The amplitude of the disturbance at higher frequencies is similar to, but generally smaller than, that of the fundamental frequency and the disturbance amplitude decreases for higher modes. A list of the saturation positions of the different frequencies and their amplitudes is presented in table (6.7). As noticed for the lower Mach number jet, only even frequencies of the second subharmonic have considerable amplitudes. The fundamental frequency (f) and its multiple frequencies ($n f$), where n is integer, saturate at the same axial position where the first pairing process is complete while multiple

frequencies of the first subharmonic (n $f/2$) reach their peak amplitude at the same location of the second vortex pairing.

The growth of the momentum thickness is plotted for both laminar and disturbed jet flows as shown in Fig. (6.22). In the region of vortex roll-up, the momentum thickness has nearly the same value as for the laminar jet.

Table (6.7) Source frequencies and saturation positions for (M_j=0.8)

Frequency	Saturation position	Maximum amplitude
f/2	22.5	0.406
f	12.5	0.245
3f/2	22.5	0.0405
2f	10	0.0269
5f/2	22.5	0.012
3f	10.5	0.0164

Following the region of the vortex roll-up, two steps-like increase in the momentum thickness are observed at various axial positions, which correspond to two different vortex-pairing processes. The first step like increase in the momentum thickness starts at x=6 and ends at x=11 which is the position of saturation for the fundamental frequency and another step increase resumes after the completion of the first pairing. The second vortex pairing is complete where the first subharmonic reaches its maximum value which means that this region is dominated by the frequency of the first subharmonic. As a result of the viscosity effect on the vorticity levels, the growth rate of the momentum thickness decreases after the completion of the second vortex pairing process.

The far field pressure disturbance contours are shown in Fig. (6.23) with an arrow indicating the position of the vortex pairing process. The domain shown in the graph is

limited between 5 and 50 radius in the radial direction. It is evident that the pressure waves propagate to the far field in semi-circles and these waves emanate from the region of the vortex pairing where the instability waves saturate. This is similar to the observations of Laufer and Yen (1983), Bridges and Hussain (1992) and to the analysis of Mankabadi and Liu (1984), Crighton and Huerre (1990), Mankbadi (1990) and Colonius, Lele and Moin (1997).

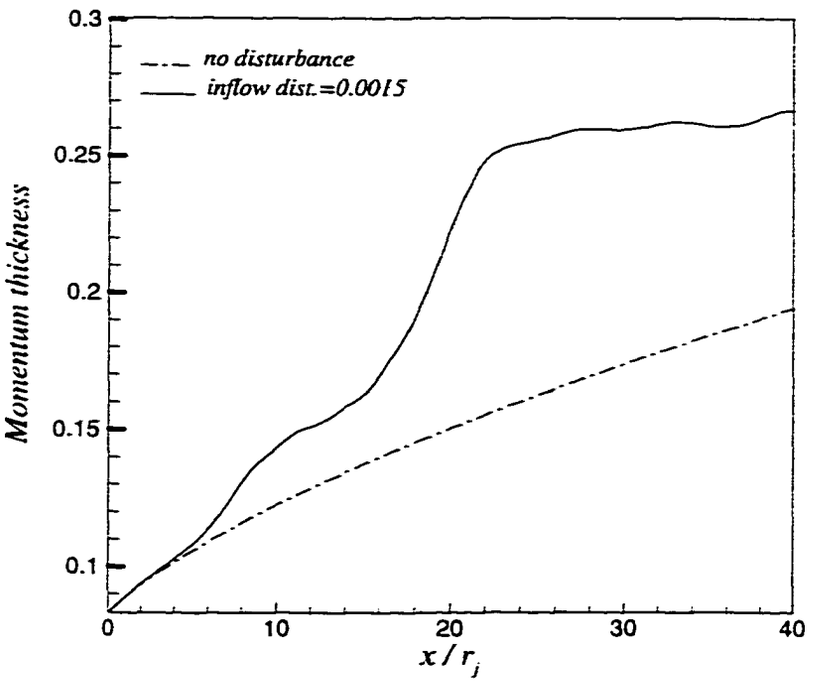

Figure (6.22) Variation of jet momentum thickness with downstream position (M_j=0.8)

The dilatation (6) defined by Eq. (6.5) is chosen to best display the acoustic waves in the far field and to provide an information about the direcivity pattern. The pressure disturbances in the far field show similar pattern but it is slightly contaminated by the far field boundary conditions. The pressure distortion in the far filed due to the boundary treatment is not a serious problem and does not affect the outcome of the computations as reported by Colonius, Lele and Moin (1997).

$$6 = \nabla . u \tag{6.5}$$

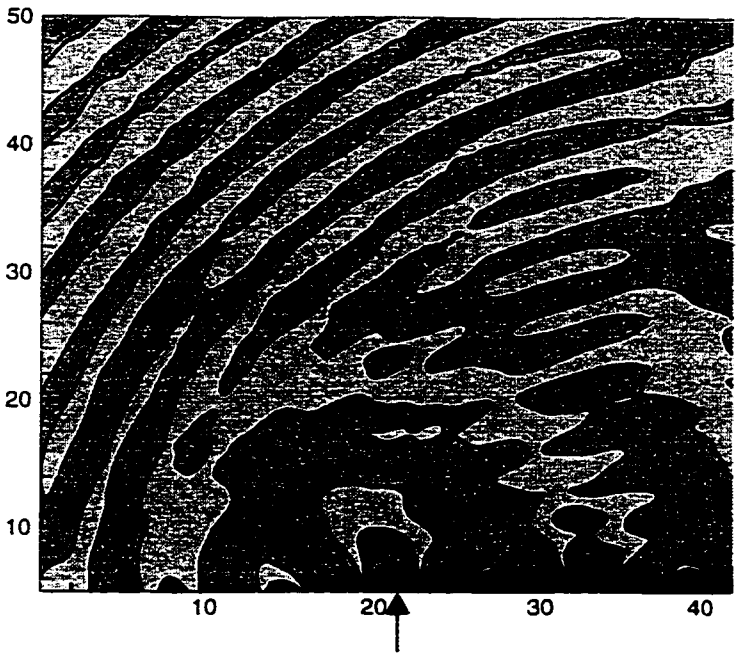

Figure (6.23) Far field pressure disturbance contours for M_j=0.8 with maximum and minimum pressure levels $\pm 1.5\times10^{-3}$ and 15 levels

The dilatation is proportional to the time derivative of the pressure disturbance for zero mean velocity in the far field. Thus, the dilatation is more nearly periodic in time than the pressure disturbance and the discrete Fourier transform can be computed more accurately. In Fig. (6.24), the dilatation is plotted away from the mixing layer in a region limited by r=20 and r=60. The graph shows that the acoustic waves is radiated from a region where the first subharmonic saturates which proves that the vortex pairing process of the subsonic jets is responsible for radiating sound to the far field.

The total radial velocity contours in the near field is presented in Fig. (6.25). The contours are presented in the region ($0 < r < 5$) with 16 contour levels. The maximum value of the levels is 0.236 and the minimum is –0.23. High values of the total radial velocity are experienced where the vortices are located and these regions of high radial velocity are equally spaced near the outflow. These space are of the order of the vortex size and it is smaller near the inflow boundary than near the outflow boundary which indicates that vortices at different frequencies exist in these regions.

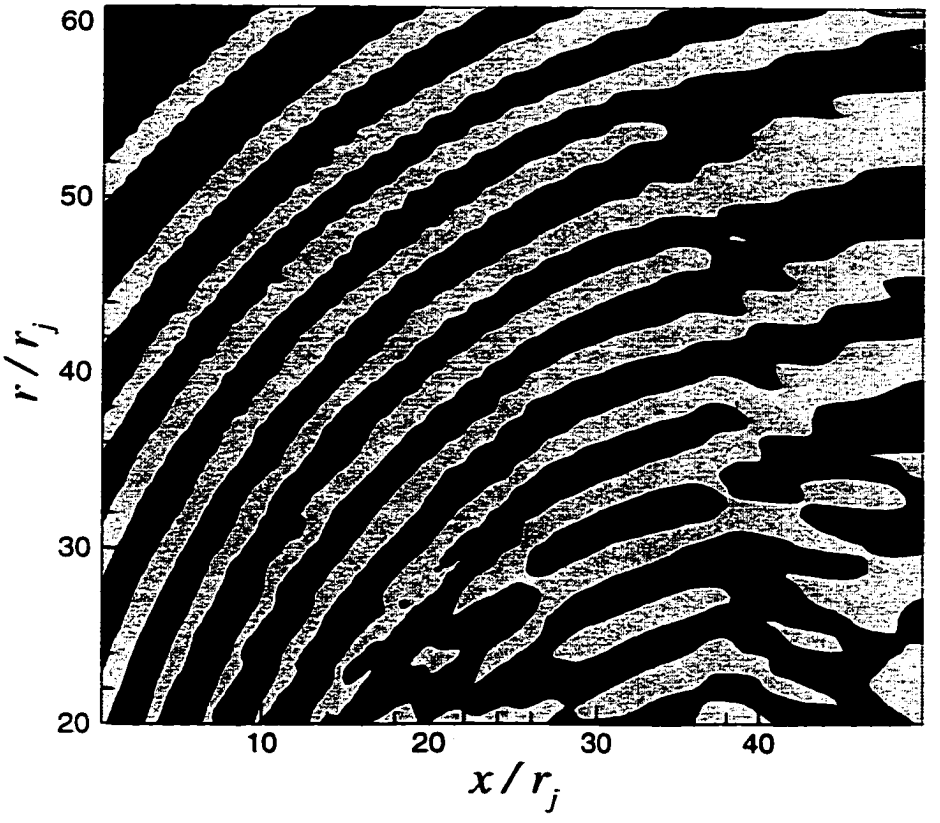

Figure (6.24) Far field dilatation contours for M_j=0.8 with maximum and minimum dilatation levels $\pm 2.5\times10^3$ and 19 levels.

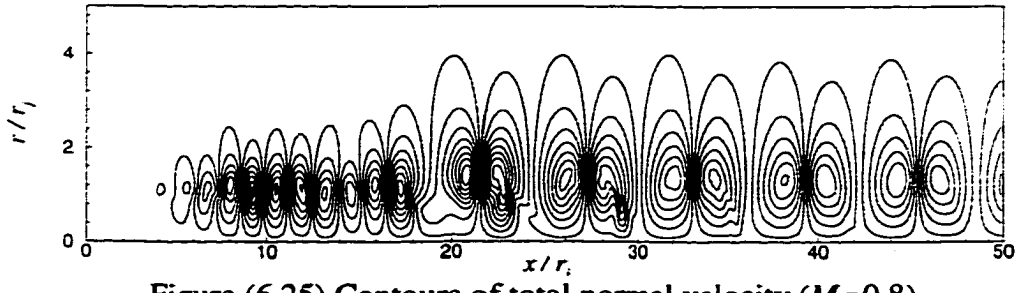

Figure (6.25) Contours of total normal velocity (M_j=0.8).

Case 3:

A third case is computed at higher Reynolds number (Re=10^5) and Mach number 0.85. The initial axial velocity profile used for the laminar flow computations has a momentum thickness 0.1 (β=5) and the temperature ratio of the jet is assumed to be one.

The Prandtl number is chosen to be 0.72 for this simulation. Linear stability analysis for this jet indicates that the most unstable frequency is 1.231 (St=0.392) and hence the wave period of the fundamental frequency is 5.1. The inflow boundary for this case is also excited at the most unstable frequency and its first two subharmonics with an initial amplitude 0.014.

The computational domain is extended to 60 radius in the axial direction and 14 radius in the radial direction. The last 10 radius in the axial direction are used for the matching layer. The mesh size is 1336×151 and uniform grid is used in the axial direction while the grid is stretched in the radial direction with minimum grid spacing 0.0.29 at the shear layer. Since, this simulation is done for very high Reynolds number, the numerical errors due to the high frequency oscillations grows without limit and causes the numerical scheme to be unstable. Therefor, a sixth order numerical filter is used to eliminate the high frequency oscillations without affecting the amplitude of the lower frequencies. The filter is applied every few iterations.

The computations are continued until the flow becomes nearly periodic at the outflow boundary after 45 cycles of the fundamental frequency and the data of the last four cycles are analyzed using the discrete Fourier transform. The time history of the axial velocity at different axial locations and near the critical layer is shown in Fig. (6.26). The graph indicates that the flow becomes nearly steady and periodic at both the inflow and outflow boundaries. At the inflow boundary (x=0), the evolution of the disturbances is due to all the frequencies and the disturbances grow linearly while the jet flow is dominated by the fundamental frequency at x=7. As the flow moves further downstream, the first subharmonic is the dominant frequency and the growth of the disturbances is due to the effect of the first subharmonic which is the same result obtained for low Reynolds number. It is also clear that the amplitude of the axial velocity disturbance increases significantly with the axial distance until it saturates and then decays slowly near the outflow boundary.

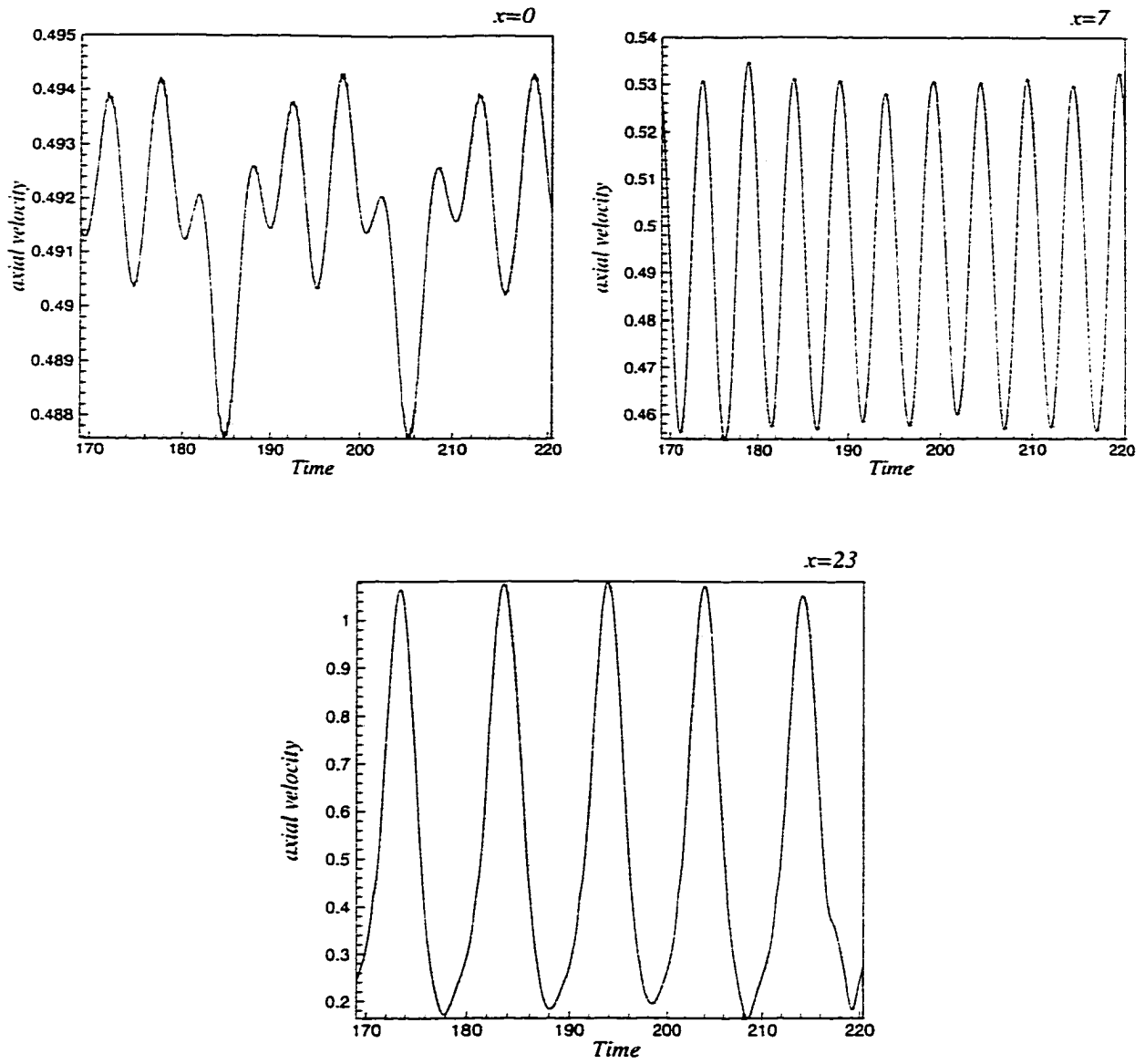

Figure (6.26) Time history of total axial velocity for M_j=0.85 at r=1 and different axial distances.

The axial velocity disturbance amplitudes at different frequencies are presented in Fig. (6.27). As the Reynolds number is increased, the amplitude of the disturbance for both the fundamental frequency and the first subharmonic is increased which means that the noise radiated from subsonic jets with higher Reynolds numbers is greater than that of low Reynolds number. The same result is predicted by the linear stability analysis. The saturation position of the first subharmonic does not change too much for high Reynolds

number simulation. Only one saturation is observed for the fundamental frequency at x=11 and the higher frequencies peaks near the saturation location of the first subharmonic.

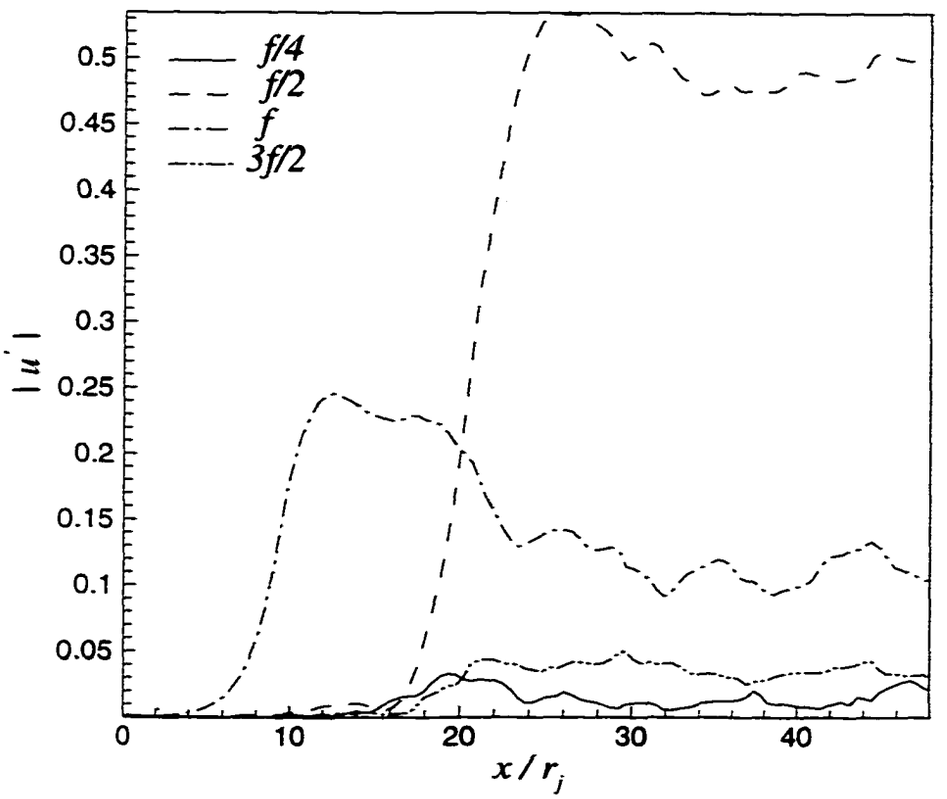

Figure (6.27) Amplitude of axial velocity disturbance versus downstream position at various frequencies (M_j=0.85 and $Re=10^5$)

The momentum thickness of the laminar flow grows very slowly with axial distance since the effect of the viscosity for the high Reynolds number jet is very small. For the perturbed jet, the momentum thickness grows very quickly and two steps-like increase are observed at the vortex pairing positions as clear from Fig. (6.28). The results presented for this case indicate that the effect of the vortex pairing processes on the momentum thickness is very significant even for high Reynolds number flows where the momentum thickness grows very slowly. This result proves that the noise radiation in

subsonic jets is mainly due to the vortex pairing processes at different frequencies. After the completion of the second vortex pairing process, the momentum thickness decays slowly which means that the vortex size decreases slowly as a result of low viscosity effect while the vorticity levels decrease faster for low Reynolds numbers. Subsequently, low Reynolds number jets are more quit at further downstream distances than high Reynolds number jets.

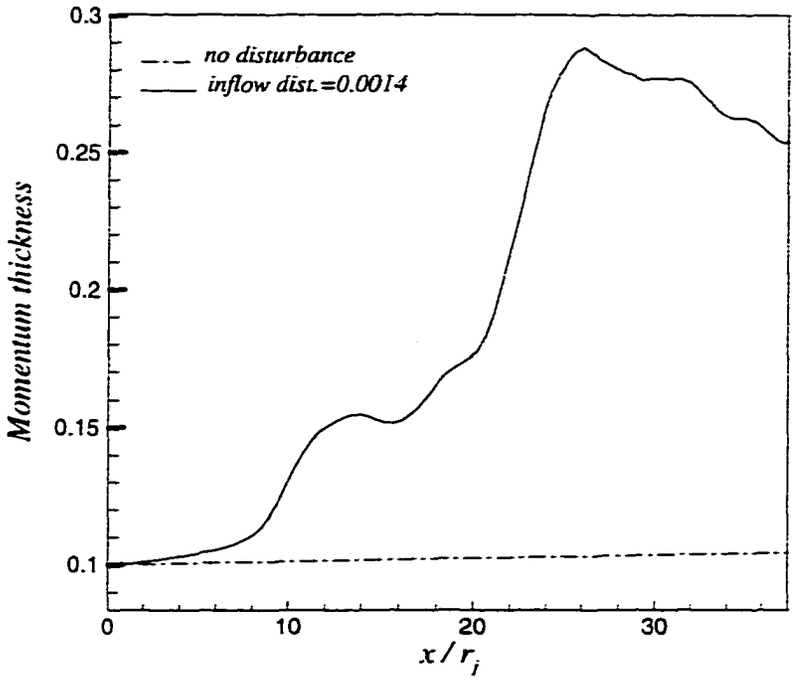

Figure (6.28) Variation of jet momentum thickness with downstream position (M_j=0.85 and $Re=10^5$)

The last conclusion about this case is that MacCormack type schemes, which are used in the current research, can successively predict noise for very high Reynolds number jets schemes while the simulations done by Mitchel, Lele and Moin (1999) using compact schemes is limited to very low Reynolds numbers. MacCormack schemes have some inherent dissipation, which makes these schemes capable of computing jets of high Reynolds numbers.

6.4 Supersonic jet simulations

Two different supersonic cases are computed at various Mach numbers and Reynolds numbers. The calculations include both the near field and the acoustic field. The results of the simulations are analyzed using the Fourier transform and the far field computations are compared with those obtained by the linearized wave Eq. in chapter 8. The optimized dispersion relation-preserving scheme is used in both simulations and characteristic boundary conditions are employed at the inflow boundary.

Case1:

The first simulation is calculated for the same jet conditions used by Mitchel, Lele and Moin (1997). The jet flow parameters are presented in table (6.8). An initial axial velocity profile with momentum thickness 0.05 is used for the laminar flow calculations and the jet temperature is assumed equal to the freestream temperature. The linear stability analysis of the jet mean flow using the initial axial velocity profile indicates that the fundamental frequency is 1.131 (st=0.36) as reported by Mitchel et al (1997). The disturbance is introduced at the inflow boundary with an amplitude 5×10^{-4} and the frequency is the fundamental frequency only. The amplitude of the inflow disturbance is chosen small enough such that the disturbance develops linearly since the noise radiated from supersonic jets is due to the linear instability waves as indicated by Tam and Burton (1984).

Table (6.8) Jet mean flow parameters for supersonic jet ($M_j = 2.0$)

$M_j = \frac{U_j}{\sqrt{\gamma R T_j}}$	$\mathrm{Re} = \frac{U_j \rho_j r_j}{\mu_j}$	$\frac{U_\infty}{U_j}$	$\frac{T_\infty}{T_j}$	Pr	β
2.0	2500	0	1	1	10

The computational domain is extended to 80 radius in the radial direction and 120 radius in the axial direction and the last 35 radius are used for the matching layer. The grid size is 706×750 in the axial and radial directions respectively.The computations are

continued for about 60 cycles until the flow becomes nearly periodic at the outflow boundary and the data of last cycle are stored for the Fourier transform analysis. The momentum thickness for both laminar and disturbed flows is presented in Fig. (6.29). The difference between the momentum thickness of the two flows is very small because the inflow disturbance is forced at very small amplitude which makes the jet develops linearly.

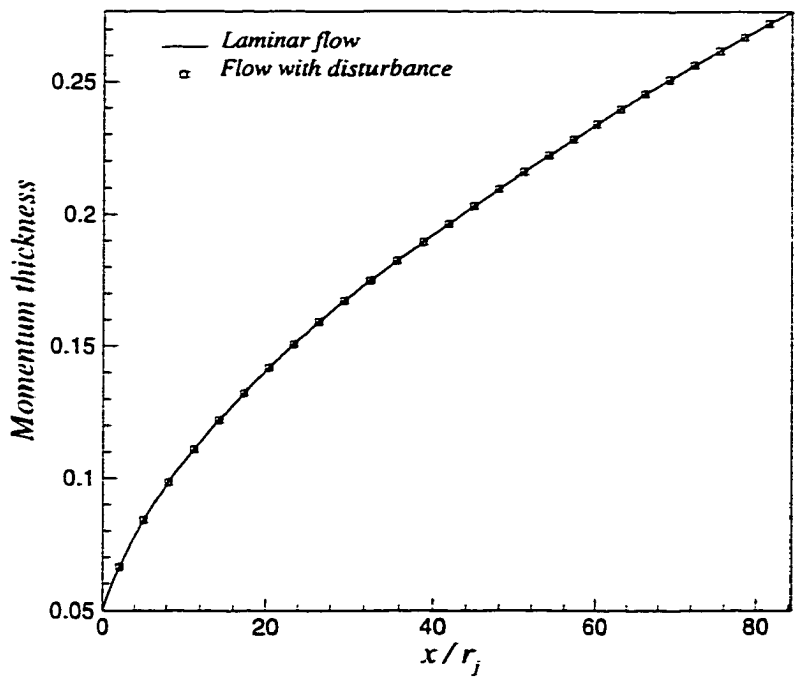

Figure (6.29) variation of momentum thickness with axial distance (M_j=2.0)

The amplitude of the pressure disturbance at the fundamental frequency is presented in Fig. (6.30). It is clear from the graph that the disturbance peaks at x/r_j=25 where the amplitude of the disturbance is about 2.5 the initial amplitude. The same result is obtained by Mitchel et al (1997). The amplitudes of the disturbances at higher frequencies are very small which means that the disturbance is developing linearly and the noise radiation is due to the linear instability waves of the fundamental frequency. The disturbance decays as the flow moves further downstream because the jet mean flow changes due to the effect of the viscosity.

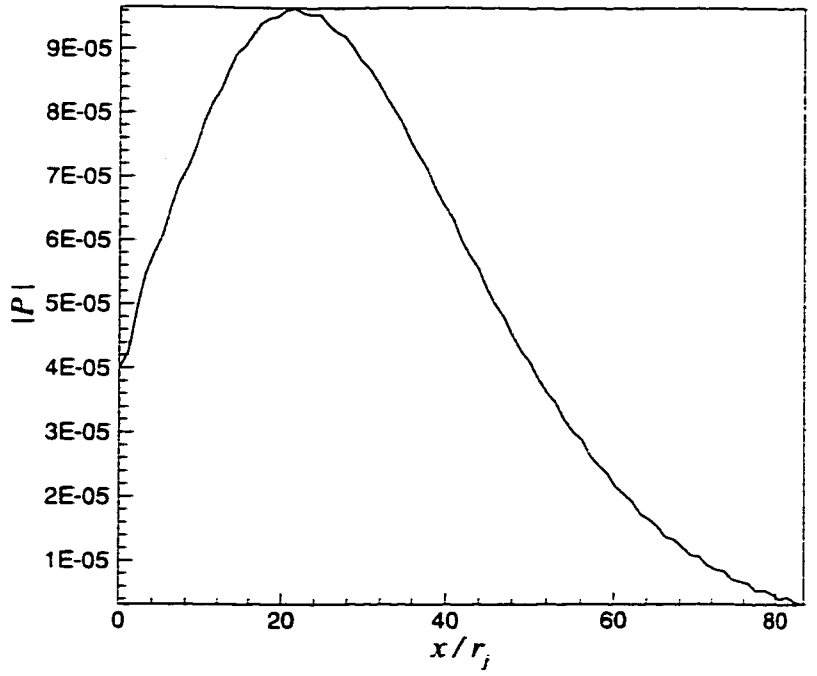

Figure (6.30) Variation of pressure disturbance amplitude near the critical layer at the fundamental frequency with the axial distance (M_j=2.0)

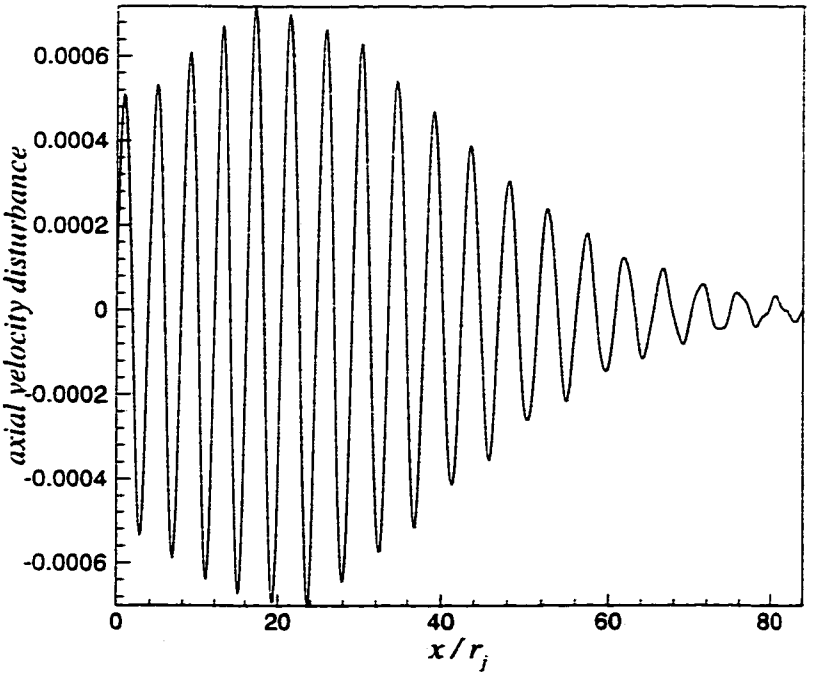

Figure (6.31) Instantaneous axial velocity disturbance versus axial distance (M_j=2.0)

In Figs. (6.31) and (6.32), the growth of the instantaneous axial velocity and pressure disturbances with the axial distance at the critical layer are plotted. The results indicate that the wavenumber of the disturbance is 0.2455 which is the same result obtained by the linear stability theory. As the flow moves downstream, the wavenumber decreases and the jet becomes stable where the instability waves decays to almost zero. The conclusion is that the sound radiated from supersonic jets is due to the linear instability waves and the source region is limited to a narrow distance in the axial direction where most of the noise is emanating from this region.

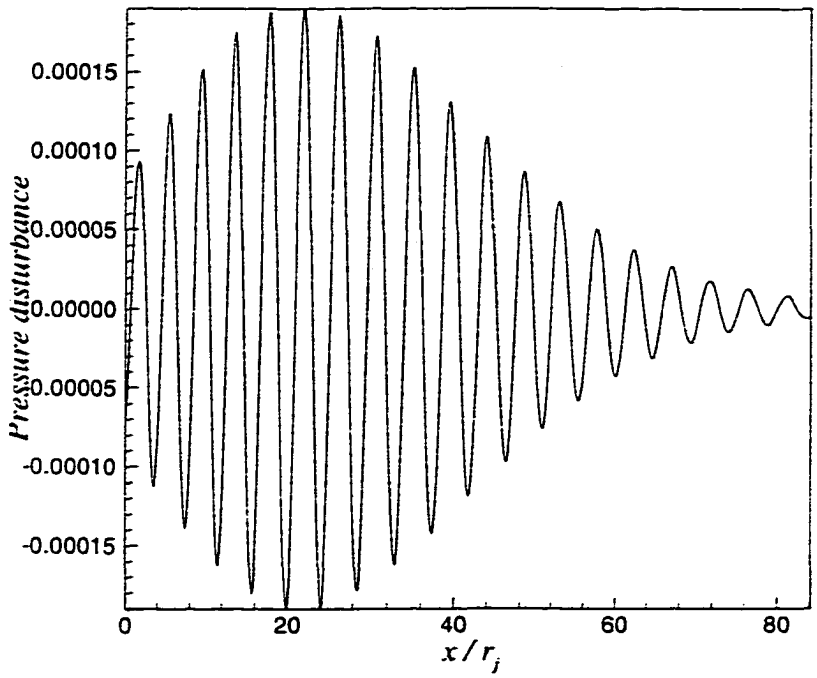

Figure (6.32) Instantaneous pressure disturbance versus axial distance (M_j=2.0)

The instantaneous far field pressure contours are shown in Fig. (6.33). It is clear from the graph that the acoustic waves of supersonic jets propagate within a cone of an angle $\varphi = \sin^{-1}(1/M_0)$, where M_0 is the jet Mach number with respect to the ambient condition, as indicated by Tam and Burton (1984). The results show that the computational domain is long enough in the axial direction to contain the quiet region downstream of the most intense Mach wave radiation. As the acoustic waves propagate to the far field, the region of intensive noise is limited to a narrow layer. The wave

reflections from the boundaries are minimal as clear from the graph, which proves that the matching layer technique has a good behavior at the boundaries.

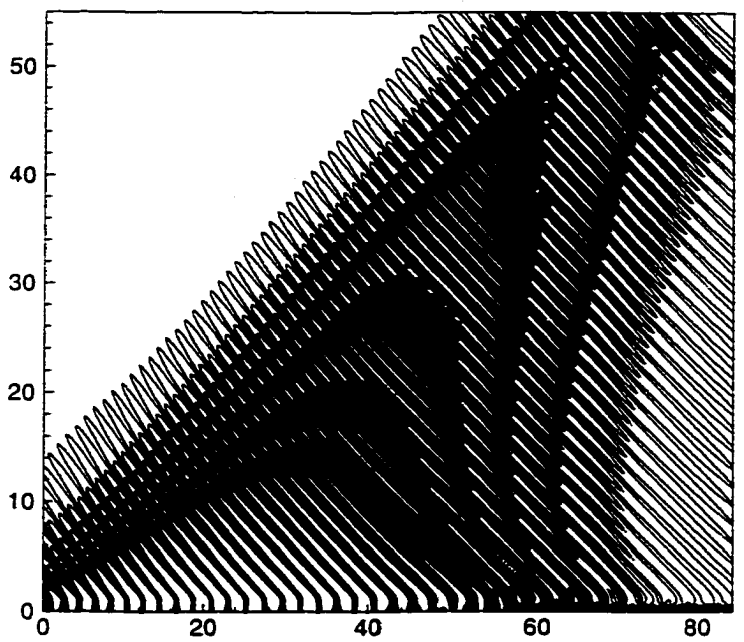

Figure (6.33) Contours of the instantaneous pressure disturbance in the far field with contour levels ranging between $\pm 5.17\times10^{-5}$ and 11 contour levels are used (M_j=2.0)

The amplitude of the pressure disturbance at the fundamental frequency, which is obtained from the Fourier transform analysis, is presented in Fig. (6.34). The directivity pattern of the sound waves in the far field is clear from the graph, which shows an angle of approximately 40^0 for the acoustic wave propagation. As the sound propagates to the far field, the acoustic waves are limited to a narrow region.

The far field dilatation, which is computed from Eq. (6.5), multiplied by the distance R measured from the jet origin is plotted against the angle θ in Fig. (6.35). The results are presented for different positions in the far field. At a distance near the sound source (R=40 and 60), maximum amplitude of the dilatation is obtained on the jet

axis where the source is located. As the distance is increased, maximum dilatation is obtained at $\theta = 40^0$ which is the same result computed by Mitchel et al (1997) as indicated in Fig. (6.36). The dilatation amplitude obtained by Mitchel is different from that computed in the current research because the amplitude of the inflow disturbance used by Mitchel might be higher than that used in the current simulation. The amplitude of the inflow disturbance is not clear in the simulation done by Mitchel.

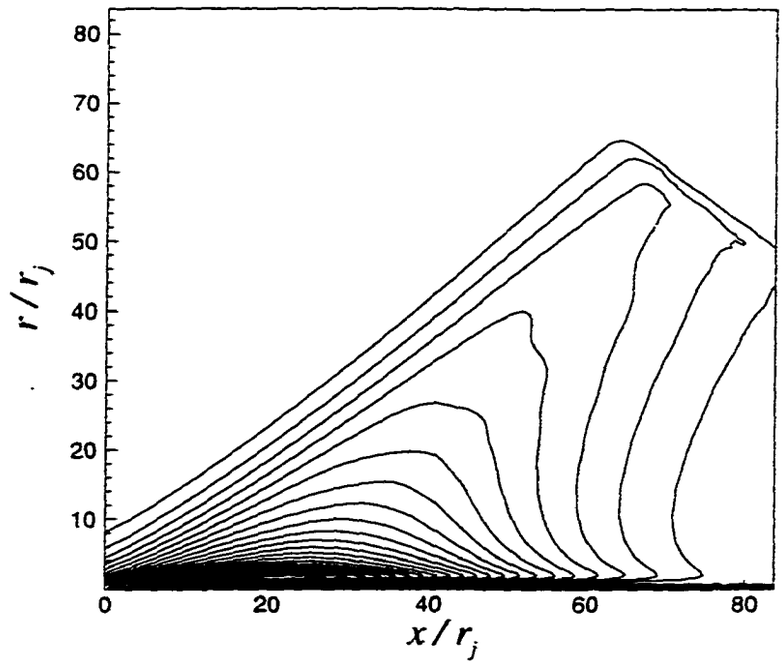

Figure (6.34) Contours of the pressure disturbance amplitude at the fundamental frequency. The maximum and minimum values of the levels are 2.65×10^{-5} and 3.98×10^{-4} and 25 contour levels are used in the graph (M_j=2.0)

The variation of the pressure and axial velocity disturbances with the radial direction is introduced in Fig. (6.37). As computed by the linear stability theory, the disturbances have maximum values at the critical layer and the disturbance oscillates as it propagates to the far field unlike those of the subsonic jets and the disturbance decays in the far field.

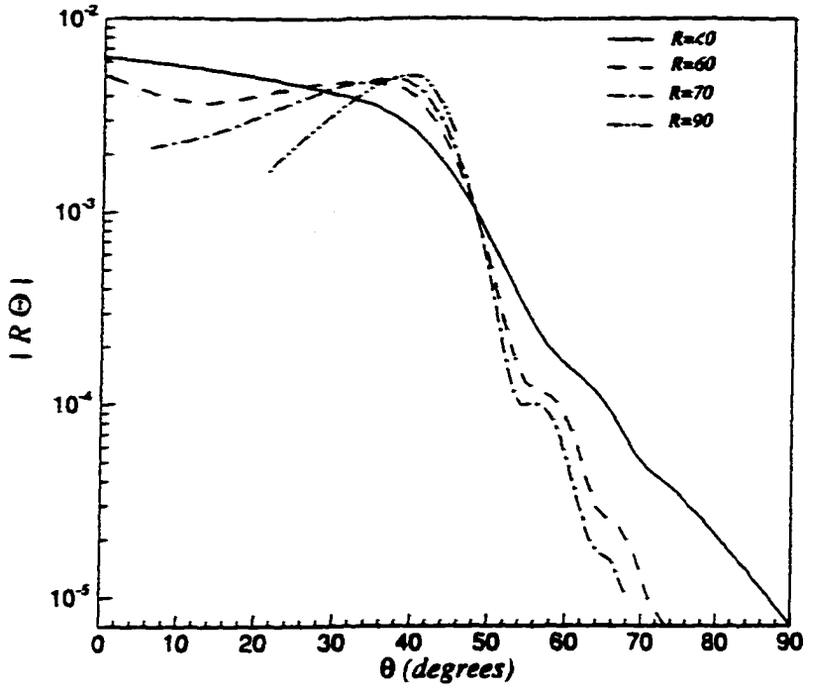

Figure (6.35) Variation of the far field dilatation Θ with the angle θ measured from the jet axis at a distance R from the jet origin (M_j=2.0)

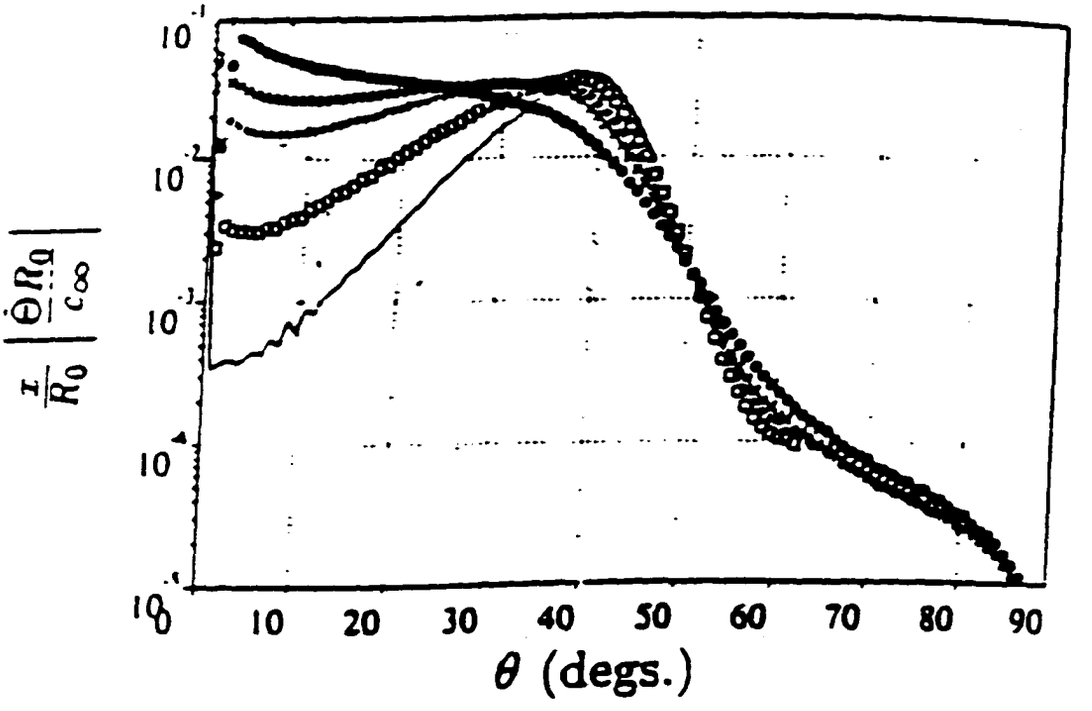

Figure (6.36) Variation of the far field dilatation Θ with the angle θ [Mitchel, Lele and Moin (1997)] (M_j=2.0)

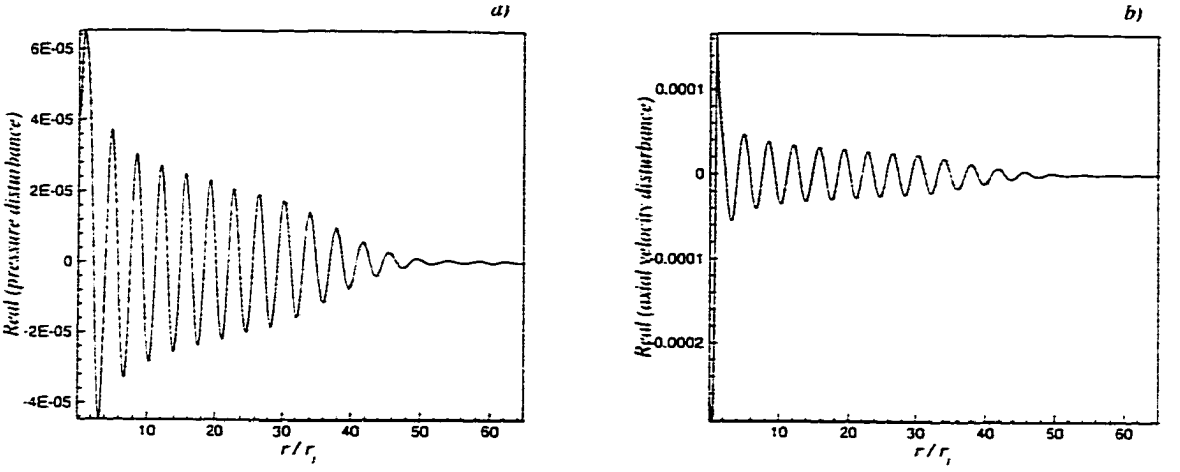

Figure (6.37) Real values of the eigenfunctions versus radial distance at x/r_j=40, (M_j=2.0) a) pressure disturbance b) axial velocity disturbance

Case 2:

The second case is computed at a higher Mach number (M_j=2.5) and Reynolds number (Re=4350). The initial momentum thickness is assumed 0.0455 (β =11) and cold jet is used for the simulation with freestream to jet temperature ratio 2.25 as indicated in table (6.9). The excitation frequency at the inflow boundary is chosen to be 1.7342, which corresponds to Strauhal number of 0.552. The initial amplitude of the disturbance is assumed to be 0.007 and the disturbance is introduced at a single frequency.

Table (6.9) Jet mean flow parameters for supersonic jet ($M_j = 2.5$)

$M_j = \frac{U_j}{\sqrt{\gamma R T_j}}$	$\mathrm{Re} = \frac{U_j \rho_j r_j}{\mu_j}$	$\frac{U_\infty}{U_j}$	$\frac{T_\infty}{T_j}$	Pr	β
2.5	4350	0	2.25	0.72	11

The computational domain is 60x50 radius in the axial and radial directions respectively with grid dimensions 1000x500. The grid is uniform in the axial direction and stretched in the radial direction with minimum grid spacing 0.029 and maximum grid size 0.391. Characteristic boundary conditions are used at the outflow boundaries due to

the size of the grid used in the simulation which does not allow adding matching layers at the boundaries.

A comparison between the momentum thickness of the laminar and disturbed flows is introduced in Fig. (6.38). The results indicate that a small difference between the two flows occurs as a result of introducing disturbances at the inflow boundary, which means that the amplitude of the disturbances at the inflow boundary is small such that the jet develops linearly.

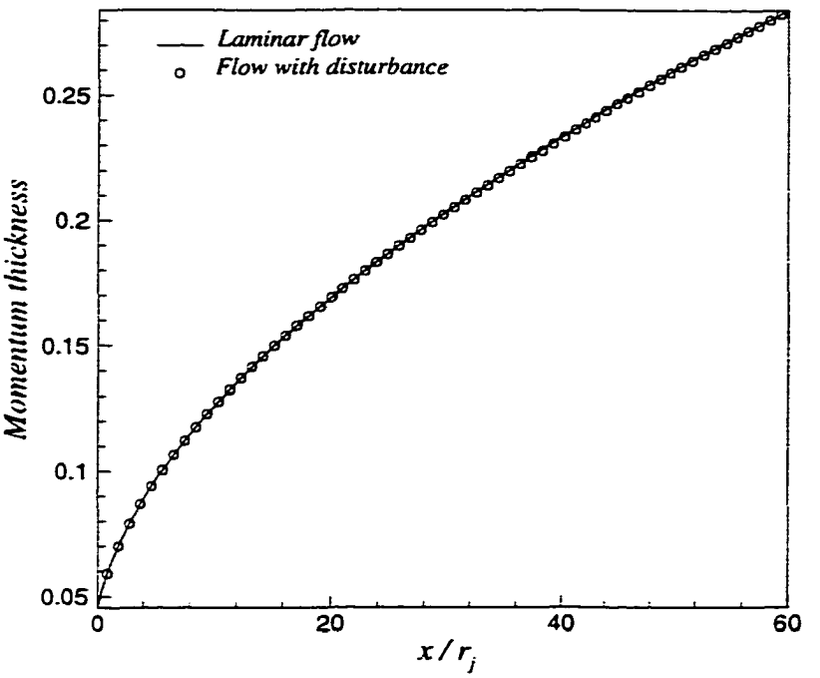

Figure (6.38) variation of momentum thickness with axial distance (M_j=2.5)

The variation of the pressure disturbance amplitude at the critical layer (r/r_j=1), computed using the Fourier transform, with the downstream position is shown in Fig. (6.39). The pressure disturbance peaks at x/r_j=29 and then decays further downstream. The maximum amplitude of the disturbance is 3.87 times the initial amplitude. It is clear from the graph that higher frequency oscillations are obtained near the outflow boundaries due to the characteristic boundary conditions. The overall accuracy of the

computations is not affected by the boundary treatment since the computational domain is long enough to obtain clean results in the source region.

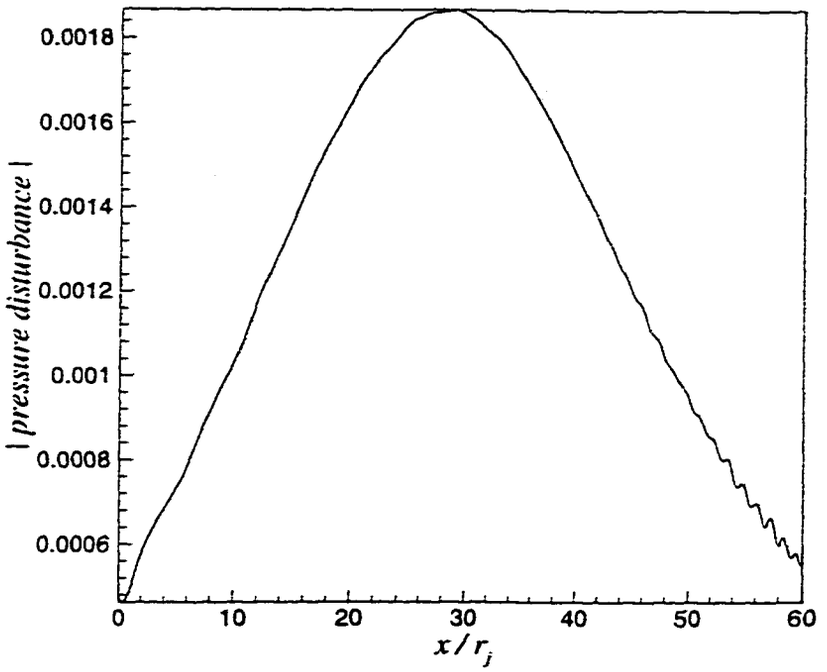

Figure (6.39) Variation of pressure disturbance amplitude near the critical layer at the fundamental frequency with the axial distance (M_j=2.5)

The pressure disturbance contours in the far field give an indication about the directivity pattern and the intense regions of the sound field as shown in Fig. (6.40). The sound radiated to the far field is higher within the Mach cone and quiet outside this region and the sound source is confined within a narrow region, which is limited by approximately 8 jet radius in the radial direction. It is clear from Fig. (6.40) that the computational domain is long enough in the radial direction to contain the quiet region.

The variation of the pressure disturbance with the radial direction is introduced in Fig. (6.41). The pressure disturbance oscillates as it propagates to the far field and it decays in the far field, which is the same result that is obtained by the linear stability theory.

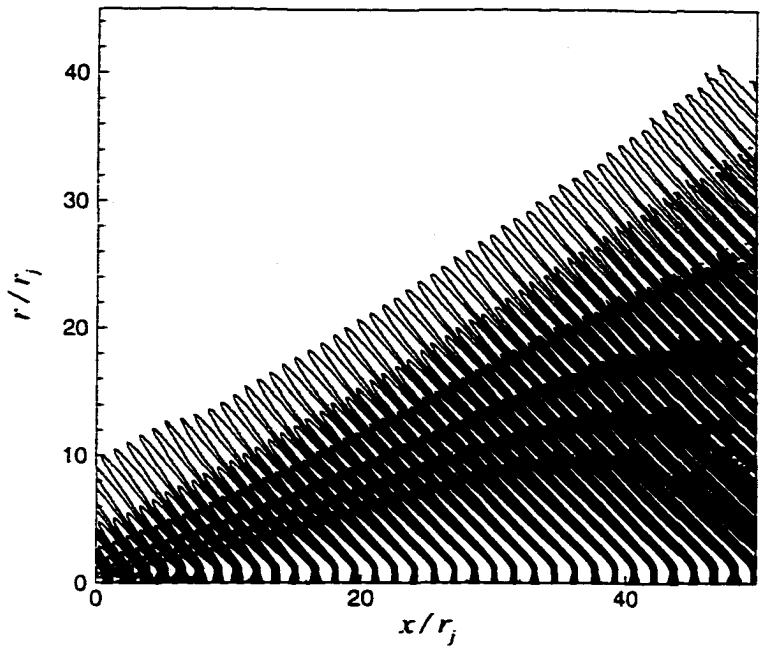

Figure (6.40) Contours of the instantaneous pressure disturbance in the far field with contour levels ranging between ±0.001 and 11 contour levels are used (M_j=2.5)

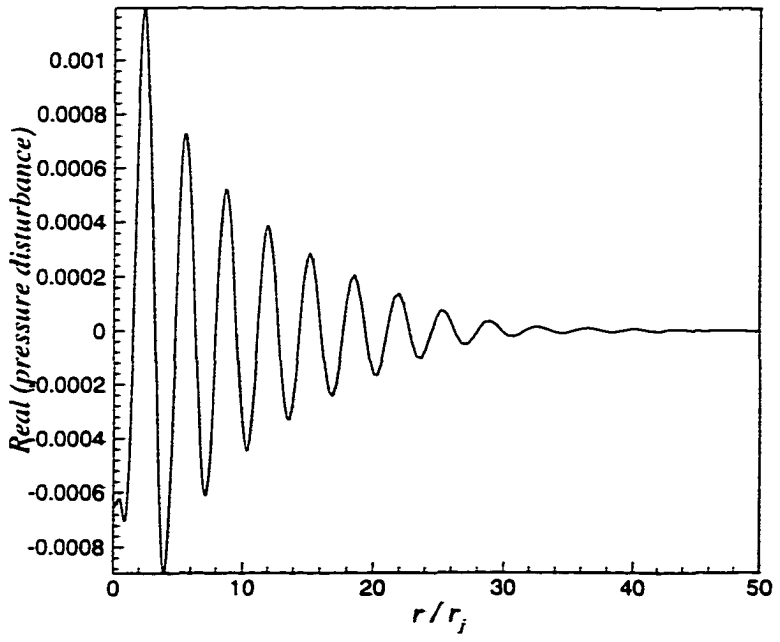

Figure (6.41) Real values of the pressure disturbance versus radial distance at x/r_j=30 (M_j=2.5)

6.5 Summary

In this chapter, DNS of unsteady compressible Navier-Stokes equations is used as a tool to compute the jet noise. The sound source of subsonic and supersonic jets at low and high Reynolds numbers is evaluated. In addition, the computational domain is extended to the far field to compute a significant portion of the acoustic field. High-order accurate MacCormack schemes with operator splitting are used in the computations. A comparison between these schemes shows that the optimized dispersion relation-preserving scheme give better results than other MacCormack schemes. For high number of points per wave length, the two-four scheme and the optimized dispersion relation scheme completely agree with the linear stability results. By decreasing the number of points per wave length, the dissipation and dispersion errors for the two-four scheme increases and the results obtained are different from those obtained using higher order accurate MacCormack schemes. Thus, explicit MacCormack scheme, with operator splitting and a finite difference formula derived from the central difference of the original dispersion relation-preserving scheme by Tam and Webb (1992), is adopted in the current work for jet noise computations.

Different outflow boundary conditions are presented in the current work for the treatment of the boundaries. The results presented in this chapter show that the perfectly matching layer technique produces minimum reflections at the outflow boundaries compared with the characteristic boundary conditions and buffer domain method. In addition, the perfectly matching layer technique is computationally less expensive than the buffer domain since it requires using few number of points. Hence, most of the simulations done in the current work are computed using the perfectly matching layer technique.

The results of five different cases are presented for subsonic and supersonic jets. For subsonic jets, the results indicate that the vortex pairing process plays a major role in the noise generation. This result agrees with the experiment of Laufer and Yen (1983) and with the numerical simulations of Mitchel et al (1999). Moreover, the noise computed in the far field for supersonic jets is in good agreement with the results

obtained by Mitchel et al (1997). The same directivity pattern, pressure disturbance contours and dilatation contours in the acoustic field are obtained as reported by Mitchel et al (1997).

Chapter 7

Three Dimensional Jet Simulation

7.1 Introduction

The development of three-dimensional axisymmetric disturbances in a subsonic jet (M_j=0.8) is investigated with emphasis on the near field computations. The simulation is done for low Reynolds number (Re=2500) and thick shear layer with an initial momentum thickness of 0.1. The azimuthal wave number is assumed to be one at the inflow boundary and the inflow disturbances are introduced at the fundamental frequency with initial amplitude of 5×10^{-4}. The disturbances are obtained from the linear stability theory and introduced at the boundary in the following form

$$Q_{dist} = \mathrm{Re}\,al[Q(r)e^{-i\omega t}]\cos\theta \qquad (7.1)$$

where, $Q = [\rho \;\; u \;\; v \;\; w \;\; p]^{trans}$

Due to the large computations required for three-dimensional jet simulation, the computational domain is limited to 20 radius in the axial direction and 13 radius in the radial direction. Only half of the jet in the azimuthal direction is computed because the disturbances are symmetric. The grid size is 250×130×60 in the axial, radial and azimuthal directions respectively. Characteristic boundary conditions are used at the outflow boundaries and Giles (1990) boundary conditions are employed at the inflow boundary. Moreover, a numerical filter is used in the azimuthal direction to damp out the high frequency oscillations.

7.2 Results

The computations are continued for 12 cycles of the fundamental frequency until the flow becomes periodic at the outflow boundary. The results are stored during the last cycle of the computations for the Fourier transform analysis. The variation of the azimuthal velocity component with the angular position at the critical layer is shown in

Fig. (7.1) at different axial positions. The amplitude of the azimuthal velocity increases as the flow moves further downstream. In addition, higher modes are developed in the azimuthal direction as a result of the disturbance growth. Near the inflow boundaries (x/r_j=5), only one helical mode (n=1), which is introduced at the inflow boundary, is developed in the jet flow. while higher modes are developed in the azimuthal direction at the outflow boundaries as clear from the graph.

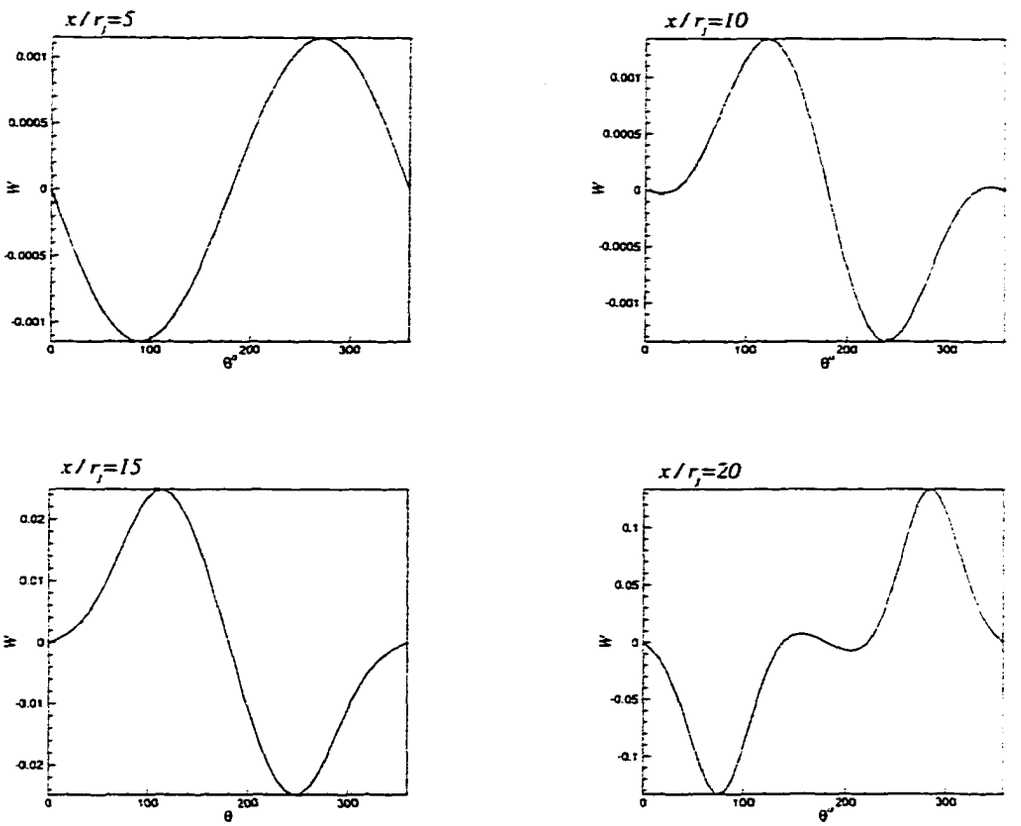

Fig. (7.1) Variation of azimuthal velocity with the angle θ at different axial positions (M_j=0.8)

In Fig. (7.2), the pressure disturbance contours at different axial positions in the (r, θ) plane are shown. The contours are presented in the near field with maximum radial position of 13 jet radius. The number of contour levels shown in each graph are 16 and the contour values range between $\pm 3.4\times10^{-4}$, $\pm 7.2\times10^{-4}$ and $\pm 9.7\times10^{-4}$ for the first, second and third graphs respectively. It is clear from the graphs that the pressure disturbance near

the inflow boundary ($x/r_j=5$) appears to be antisymmetric around the plane $\theta=\pi/2$ and high disturbance amplitudes are radiated from the critical layer. As the disturbance amplitude grows at further downstream positions, higher modes are developed in the azimuthal direction and the pressure disturbance is no longer antisymmetric around $\theta=\pi/2$.

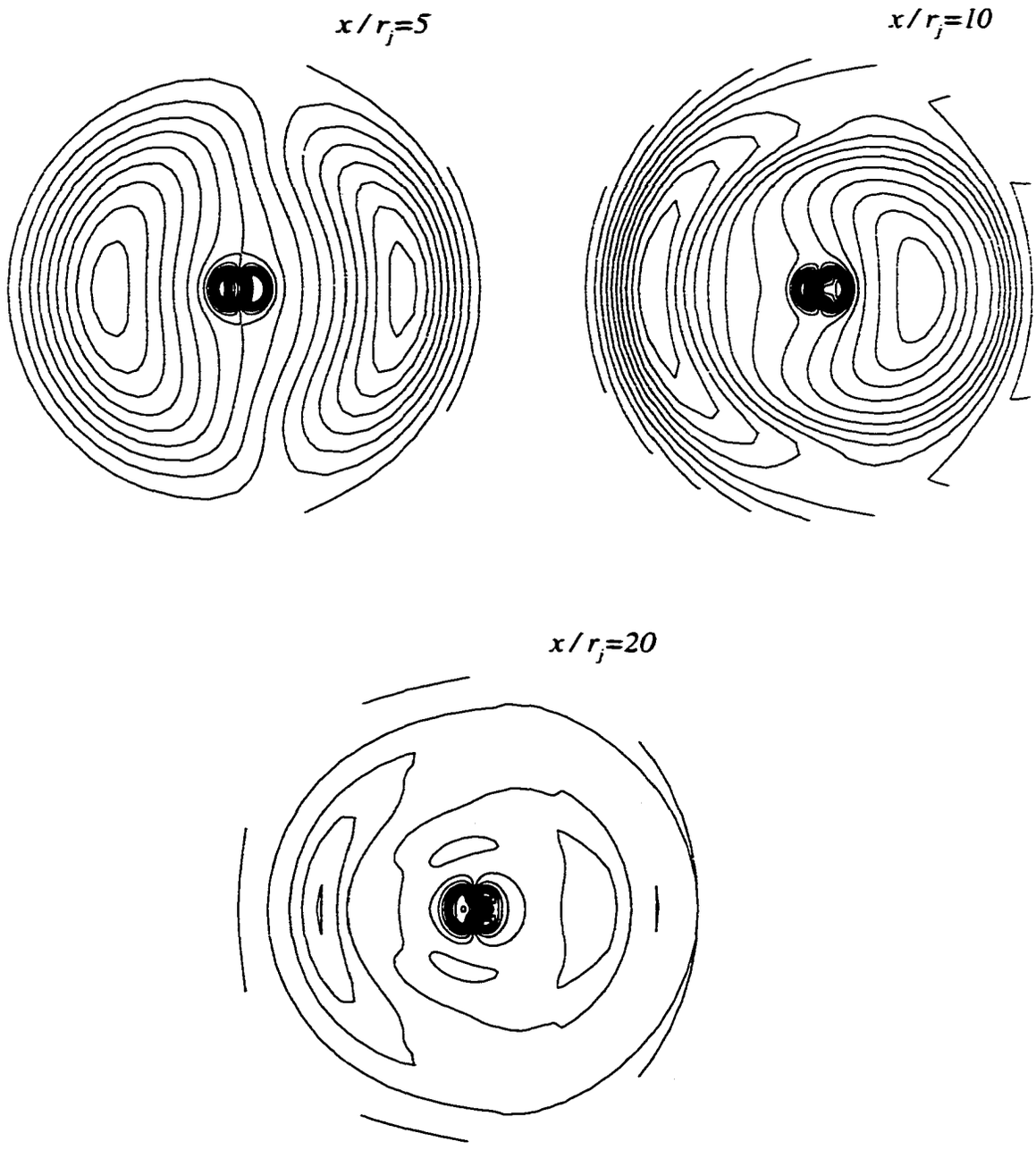

Fig. (7.2) Pressure contours in (r,θ) plane at different axial positions (M_j=0.8)

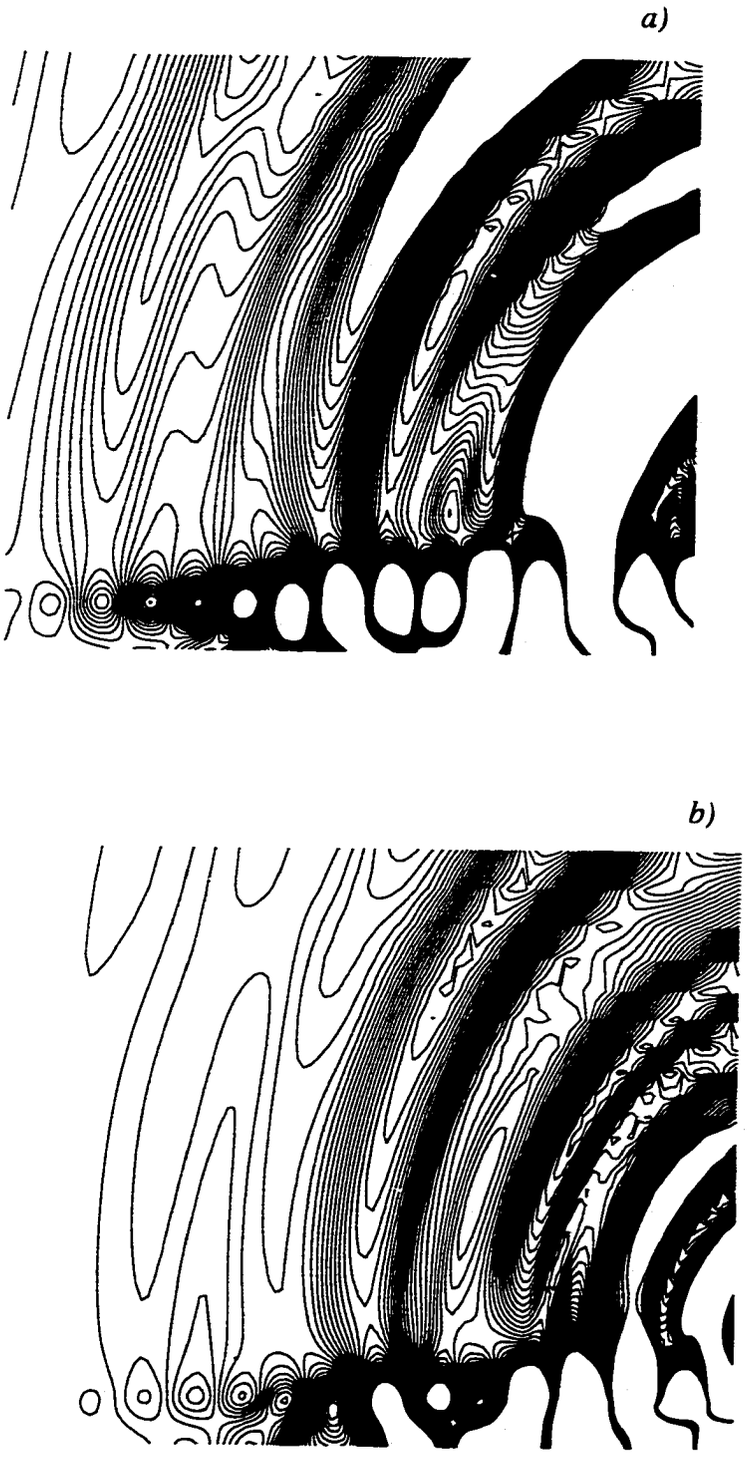

Fig. (7.3) Pressure contours in (x,r) plane at two different azimuthal positions (M_j=0.8) a) $\theta=0$ b) $\theta=\pi/2$

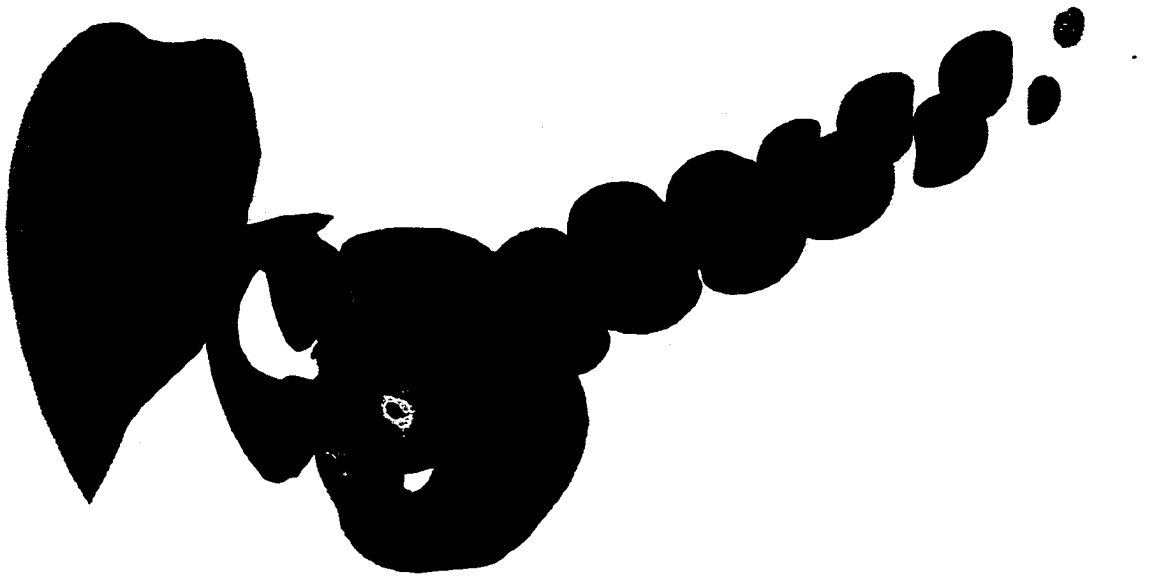

Fig. (7.4) Pressure iso-surface for subsonic jet (M_j=0.8) with pressure levels $\pm 4\times10^{-3}$ and 17 levels

The pressure disturbance contours in the (x,r) plane are plotted at two different azimuthal positions as shown in Fig. (7.3). The contours are shown within 20 radius in the axial direction and 13 radius in the radial direction. The maximum and minimum values of the contour levels are $\pm 1\times10^{-3}$ and 41 levels are used in the graphs. The upstream influence of the pressure disturbances is clear from the graph at both azimuthal positions and the disturbances propagate in semi circles. In Fig. (7.4), the pressure iso-surface is presented where the helical nature of the jet structure and the roll-up are evident as reported by Shih and Hixon (1995), and Freund, Moin and Lele (1997).

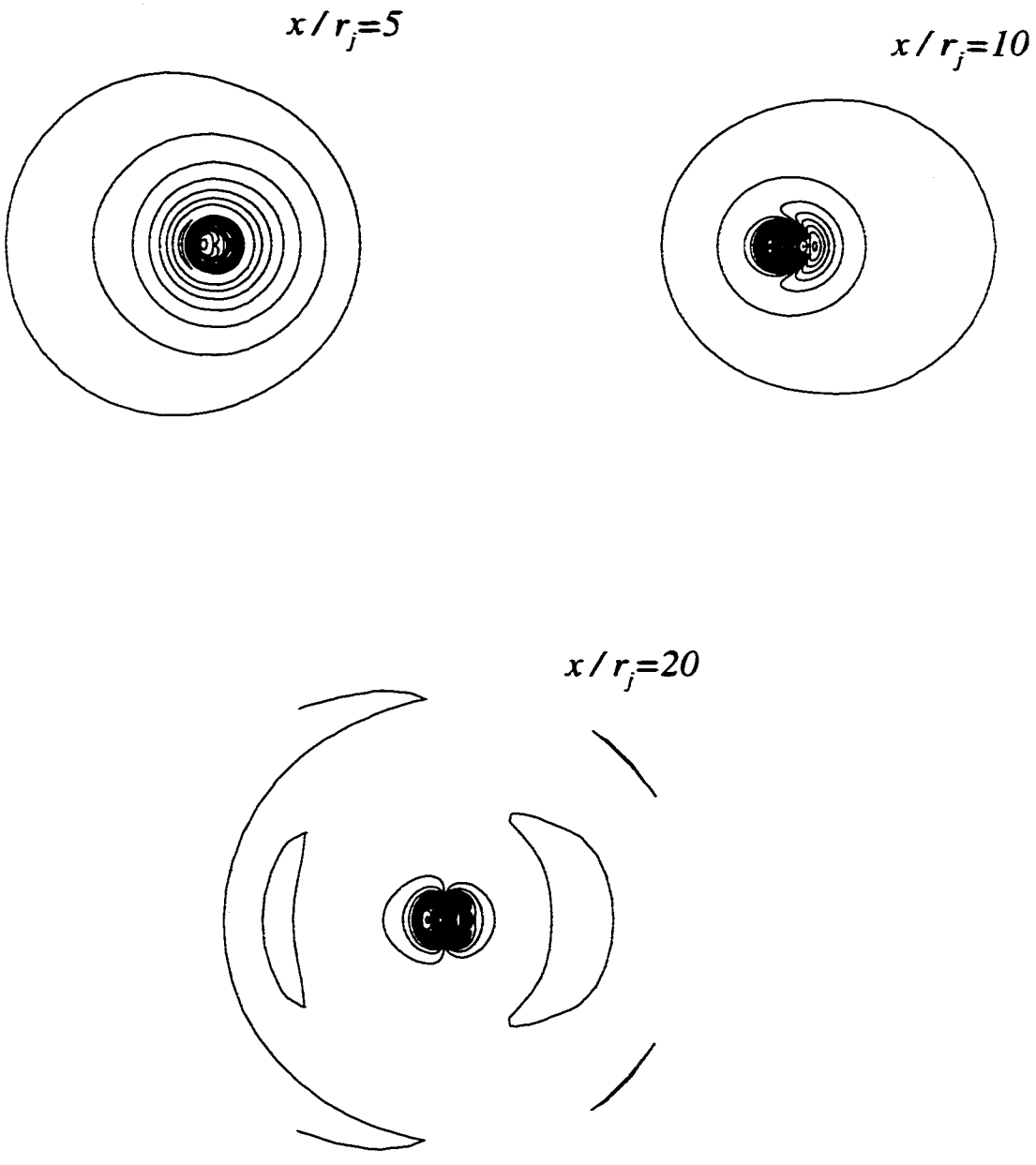

Fig. (7.5) Normal velocity contours in (r, θ) plane at different axial positions (M_j=0.8)

The normal velocity contours in the (r, θ) plane are introduced at different axial positions as shown in Fig. (7.5). The contour values are in the range of $\pm 5\times10^{-3}$ and 15 levels are used in the graphs. The disturbances appear to be radiated from the jet axis

where quadrupoles are distributed. This can be seen clearly at larger distances from the inflow boundary where higher helical modes are developed.

The amplitude of the axial velocity disturbance obtained from the Fourier transform analysis at different azimuthal wavenumbers is shown in Fig. (7.6). The results are presented at different radial positions and frequencies. At the jet centerline, the mode (1,1) is the dominant mode while the most dominant mode at the critical layer is (1,4) as shown also in Figs. (7.7) and (7.8). It is evident from Fig. (7.6) that too many modes are developed at the critical layer while few modes are generated near the centerline.

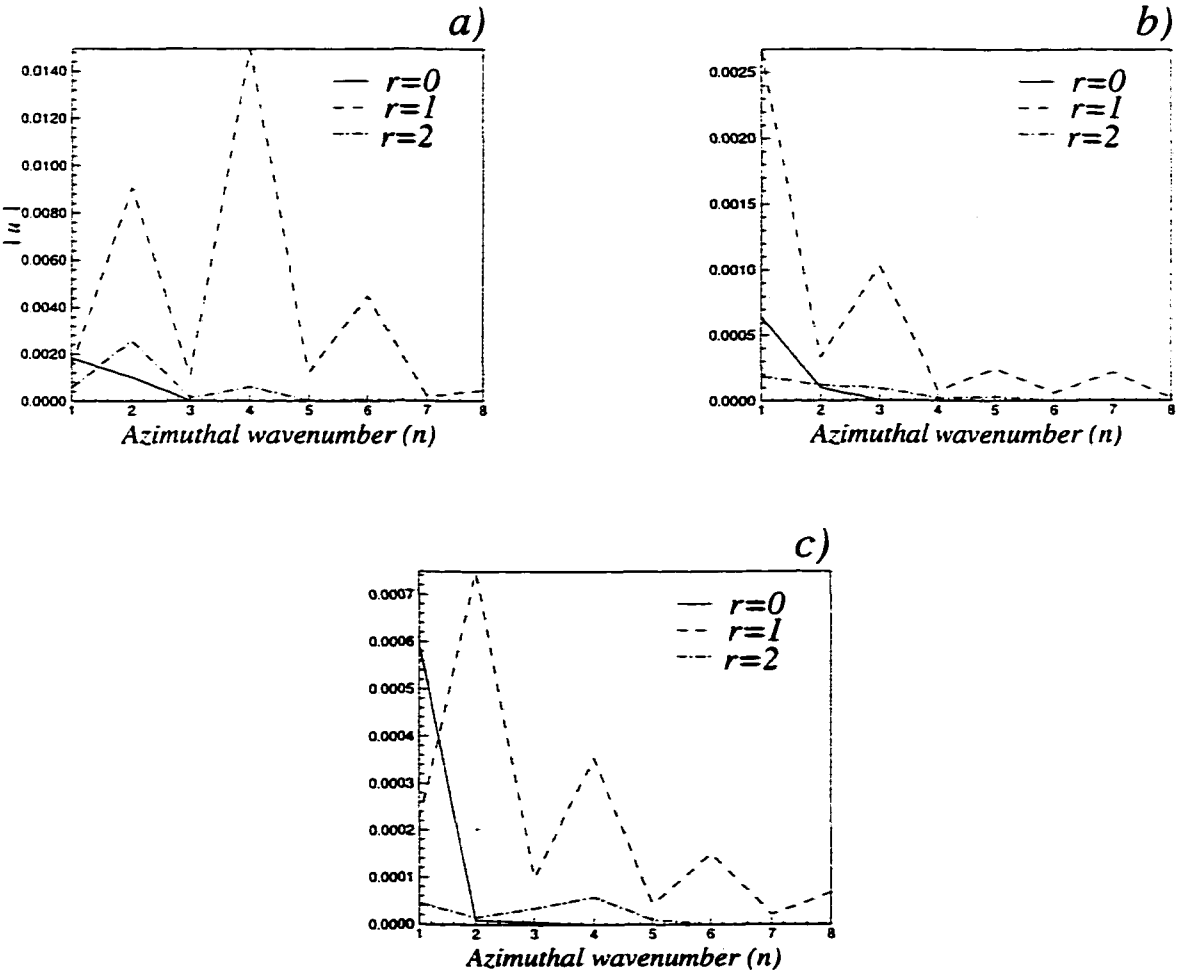

Fig. (7.6) Amplitude of axial velocity disturbance versus azimuthal wavenumber at different radial positions (x/r_j=18) and a) for the fundamental frequency ω b) 2ω c) 3ω

The disturbances generated at the fundamental frequency have higher amplitudes than those generated at 2ω and 3ω. For the fundamental frequency ω and 3ω, even modes $(\omega,2)$, $(\omega,4)$, $(\omega,6)$ and $(\omega,8)$ are dominant at the critical layer while odd modes generated at 2ω are more dominant than the even modes generated at the same frequency. At the centerline, odd modes generated at ω, 2ω and 3ω have higher amplitudes than the even modes.

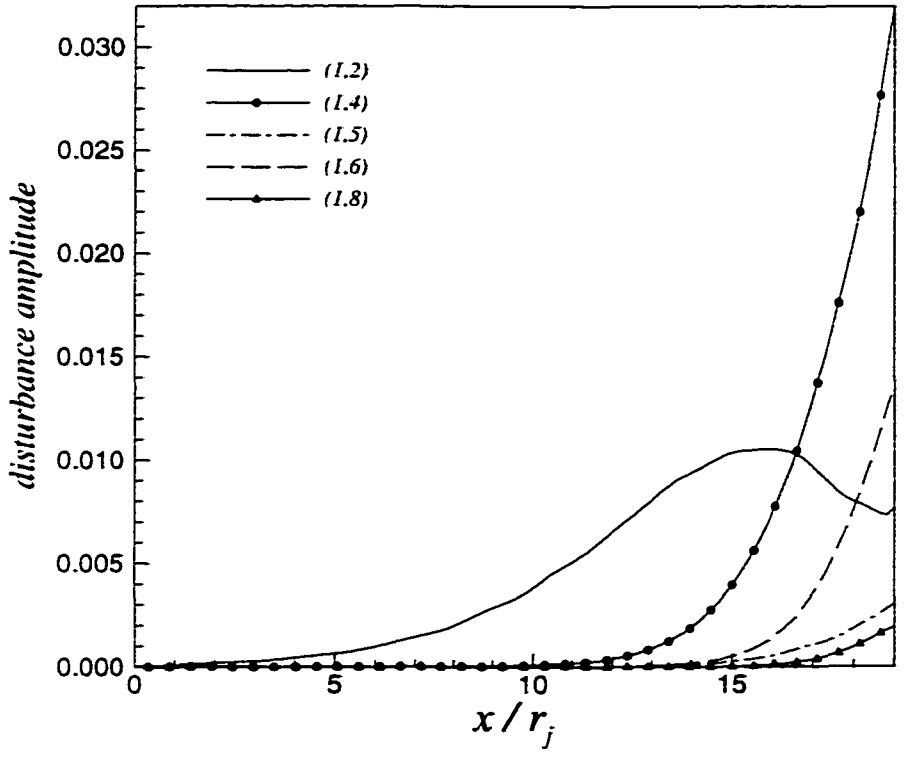

Fig. (7.7) Amplitude of axial velocity disturbance versus axial positions for different modes $[\omega,n]$ and at the critical layer (M_j=0.8)

In Figs. (7.7) and (7.8), the disturbance amplitude generated at different modes for ω and 2ω are plotted versus the axial distance. The disturbances developed at the fundamental frequency have larger amplitudes than that generated at 2ω. It is evident from the graphs that the disturbances for most of the modes are still growing and a larger distance in the axial direction is needed in order to obtain the saturation.

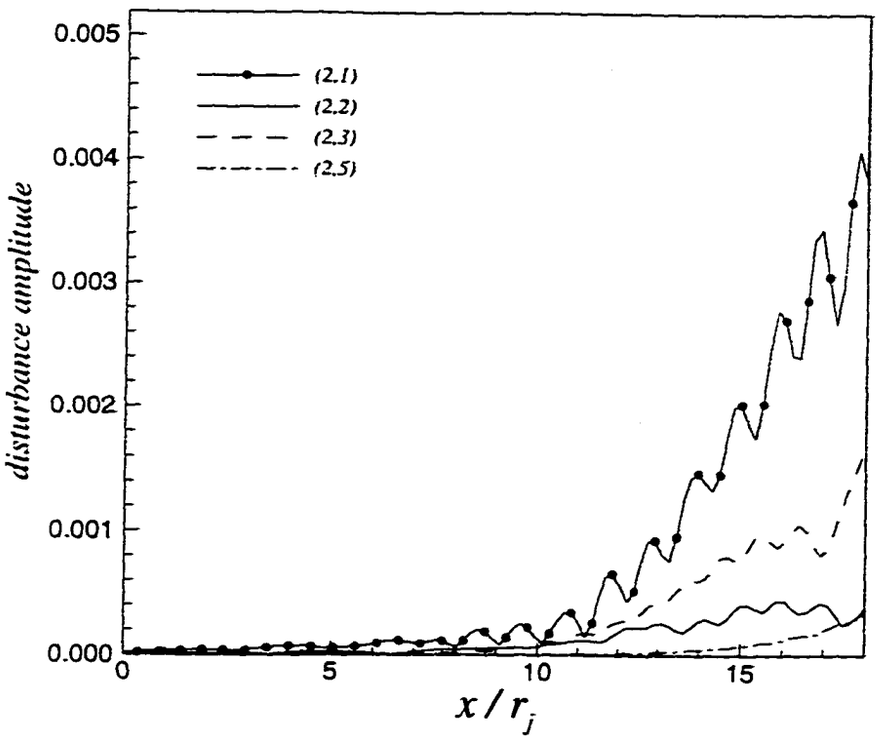

Fig. (7.8) Amplitude of axial velocity disturbance versus axial positions for different modes $[2\omega,n]$ and at the critical layer (M_j=0.8)

Chapter 8

Acoustic Field Computations

8.1 Introduction

The acoustic field computations provide information about the directivity pattern and the acoustic waves of the sound radiated from the jet mixing layer. Computing the acoustic field using Navier-Stokes equations requires huge computational efforts and computer capabilities, which are not always available. In addition, the numerical errors due to the discretized equations contaminate the acoustic field and produce spurious waves at the boundaries. Thus the solution is extended to the far field using the linearized wave equation which is the linearized Euler equation for zero mean velocities. The pressure disturbances obtained from Navier-Stokes computations in the near field are stored at particular radial positions where the radial velocity component is small. The disturbances are then submitted to the linearized wave equation at the boundary.

The results obtained from the linearized wave equation are compared with those obtained from Navier-Stokes equations for some cases where the near field solution is extended to a large distance in the far field. Thus, the accuracy of the far field computations is tested for both Navier-Stokes and linearized wave equations.

8.2 Governing equations

The disturbance propagation in the far field is governed by the linearized Euler equations because the viscous effects are negligible in the far field and the nonlinear effects are confined to a narrow region in the near field. Hence, the linearized Euler equations in cylindrical coordinates are used to obtain the disturbances in the far field and the equations are expressed in the following form for stationary medium:

$$\frac{\partial u}{\partial t} = -\frac{1}{\rho_m}\frac{\partial p}{\partial x}$$

$$\frac{\partial v}{\partial t} = -\frac{1}{\rho_m}\frac{\partial p}{\partial r} \tag{8.1}$$

$$\frac{\partial w}{\partial t} = -\frac{1}{r\rho_m}\frac{\partial p}{\partial \theta}$$

$$\frac{\partial p}{\partial t} + \frac{1}{M_o^2}\left(\frac{1}{r}\frac{\partial w}{\partial \theta} + \frac{v}{r} + \frac{\partial v}{\partial r} + \frac{\partial u}{\partial x}\right) = 0$$

Eliminating the velocity components from the pressure equation in terms of the pressure derivatives, the following linearized wave equation is obtained

$$\frac{\partial^2 p}{\partial t^2} - \frac{1}{\rho_m M_o^2}\left(\frac{1}{r^2}\frac{\partial^2 p}{\partial \theta^2} + \frac{1}{r}\frac{\partial p}{\partial r} + \frac{\partial^2 p}{\partial r^2} + \frac{\partial^2 p}{\partial x^2}\right) = 0 \tag{8.2}$$

where ρ_m and T_o is the mean density and temperature in the far field. The Mach number M_o in Eq. (8.2) is defined as

$$M_o = \frac{u_j}{\sqrt{\gamma R T_o}} \tag{8.3}$$

8.3 Boundary conditions

Boundary conditions are needed at the boundary separating the near field and far field computations as shown in Fig. (8.1). These boundary conditions are defined in terms of the instantaneous pressure obtained from the Navier-Stokes computations at certain radial position (r_o) where the pressure is known as function of time, azimuthal direction and axial position. The pressure is applied at the boundary as Dirichliet boundary condition.

$$p_o = p(x, r_o, \theta, t) \tag{8.4}$$

In addition, radiation boundary conditions are needed at all other boundaries to allow the acoustic waves to cross the boundaries with minimum reflections. The following radiation boundary condition derived by Tam (1980) is utilized:

$$\frac{1}{C_o}\frac{\partial p}{\partial t}+\frac{\partial p}{\partial R}+\frac{p}{R}=0 \tag{8.5}$$

where R is the distance measured from the sound source in spherical coordinates and C_o is speed of sound in the far field.

$$R=\sqrt{x^2+r^2} \tag{8.6}$$

Then Eq. (8.5) can be rewritten in cylindrical coordinates as follows:

$$\frac{1}{C_o}\frac{\partial p}{\partial t}+\frac{x}{R}\frac{\partial p}{\partial x}+\frac{r}{R}\frac{\partial p}{\partial r}+\frac{p}{R}=0 \tag{8.7}$$

For two-dimensional axisymmetric jet, the non-homogenous term (p/R) in Eq. (8.7) is divided by 2R rather than R (Roe 1989).

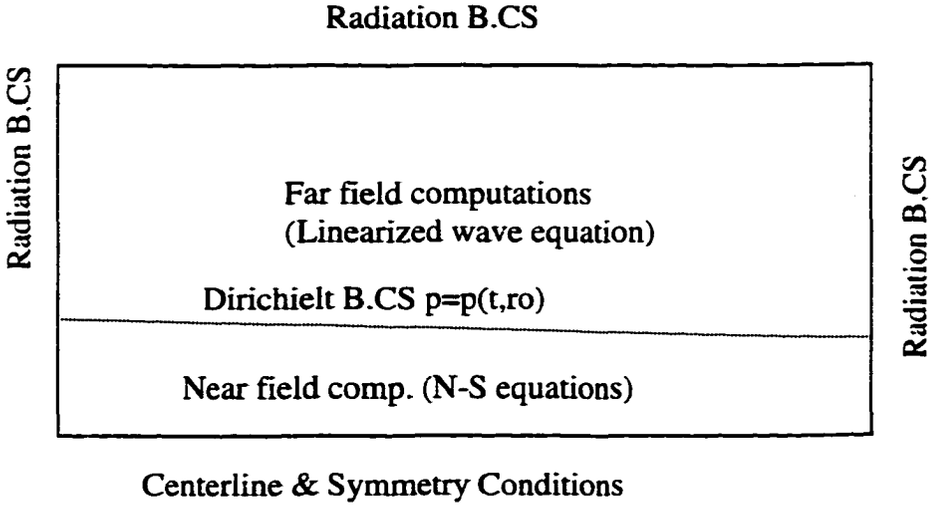

Figure (8.1) Computational domain and boundary conditions for wave equation.

8.4 Numerical discretization

The wave equation, Eq. (8.2), and the boundary conditions given by Eqs. (8.4) and (8.7) are discretized using sixth-order compact finite difference scheme which is Pade scheme. Fourth-order Runge-Kutta presented in chapter 5 is used to integrate the time derivatives. The first order spatial derivatives are discretized implicitly as follows.

$$p'_{i+1} + 3p'_i + p'_{i-1} = \frac{7}{3}\frac{p_{i+1} - p_{i-1}}{\Delta x} + \frac{1}{12}\frac{p_{i+2} - p_{i-2}}{\Delta x} \tag{8.8}$$

At points near the boundaries *(i=2 and imax-1)*, the scheme is changed to the standard centered fourth-order compact scheme as suggested by Freund, Moin and Lele (1997) and the first derivatives are discretized as

$$\begin{aligned} p'_{i\max} + 4p'_{i\max-1} + p'_{i\max-2} &= 3\frac{p_{i\max} - p_{i\max-2}}{\Delta x} \\ p'_1 + 4p'_2 + p'_3 &= 3\frac{p_3 - p_1}{\Delta x} \end{aligned} \tag{8.9}$$

While at the boundaries (*i=1 and imax*), a one sided third-order finite difference is applied which maintains the tridiagonal nature of the system.

$$\begin{aligned} 2p'_{i\max} + 4p'_{i\max-1} &= \frac{5p_{i\max} - 4p_{i\max-1} - p_{i\max-2}}{\Delta x} \\ 2p'_1 + 4p'_2 &= \frac{-5p_1 + 4p_2 + p_3}{\Delta x} \end{aligned} \tag{8.10}$$

The second derivatives are discretized at the interior points as follows

$$2p''_{i+1} + 11p''_i + 2p''_{i-1} = 12\frac{p_{i+1} - 2p_i + p_{i-1}}{\Delta x^2} + \frac{3}{4}\frac{p_{i+2} - 2p_i + p_{i-2}}{\Delta x^2} \tag{8.11}$$

At and near the boundaries, the finite difference forms are changed to the following expressions

$$p''_{i\max} + 10p''_{i\max-1} + p''_{i\max-2} = \frac{12p_{i\max} - 24p_{i\max-1} + 12p_{i\max-2}}{\Delta x^2} \tag{8.12}$$

$$p''_1 + 10p''_2 + p''_3 = \frac{12p_3 - 24p_2 + 12p_1}{\Delta x^2} \tag{8.13}$$

$$11p''_{i\max-1} + p''_{i\max} = \frac{13p_{i\max} - 27p_{i\max-1} + 15p_{i\max-2} - p_{i\max-3}}{\Delta x^2} \tag{8.14}$$

$$11p''_2 + p_1 = \frac{13p_1 - 27p_2 + 15p_3 - p_4}{\Delta x^2} \tag{8.15}$$

8.5 Results

Three different cases are computed for supersonic and subsonic jets with high and low Reynolds number. The results presented here include directivity pattern of the sound radiated to the far field and the pressure disturbances contours in the acoustic field. All the computations are done for two-dimensional axisymmetric jets.

8.5.1 Supersonic jet

The far field computations of a supersonic jet are introduced in this section. The near field predictions of this jet using Navier-Stokes equations are presented in chapter 6 section 6.4. The jet Mach number is 2 and Reynolds number is 2500. Using the Fourier transform of the disturbances in the near field, it is predicted that the sound source of this jet is located at 20 radius on the jet axis.

The pressure disturbances in the near field are stored at 8 radius in the radial direction for the far field calculations. The computational domain for the acoustic field computations is 84 radius in the axial direction and 80 radius in the radial direction with grid size of 500×500. The time step used for the solution of the linearized wave equation is 0.016.

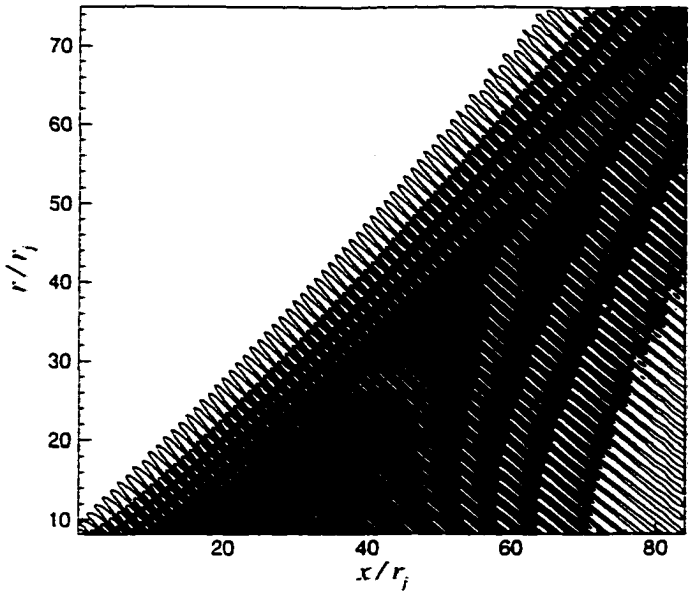

Figure (8.2) Contours of the instantaneous pressure disturbance in the far field obtained using linearized wave equation. The contour levels range between $\pm 5.17\times10^{-5}$ and 16 contour levels are used (M_j=2.0)

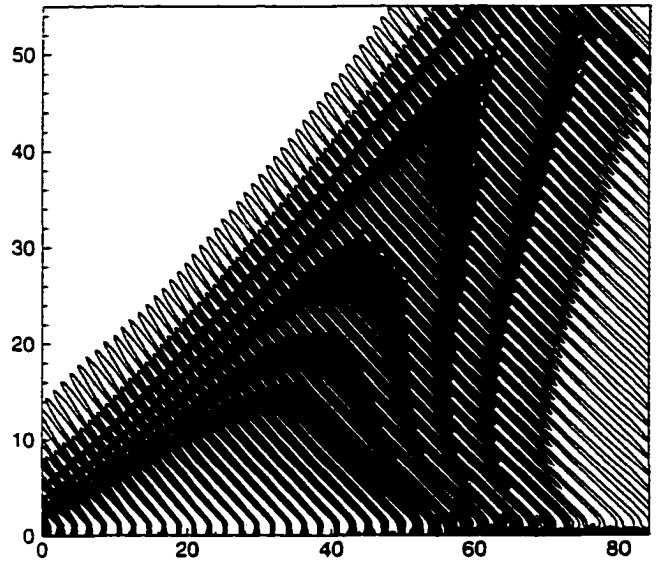

Figure (8.3) Contours of the instantaneous pressure disturbance in the far field obtained using Navier-Stokes equations. The contour levels range between $\pm 5.17\times10^{-5}$ and 16 contour levels are used (M_j=2.0)

The instantaneous far field pressure disturbance contours are presented in Fig. (8.2). Comparing Fig. (8.2) with Fig. (8.3), which is obtained from the direct computations of Navier-Stokes equations, shows an excellent agreement between the computations of linearized wave equation and Navier-Stokes equations in the acoustic field. Similar wave propagation angles are obtained from both calculations. Although the radiation boundary conditions produce some reflections at the boundaries as clear from the pressure disturbance contours, the overall accuracy of the far field computations is not affected and the whole acoustic field is not contaminated by these reflections.

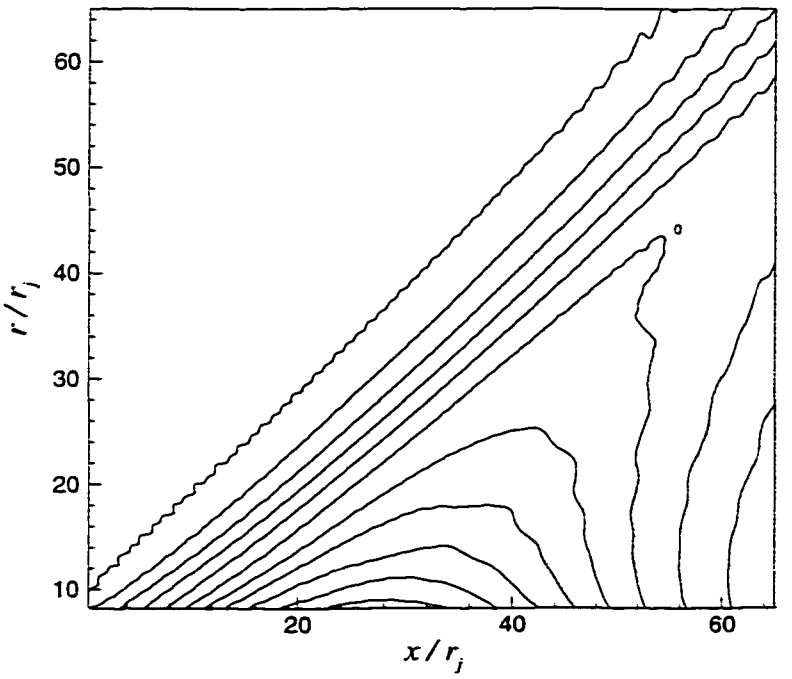

Figure (8.4) Contours of the dilatation amplitudes in the far field with contour levels ranging between 1.896×10^{-6} and 3.979×10^{-5} and 11 contour levels are used (M_j=2.0)

For uniform mean flow, the dilatation is expressed in terms of the time derivative of the pressure disturbance as indicated in Eq. (8.16). The amplitudes of the dilatation in the far field, that are obtained from the Fourier transform analysis of the data stored during the last cycle of the computations, are introduced in Fig. (8.4). The graph indicates that the disturbances propagate at angle of 40^0, which is the same result obtained using Navier-Stokes computations and by Mitchel, Lele and Moin (1997).

$$\Theta = -\frac{1}{M_o^2}\frac{\partial p}{\partial t} \tag{8.16}$$

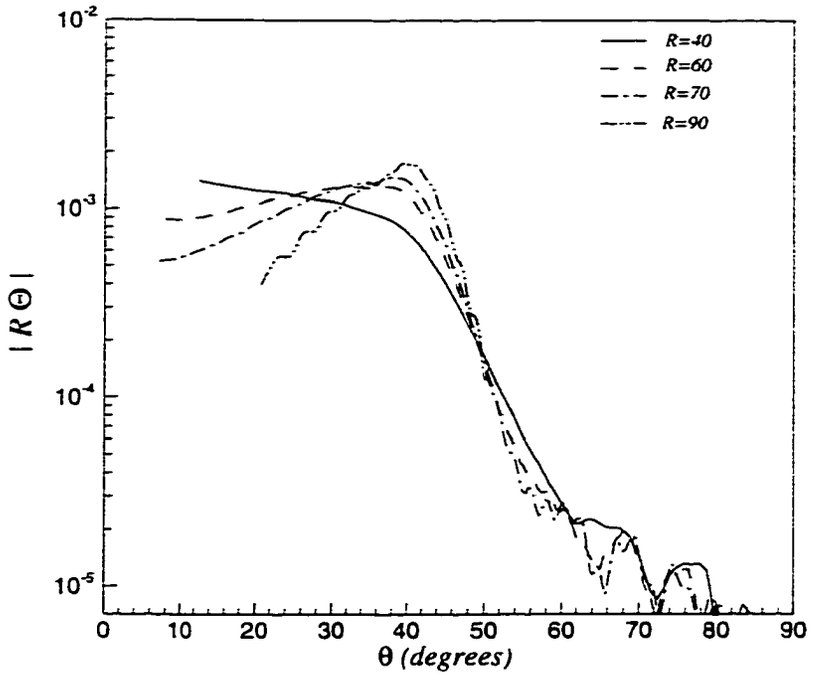

Figure (8.5) Variation of the far field dilatation Θ with the angle θ measured from the jet axis at a distance R (M_j=2.0)

The directivity pattern of the far field sound is presented in Fig. (8.5) in terms of the amplitude of the dilatation multiplied by the observer distance. The results are plotted at different distances from the sound source against the angle θ which is measured from the jet axis. The graph indicates that maximum dilatation amplitudes are obtained at approximately $\theta = 40^{o}$ for larger distances away from the sound source while maximum dilatation amplitude at R/r_j=40 is obtained near the jet axis. Similar results are obtained by Mitchel, Lele and Moin (1997).

8.5.2 Subsonic Jets

The far field computations of two different subsonic jets with different mach numbers are introduced in this section. The near field predictions of these jets using Navier-Stokes equations are shown in chapter 6. The first case is done for Mach number

0.6 and Reynolds number 2500. It is clear from Fig. (6.14) in chapter 6 that the sound source is located at 24 radius on the jet axis where maximum amplitude of the disturbance is reached. The pressure disturbances obtained from Navier-Stokes computations in the near field are stored at 10 radius in the radial direction for the far field calculations. The computational domain for the acoustic field computations is 55 radius in the axial direction and 70 radius in the radial direction with grid size of 500×500. The time step used for the solution of the linearized wave equation is 0.02.

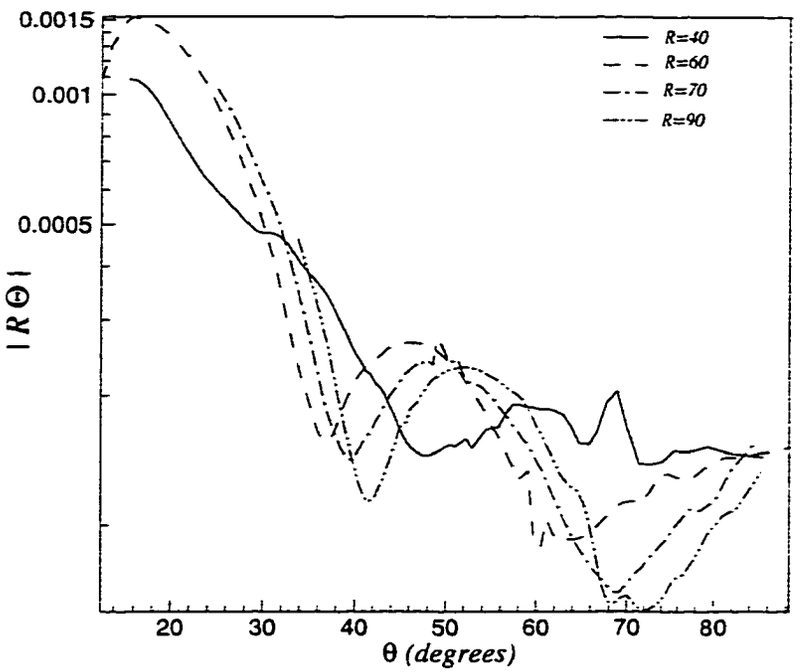

Figure (8.6) Variation of the far field dilatation Θ at the fundamental frequency with the angle θ measured from the jet axis at various distances R (M_j=0.6)

Subsonic jets develop nonlinearly in the near field and hence the sound radiation process is due to propagation of acoustic waves at different frequencies. The results presented in chapter 6 for subsonic jets show that the first subharmonic and the fundamental frequency have the highest disturbance amplitudes in the near field. In Figs. (8.6) and (8.7), the amplitudes of the dilatations multiplied by the observer distance are plotted against the angle θ measured from the jet axis. The dilatation amplitudes at the fundamental frequency for different distances from the sound source are presented in Fig.

(8.6). The graph indicates extinction angles between 64° and 72° at various locations in the far field, which is explained by Mitchel, Lele and Moin (1995) with the analogy to axisymmetric point quadrupoles.

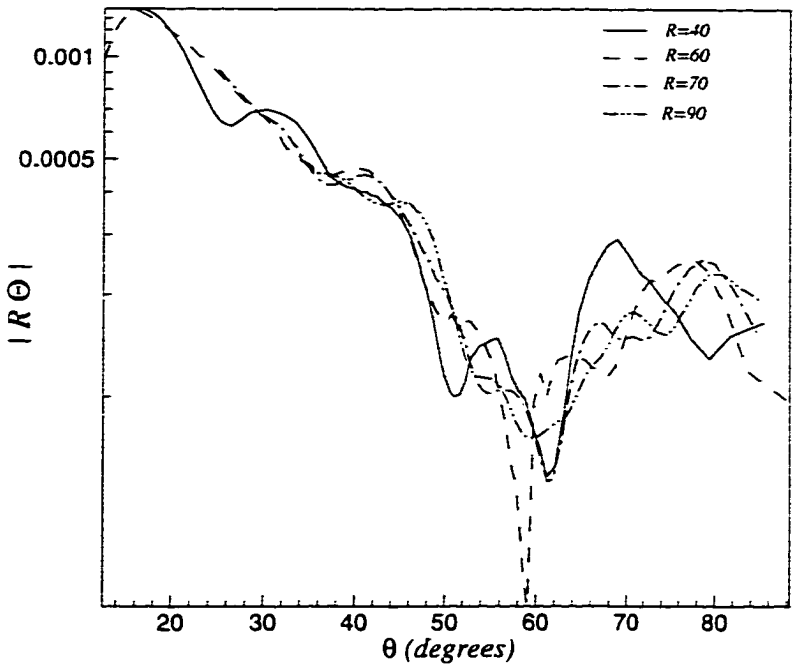

Figure (8.7) Variation of the far field dilatation Θ at the first subharmonic with the angle θ measured from the jet axis at various distances R (M_j=0.6)

The dilatation amplitudes at the first subharmonic are shown in Fig. (8.7) where the results indicate that the angles of extinction are in the range of 60° and 63° at various observer locations. Maximum dilatation amplitudes at different distances from the sound source are obtained near the jet axis or at shallow angles where the sound source has a preferred directivity.

The second case is done for higher Mach number (M_j=0.8) and the same Reynolds number (Re=2500). The results presented in chapter 6 for the variation of the disturbance amplitudes with the axial distance indicate that maximum disturbance amplitude is obtained at x/r_j=22 where the sound source is located. The pressure

disturbances obtained from Navier-Stokes computations in the near field are stored at 10 radius in the radial direction for the far field calculations. The computational domain for the acoustic field computations is 55 radius in the axial direction and 80 radius in the radial direction with grid size of 1000×500. The time step used for the solution of the linearized wave equation is 0.02.

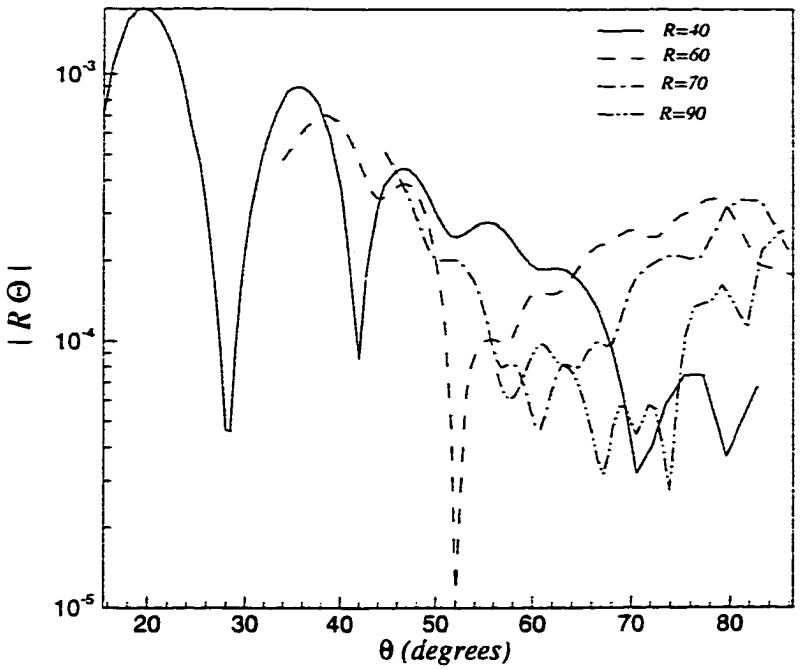

Figure (8.8) Variation of the far field dilatation Θ at the fundamental frequency with the angle θ measured from the jet axis at various distances R (M_j=0.8)

The far field directivity is presented in Fig. (8.8) in terms of the dilatation amplitude at the fundamental frequency. The angle of extinction varies with the observer location. As the distance measured from the source is increased, the extinction angle is increased which means that the jet noise is low at the forward arc for large distances. The jet shows preferred directivity at shallow angles.

The amplitudes of the dilatation at the first subharmonic have angles of extinction in the range of 55°-65° depending on the distance from the sound source as shown in Fig.

(8.9). Maximum amplitudes of the dilatation are obtained at shallow angles from the jet axis.

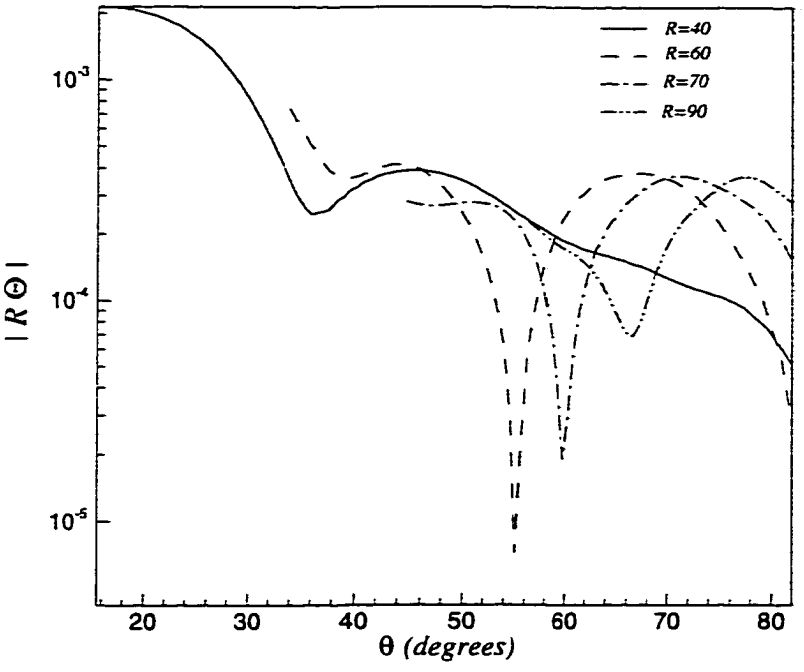

Figure (8.9) Variation of the far field dilatation Θ at the first subharmonic with the angle θ measured from the jet axis at various distances R (M_j=0.8)

8.6 Summary

A method is developed to compute jet noise in the far field using the linearized wave equation. Sixth-order compact finite difference scheme is used in the computations along with radiation boundary conditions. The sound source and its position are computed in chapter 6 using Navier-Stokes equations. The pressure disturbances from Navier-Stokes computations are submitted to the linearized wave equation at the interface as Dirchliet boundary conditions.

Noise is computed for supersonic and subsonic jets and the results agree with those obtained in chapter 6 using Navier-Stokes equations. In addition, the results are in good agreement with the results computed by Mitchel et al (1997) using Kirchhoff surface integral and the acoustic analogy. The results indicate that linearized Euler

equations or linearized wave equation can be used to compute jet noise in the far field after evaluating the sound source in the near field using Navier-Stokes equations. Computing the whole flow field using Navier-Stokes equations requires huge computational effort.

Chapter 9

Conclusions

9.1 Concluding Remarks and Discussion

The current research focuses on computing the far field noise radiated from the jet mixing layer. In addition, special method has been considered for estimating the sound source in the near field using the unsteady full Navier-Stokes equations. High order accurate numerical schemes are considered for the solution of the unsteady equations. Moreover, several kinds of boundary conditions are investigated in the current research.

In order to obtain the perturbation quantities, the jet mean flow is needed for the direct computation of the unsteady Navier-Stokes equations. In chapter 3, the jet mean flow calculation is discussed in detail. An accurate method is developed to estimate the jet mean flow using the boundary layer equations. The equations are solved using two-point fourth order accurate compact scheme. Additionally, the stability of the jet flow is analyzed using the linear stability theory. Two different stability methods are treated in the current research. The jet stability analysis is achieved using the global method, which provides an initial guess for the local stability method. The results of the global method are validated with those obtained by Khorrami (1991) and the results are in good agreement. Then, the most unstable frequency and its subharmonics, the eigenfunctions associated with these frequencies, the growth rate and the N-factor are computed using the local stability method. The results obtained from the local stability method are submitted to the direct simulation code at the inflow boundary for the evaluation of sound source.

To compute the unsteady flow quantities from Navier-Stokes equations, high order accurate numerical schemes are required. Explicit MacCormack schemes with operator splitting are adopted in the current research for the direct simulation of Navier-Stokes equations. Numerical schemes with different accuracy are investigated. One of the

well known finite difference schemes for computational aeroacoustics is the two-four scheme which is developed by Gottlieb and Turkel (1976). This scheme is fourth order accurate in space and second order in time. The accuracy of this scheme is increased in time and space by Hixon (1997). In addition, the dispersion error of the two-four scheme is minimized. Thus, new versions of the explicit MacCormack schemes such as two-six, four-four, four-six and the optimized dispersion relation-preserving scheme have been developed. A comparison between these schemes is carried out in the current research by applying these schemes for the simulation of supersonic jet. The results indicate that the two-four scheme has higher dispersion error than the new developed schemes. Moreover, the study shows that the dispersion relation-preserving scheme is the best among these schemes for less number of points per wavelength. Thus, an explicit MacCormack scheme with operator splitting, which is based on the finite difference of the original dispersion relation scheme developed by Tam and Webb (1992), is adopted in this work for the jet simulations.

Special treatments have been considered for the boundaries of the jet problem in order to ensure minimum wave reflection as the flow crosses the boundaries. Different types of boundary conditions are examined in the current research for the direct simulation of the unsteady Navier-Stokes equations. These boundary conditions include characteristic methods, buffer domain method and perfectly matching layer technique. A comparison between these boundary conditions and a reference solution is carried out and the results show that the perfectly matching layer technique has less reflection than the characteristic and buffer domain methods. In addition, the matching layer is not computationally expensive as the buffer domain method. Only few number of points are required in the matching layer while the sponge method and the buffer domain need very long computational domain.

Using the explicit MacCormack scheme and the matching layer technique at the boundaries, simulations of subsonic and supersonic jets are done with computational domain includes both the near field and in some cases the far field. The simulations are achieved for high and low Reynolds numbers. Additionally, jets with different Mach

numbers are computed. The computations of subsonic jets indicate that the sound source is characterized by the vortex pairing process which is the same result that is reported experimentally by Laufer and Yen (1983) and numerically by Colonius, Lele and Moin (1997). The dominant frequency for subsonic jets is the first subharmonic. Maximum disturbance amplitudes is obtained at the first subharmonic and the fundamental frequency, while other frequencies have small amplitudes. The location of the sound source on the jet axis is determined by the position of the disturbance saturation at the first subharmonic and it is found that most of the noise is radiated from this location. The directivity pattern in the far field of both subsonic and supersonic jets is computed using Navier-Stokes equations by extending the computational domain to the far field. The results obtained in the far field are in excellent agreement with those computed by Mitchel, Lele and Moin (1997).

In addition to the two dimensional axisymmetric jet simulations, three dimensional jet simulation for the near field computations is achieved using the same numerical scheme and characteristic boundary conditions. The computational domain is limited to a shorter distance because of the computational requirements for this simulation. The dominant modes, which generate the highest disturbance amplitudes, are predicted.

A numerical method is developed to compute the far field noise using the linearized wave equation. A sixth-order compact scheme is used to discretize the wave equation and radiation boundary conditions are employed at the boundaries. The results are compared with those obtained from the direct computations of Navier-Stokes equations for supersonic jet and the results are in good agreement. The directivity pattern of the far field noise radiated from subsonic jets is predicted using the wave equation. The sound radiated from subsonic jets in the far field is characterized by angles of extinction. Similar results are obtained using Lighthill's theory and Kirchohoff's surface by Mitchel, Lele and Moin (1995).

9.2 Recommendations for Future Work

For three dimensional axisymmetric jet simulations, the grid size near the jet centerline severely limits the time step and hence increases the computational time required for the simulation of subsonic jets where many grid are needed to calculate all the modes points in the azimuthal direction. Thus, a different numerical method in the angular direction is needed to avoid the stability limits at the centerline. One of these methods, which is used by Freund, Moin and Lele (1997), is the Fourier spectral method which uses the Fourier transform in the azimuthal direction to compute the derivatives. By using this method, the high wave numbers in the azimuthal direction are eliminated near the centerline. This method reduces the effective resolution in the azimuthal direction and greatly relaxes the time step restriction. Thus, it is recommended to improve the numerical schemes used in the current research for the three dimensional axisymmetric jet simulations by utilizing the Fourier spectral method in the azimuthal direction only.

In the current research, the noise radiated from only the jet mixing layer is computed. There is another source of noise emanated from imperfectly expanded jets. This noise is due to the interaction of shock waves in an incorrectly expanded supersonic jet with the turbulent mixing layer. Shock associated noise has two components, one consists of discrete tones which is the screech and the other is more broadband and often called broadband shock associated noise. The screech noise, which involves an acoustic feedback from the source region to the nozzle, is studied in some detail by Powell (1953). The source of the shock noise component is spatially coherent over an extended length of the jet and the quasi-periodicity of the shock cell structure plays a crucial role in the noise generation [Tam (1986)]. Although most of the jet noise is radiated from the mixing layer, it is recommended to investigate the role of shock wave-mixing layer interaction on the noise radiation.

An investigation of the broadband noise suppression is required in any future work. There are several methods used to suppress jet noise. One of these methods is introducing an annular coflow to eliminate the Mach wave emission. The effect of

coaxial jets on the noise emission is studied experimentally by Debiasi (1999) and Murkami (1998). It is found that using coflow reduces the near field screech peaks by 5-10 DB and the coflow suppressed the Mach wave emission effectively in jets by about 18 DB in the far field. It is recommended to investigate numerically the effect of coaxial jets on supersonic jet noise emission.

Moreover, the following issues need to be addressed in future work:

1) The physical process associated with shock waves/turbulence interaction mechanism.
2) The effect of jet temperature on broadband noise.
3) The effect of using coaxial jets on noise suppression.

Appendix A

Formulation of Boundary Layer Equations in Matrix Form

Rewriting the boundary-layer Eqs. (3.24)-(3.26), in the following form:

$$\overset{\circ}{\psi} = f(\psi, r) \tag{A.1}$$

Let $G(\psi, \overset{\circ}{\psi}) = \overset{\circ}{\psi} - f(\psi, r) = 0$ (A.2)

Using Taylor series expansion, the function G can be written as

$$G(\psi, \overset{\circ}{\psi}) = G(\psi, \overset{\circ}{\psi})_i + (\frac{\partial G}{\partial \psi})_i \Delta\psi + (\frac{\partial G}{\partial \overset{\circ}{\psi}})_i \Delta\overset{\circ}{\psi} \tag{A.3}$$

where the subscript i denotes the initial guess

Rearranging Eq. (A.3) and using Eq. (A.1), yields

$$\Delta\overset{\circ}{\psi} = [f(\psi, r) - \overset{\circ}{\psi}]_i + (\frac{df}{d\psi})_i \Delta\psi \tag{A.4}$$

Eq. (A.4) may be expressed in the following matrix form

$$\Delta\overset{\circ}{\psi} = F + D\,\Delta\psi \tag{A.5}$$

Where the nonzero elements of the matrices D and F are:

$$D(1,2) = 1$$

$$D(2,1) = \frac{1}{\mu T}(a_1 U_2 + a_2 U_1 + a_3 U) + \frac{a_3 U}{\mu T}$$

$$D(2,2) = -\frac{1}{r} - \frac{1}{\mu}\frac{d\mu}{dT}\frac{\partial T}{\partial r} + \frac{V}{T}\frac{1}{\mu}$$

$$D(2,3) = \frac{1}{\mu}\frac{1}{T}\frac{\partial U}{\partial r}$$

$$D(2,4) = -\frac{\partial U}{\partial r}[\frac{-1}{\mu^2}(\frac{d\mu}{dT})^2 + \frac{1}{\mu}\frac{d^2\mu}{dT^2}]\frac{\partial T}{\partial r} - \frac{U}{T^2}\frac{1}{\mu}(a_1U_2 + a_2U_1 + a_3U)$$

$$-\frac{U}{T}\frac{1}{\mu^2}\frac{d\mu}{dT}(a_1U_2 + a_2U_1 + a_3U) - V\frac{\partial U}{\partial r}[\frac{1}{T^2}\frac{1}{\mu} + \frac{1}{T}\frac{1}{\mu^2}\frac{d\mu}{dT}]$$

$$D(2,5) = -\frac{1}{\mu}\frac{d\mu}{dT}\frac{\partial U}{\partial r}$$

$$D(3,1) = -a_3 + \frac{1}{T}(a_1T_2 + a_2T_1 + a_3T)$$

$$D(3,3) = -\frac{1}{r} - \frac{1}{T}\frac{\partial T}{\partial r}$$

$$D(3,4) = -\frac{V}{T^2}\frac{\partial T}{\partial r} + \frac{U}{T}a_3 - \frac{U}{T^2}(a_1T_2 + a_2T_1 + a_3T)$$

$$D(3,5) = \frac{V}{T}$$

$$D(4,5) = 1$$

$$D(5,1) = \frac{1}{T}\frac{\mathrm{Pr}}{\mu}(a_1T_2 + a_2T_1 + a_3T)$$

$$D(5,2) = -2\,\mathrm{Pr}\,(\gamma - 1)M^2\frac{\partial U}{\partial r}$$

$$D(5,3) = \frac{\mathrm{Pr}}{\mu}\frac{1}{\mathrm{T}}\frac{\partial T}{\partial r}$$

$$D(5,4) = -\frac{\mathrm{Pr}}{\mu}\frac{U}{T^2}(a_1T_2 + a_2T_1 + a_3T) - (\frac{\partial T}{\partial r})^2[\frac{1}{\mu^2}(\frac{d\mu}{dT})^2 + \frac{1}{\mu}\frac{d^2\mu}{dT^2}]$$

$$-\frac{U}{T}(a_1T_2 + a_2T_1 + a_3T)\frac{\mathrm{Pr}}{\mu^2}\frac{d\mu}{dT} - V\frac{\partial T}{\partial r}[\frac{1}{T^2}\frac{\mathrm{Pr}}{\mu} + \frac{1}{T}\frac{\mathrm{Pr}}{\mu^2}\frac{d\mu}{dT}]$$

$$D(5,5) = -2\frac{\partial T}{\partial r}\frac{1}{\mu}\frac{d\mu}{dT} - \frac{1}{r} + \frac{\mathrm{Pr}}{\mu}\frac{V}{\mathrm{T}}$$

$$F(2) = -\frac{\partial^2 U}{\partial r^2} + -\frac{1}{r}\frac{\partial U}{\partial r} - \frac{1}{\mu}\frac{d\mu}{dT}\frac{dT}{dr}\frac{\partial U}{\partial r} + \frac{U}{\mu T}(a_1U_2 + a_2U_1 + a_3U) + \frac{V}{\mu T}\frac{\partial U}{\partial r}$$

$$F(3) = -\frac{\partial V}{\partial r} + \frac{V}{r} + (a_1 U_2 + a_2 U_1 + a_3 U) - \frac{U}{T}(a_1 T_2 + a_2 T_1 + a_3 T) - \frac{V}{T}\frac{\partial T}{\partial r}$$

$$F(5) = -\frac{\partial^2 T}{\partial r^2} + -\frac{1}{r}\frac{\partial T}{\partial r} + \frac{\mathrm{Pr}}{\mu}\frac{U}{T}(a_1 T_2 + a_2 T_1 + a_3 T) + \frac{\mathrm{Pr}}{\mu}\frac{V}{T}\frac{\partial T}{\partial r} - \frac{1}{\mu}(\frac{\partial T}{\partial r})^2 \frac{d\mu}{dT}$$

$$-\mathrm{Pr}(\gamma - 1)M^2(\frac{\partial U}{\partial r})^2$$

Appendix B

Linear Stability Equations

Continuity:

$$\frac{dF}{dr}+\left[\frac{1}{\pi}\frac{d\pi}{dr}-\frac{1}{\eta}\frac{d\eta}{dr}+\frac{1}{r}\right]F+\left[\frac{in}{r}\right]G+[i\alpha]H+\left[\frac{U}{\pi}\right]\frac{dP}{dr}$$
$$+\left[\frac{inV}{r\pi}-\frac{U}{\pi\eta}\frac{d\eta}{dr}+\frac{1}{\pi}\left(\frac{dU}{dr}+\frac{U}{r}\right)+\frac{i\alpha W}{\pi}-\frac{i\omega}{\pi}\right]P-\left[\frac{U}{\eta}\right]\frac{dT}{dr} \qquad \text{(B.1)}$$
$$+\left[\frac{2U}{\eta^2}\frac{d\eta}{dr}-\frac{U}{\pi\eta}\frac{d\pi}{dr}-\frac{inV}{r\eta}-\frac{1}{\eta}\left(\frac{dU}{dr}+\frac{U}{r}\right)-\frac{i\alpha W}{\eta}+\frac{i\omega}{\eta}\right]T=0$$

r-momentum:

$$\left[2+\frac{\lambda}{\mu}\right]\frac{d^2F}{dr^2}+\left[-\frac{\mathrm{Re}\,\rho U}{\mu}+\frac{1}{\mu}\frac{d\eta}{dr}\left(2\frac{d\mu}{d\eta}+\frac{d\lambda}{d\eta}\right)\right.$$
$$+\frac{1}{r}\left((2+\frac{\lambda}{\mu})\right]\frac{dF}{dr}+\left[\frac{i\omega\,\mathrm{Re}\,\rho}{\mu}-\frac{\mathrm{Re}\,\rho}{\mu}\frac{dU}{dr}-\frac{in\,\mathrm{Re}\,\rho V}{\mu r}\right.$$
$$\left.-\frac{i\alpha\,\mathrm{Re}\,\rho W}{\mu}+\frac{1}{\mu r}\frac{d\lambda}{d\eta}\frac{d\eta}{dr}-\frac{1}{r^2}\left(2+\frac{\lambda}{\mu}\right)-\frac{n^2}{r^2}-\alpha^2\right]F$$
$$+\left[\frac{in}{r}\left(1+\frac{\lambda}{\mu}\right)\right]\frac{dG}{dr}+\left[\frac{2\,\mathrm{Re}\,\rho V}{\mu r}+\frac{in}{\mu r}\frac{d\lambda}{d\eta}\frac{d\eta}{dr}\right.$$
$$\left.-\frac{in}{r^2}\left(3+\frac{\lambda}{\mu}\right)\right]G+\left[i\alpha\left(1+\frac{\lambda}{\mu}\right)\right]\frac{dH}{dr}+\left[\frac{i\alpha}{\mu}\frac{d\lambda}{d\eta}\frac{d\eta}{dr}\right]H$$
$$-\left[\frac{Re}{\mu}\right]\frac{dP}{dr}-\left[\frac{Re\,\rho}{\mu\pi}\left(U\frac{dU}{dr}-\frac{V^2}{r}\right)\right]P+\left[\frac{2}{\mu}\frac{d\mu}{d\eta}\frac{dU}{dr}+\frac{1}{\mu}\frac{d\lambda}{d\eta}\left(\frac{dU}{dr}+\frac{U}{r}\right)\right]\frac{dT}{dr} \qquad \text{(B.2)}$$
$$+\left[\frac{2}{\mu}\frac{d^2\mu}{d\eta^2}\frac{d\eta}{dr}\frac{dU}{dr}\right.$$

$$\frac{2}{\mu}\frac{d\mu}{d\eta}\frac{d^2U}{dr^2}+\frac{1}{\mu}\frac{d^2\lambda}{d\eta^2}\frac{d\eta}{dr}\left(\frac{dU}{dr}+\frac{U}{r}\right)+\frac{1}{\mu}\frac{d\lambda}{d\eta}\left(\frac{d^2U}{dr^2}-\frac{U}{r^2}\right.$$

$$\left.+\frac{1}{r}\frac{dU}{dr}\right)+\frac{in}{\mu}\frac{d\mu}{d\eta}\left(\frac{1}{r}\frac{dV}{dr}-\frac{V}{r^2}\right)+\frac{\mathrm{Re}\,\rho}{\mu\eta}\left(U\frac{dU}{dr}-\frac{V^2}{r}\right)$$

$$\left.+\frac{i\alpha}{\mu}\frac{d\mu}{d\eta}\frac{dW}{dr}+\frac{2}{\mu}\frac{d\mu}{d\eta}\left(\frac{1}{r}\frac{dU}{dr}-\frac{U}{r^2}\right)\right]T=0$$

6 - momentum:

$$\left[\frac{in}{r}\left(1+\frac{\lambda}{\mu}\right)\right]\frac{dF}{dr}+\left[\frac{in}{r^2}\left(3+\frac{\lambda}{\mu}\right)-\frac{\mathrm{Re}\,\rho}{\mu}\frac{dV}{dr}-\frac{\mathrm{Re}\,\rho V}{\mu r}+\frac{in}{r}\frac{1}{\mu}\frac{d\mu}{d\eta}\frac{d\eta}{dr}\right]F+\frac{d^2G}{dr^2}$$

$$+\left[\frac{1}{\mu}\frac{d\mu}{d\eta}\frac{d\eta}{dr}-\frac{\mathrm{Re}\,\rho U}{\mu}+\frac{1}{r}\right]\frac{dG}{dr}+\left[\frac{i\omega\,\mathrm{Re}\,\rho}{\mu}-\frac{in\,\mathrm{Re}\,\rho V}{\mu r}-\frac{i\alpha\,\mathrm{Re}\,\rho W}{\mu}-\frac{\mathrm{Re}\,\rho U}{\mu r}\right.$$

$$\left.-\frac{n^2}{r^2}\left(2+\frac{\lambda}{\mu}\right)-\alpha^2-\frac{1}{r}\frac{1}{\mu}\frac{d\mu}{d\eta}\frac{d\eta}{dr}-\frac{1}{r^2}\right]G$$

$$-\left[\frac{an}{r}\left(1+\frac{\lambda}{\mu}\right)\right]H-\left[\frac{in\,Re}{\mu r}+\frac{Re\,\rho}{\mu\pi}\left(U\frac{dV}{dr}+\frac{UV}{r}\right)\right]P$$

$$+\left[\frac{1}{\mu}\frac{d\mu}{d\eta}\left(\frac{dV}{dr}-\frac{V}{r}\right)\right]\frac{dT}{dr}+\left[\frac{Re\,\rho}{\mu\eta}\left(U\frac{dV}{dr}+\frac{UV}{r}\right)\right.$$

$$+\frac{2inU}{r^2}\frac{1}{\mu}\frac{d\mu}{d\eta}+\frac{in}{\mu}\frac{d\lambda}{d\eta}\left(\frac{1}{r}\frac{dU}{dr}+\frac{U}{r^2}\right)+\frac{1}{\mu}\frac{d^2\mu}{d\eta^2}\frac{d\eta}{dr}\left(\frac{dV}{dr}\right. \qquad \text{(B.3)}$$

$$\left.\left.-\frac{V}{r}\right)+\frac{1}{\mu}\frac{d\mu}{d\eta}\left(\frac{d^2V}{dr^2}+\frac{V}{r^2}-\frac{1}{r}\frac{dV}{dr}\right)+\frac{2}{r\mu}\frac{d\mu}{d\eta}\left(\frac{dV}{dr}-\frac{V}{r}\right)\right]T=0$$

x-momentum:

$$\left[i\alpha\left(1+\frac{\lambda}{\mu}\right)\right]\frac{dF}{dr}+\left[\frac{i\alpha}{r}\left(1+\frac{\lambda}{\mu}\right)-\frac{\mathrm{Re}\,\rho}{\mu}\frac{dW}{dr}\right.$$

$$\left.+\frac{i\alpha}{\mu}\frac{d\mu}{d\eta}\frac{d\eta}{dr}\right]F-\left[\frac{\alpha n}{r}\left(1+\frac{\lambda}{\mu}\right)\right]G+\frac{d^2H}{dr^2}+\left[-\frac{\mathrm{Re}\,\rho U}{\mu}\right.$$

$$\left.+\frac{1}{\mu}\frac{d\mu}{d\eta}\frac{d\eta}{dr}+\frac{1}{r}\right]\frac{dH}{dr}+\left[\frac{i\omega\,\mathrm{Re}\,\rho}{\mu}-\frac{in\,\mathrm{Re}\,\rho V}{\mu r}-\frac{i\alpha\,\mathrm{Re}\,\rho W}{\mu}\right.$$

$$-\alpha^2\left(2+\frac{\lambda}{\mu}\right)-\frac{n^2}{r^2}\Bigg]H-\left[\frac{Re\,\rho U}{\mu\pi}\frac{dW}{dr}+\frac{i\alpha Re}{\mu}\right]P$$

$$+\left[\frac{1}{\mu}\frac{d\mu}{d\eta}\frac{dW}{dr}\right]\frac{dT}{dr}+\left[\frac{Re\,\rho U}{\mu\eta}\frac{dW}{dr}+\frac{i\alpha}{\mu}\frac{d\lambda}{d\eta}\left(\frac{dU}{dr}+\frac{U}{r}\right)\right. \tag{B.4}$$

$$\left.+\frac{1}{\mu}\frac{d\mu}{d\eta}\left(\frac{d^2W}{dr^2}+\frac{1}{r}\frac{dW}{dr}\right)+\frac{1}{\mu}\frac{d^2\mu}{d\eta^2}\frac{d\eta}{dr}\frac{dW}{dr}\right]T=0$$

Energy-Equation:

$$\left[2(\gamma-1)M^2\,Pr\left\{\frac{2\mu}{\kappa}\frac{dU}{dr}+\frac{\lambda}{\kappa}\left(\frac{dU}{dr}+\frac{U}{r}\right)\right\}\right]\frac{dF}{dr}$$

$$+\left[-\frac{Pr\,Re\,\rho}{\kappa}\frac{d\eta}{dr}+(\gamma-1)M^2\,Pr\left\{\frac{Re}{\kappa}\frac{d\pi}{dr}+\frac{4\mu}{\kappa}\frac{U}{r^2}\right.\right.$$

$$\left.\left.+i2\alpha\frac{\mu}{\kappa}\frac{dW}{dr}+\frac{i2n\mu}{r\kappa}\left(\frac{dV}{dr}-\frac{V}{r}\right)+\frac{2}{r}\frac{\lambda}{\kappa}\left(\frac{dU}{dr}+\frac{U}{r}\right)\right\}\right]F$$

$$+\left[2(\gamma-1)M^2\,\mathrm{Pr}\frac{\mu}{\kappa}\left(\frac{dV}{dr}-\frac{V}{r}\right)\right]\frac{dG}{dr}$$

$$+\left[\frac{2(\gamma-1)M^2\,\mathrm{Pr}}{r}\left\{\frac{i2n\mu U}{r\kappa}+\frac{in\lambda}{\kappa}\left(\frac{dU}{dr}+\frac{U}{r}\right)\right.\right.$$

$$\left.\left.-\frac{\mu}{\kappa}\left(\frac{dV}{dr}-\frac{V}{r}\right)\right\}\right]G+\left[2(\gamma-1)M^2\,\mathrm{Pr}\frac{\mu}{\kappa}\frac{dW}{dr}\right]\frac{dH}{dr}$$

$$+\left[i2\alpha(\gamma-1)M^2\,Pr\frac{\lambda}{\kappa}\left(\frac{dU}{dr}+\frac{U}{r}\right)\right]H$$

$$+\left[\frac{(\gamma-1)M^2\,Pr\,Re}{\kappa}U\right]\frac{dP}{dr}+\left[-\frac{Pr\,Re\,\rho U}{\kappa\pi}\frac{d\eta}{dr}\right.$$

$$\left.+\frac{i(\gamma-1)M^2\,Pr\,Re}{\kappa}\left(-\omega+\frac{nV}{r}+\alpha W\right)\right]P+\frac{d^2T}{dr^2}$$

$$+\left[-\frac{\mathrm{Pr}\,\mathrm{Re}\,\rho U}{\kappa}+\frac{2}{\kappa}\frac{d\kappa}{d\eta}\frac{d\eta}{dr}+\frac{1}{r}\right]\frac{dT}{dr}+\left[\frac{i\,\mathrm{Pr}\,\mathrm{Re}\,\rho}{\kappa}(\omega\right.$$

$$-\frac{nV}{r}-\alpha W)+\frac{\mathrm{Pr}\,\mathrm{Re}\,\rho U}{\kappa\eta}\frac{d\eta}{dr}+\frac{1}{\kappa}\frac{d^2\kappa}{d\eta^2}\left(\frac{d\eta}{dr}\right)^2-\frac{n^2}{r^2}$$

$$-\alpha^2+\frac{1}{\kappa}\frac{d\kappa}{d\eta}\left(\frac{d^2\eta}{dr^2}+\frac{1}{r}\frac{d\eta}{dr}\right)+(\gamma-1)M^2\,\mathrm{Pr}\frac{1}{\kappa}\frac{d\mu}{d\eta}\left(\frac{dW}{dr}\right)^2$$

$$+\frac{2(\gamma-1)M^2\,\mathrm{Pr}}{\kappa}\frac{d\mu}{d\eta}\left\{\left(\frac{dU}{dr}\right)^2+\frac{U^2}{r^2}\right\}$$

$$+\frac{(\gamma-1)M^2\,\mathrm{Pr}}{\kappa}\frac{d\mu}{d\eta}\left\{\left(\frac{dV}{dr}-\frac{V}{r}\right)^2\right\} \qquad \text{(B.5)}$$

$$\left.+\frac{(\gamma-1)M^2\,\mathrm{Pr}}{\kappa}\frac{d\lambda}{d\eta}\left\{\left(\frac{dU}{dr}+\frac{U}{r}\right)^2\right\}\right]T=0$$

BIBLIOGRAPHY

1. Atkins, H. and Casper, J., 1994 "Nonreflecting boundary conditions for high-order methods" *AIAA journal*, Vol. 32, No. 3, pp. 512-518.
2. Balakumar, P., 1998 "Prediction of supersonic jet noise" *AIAA paper* 98-1057
3. Bayliss, A. and Turkel, E., 1980 "Radiation boundary conditions for wave-like equations" *Communications on Pure and Applied Mathematics*, Vol. 33, pp. 708-725.
4. Bayliss, A. and Turkel, E., 1982 "Far field boundary conditions for compressible flows" *Journal of Computational Physics*, Vol. 48, pp. 182-199.
5. Bayliss, A., Maestrello, L., Parikh, P., and Turkel, E., 1985 "A Fourth Order Scheme for the Unsteady Compressible Navier-Stokes Equations" *AIAA paper* 85-1694.
6. Bayliss, A. and Maestrello, L., 1997 " Response of high subsonic jet to nonaxisymmetric disturbances" *AIAA* 97-1580.
7. Berenger, J-P, 1994 "A perfectly matched layer for the absorption of electromagnetic waves" *Journal of Computational Physics*, Vol. 114, pp. 185-200.
8. Berenger, J-P, 1996 "Three-dimensional perfectly matched layer for the absorption of electromagnetic waves" *Journal of Computational Physics*, Vol. 127, pp. 363-379.
9. Bridges, J. and Hussain, F., 1992 "Direct evaluation of aeroacoustic theory in a jet" *Journal of Fluid Mechanics*, Vol. 240, pp. 469-501.
10. Colonius, T., Lele, S. K. and Moin, P., 1993 "Boundary conditions for direct computation of aerodynamic sound generation" *AIAA Journal*, Vol. 31, No. 9, pp. 1574-1582.
11. Colonius, T., Sanjiva, K.L., Parviz, M., 1997 "Sound generation in a mixing layer" *Journal of Fluid Mechanics*, Vol.330, pp. 375-409.
12. Crighton, D. G. and Huerre, P., 1990 "Shear-layer pressure fluctuations and superdirective acoustic source" *Journal of Fluid Mechanics*, Vol. 220, pp. 355-368.
13. Crow, S. C. and Champagne, F.H., 1971 "Orderly structure in jet turbulence" *Journal of Fluid Mechanics*, Vol. 48, pp. 547-591.
14. Damkevala, R.J., Grosche, F.R. and Guest, S.H., 1973 "Direct measurement of sound sources in airjets using the crossed beam correlation technique" *AGARD-CP*-131.
15. Debiasi, M. and Papamoschou, D., 1999 "Acoustics of Under-and Over-Expanded Coaxial Jets" *AIAA 99-0081*.
16. Dong, T. Z., 1996 " A set of simple radiation boundary conditions for acoustic computations in non-uniform mean flows" *AIAA* 96-0274.
17. Enquist, B. and Majda, A., 1977 " Absorbing boundary conditions for the numerical simulation of waves" *Mathematics of Computation*, Vol. 31, No. 139, pp. 629-651.
18. Enquist, B. and Majda, A., 1979 " Radiation boundary conditions for acoustic and elastic wave calculations" *Communications on Pure and Applied Mathematics*, Vol. 32 (3), pp. 708-725.
19. Farouk, B., Oran, E.S., and Kailasanath, K. 1991, "Numerical Simulation of the structure of supersonic shear layers", *Physics of Fluids*, Vol. 3, pp. 2786-2798.
20. Freund, J.B., Moin, P. and Lele, S.K., 1997 " Compressibility effects in a turbulent annual mixing layer" *Stanford University Report No. TF-72*.
21. Freund, J.B., Lele, S.K., and Moin, P., 1998 " Direct simulation of a Mach 1.92 jet and its sound field" *AIAA/CEAS* 98-2291

22. Giles, M.B., 1990 " Nonreflecting boundary conditions for Euler equation calculations" *AIAA Journal*, Vol. 28, No. 12, pp. 2050-2058.
23. Givoli, D., 1991 " Non-reflecting boundary conditions" " *Journal of Computational Physics*, Vol. 94, pp. 1-29, 1991.
24. Goldstien, M. E., 1976 "Aeroacoustics" McGraw-Hill.
25. Goldstien, M. E., 1984 "Aeroacoustics of turbulent shear flows" *Ann. Rev. Fluid Mech.*, Vol. 16, pp. 263-285.
26. Gottlieb, D. and Turkel, E., 1976 'Dissipative two-four method for time dependent problems', *Mathematics of computations*, Vol. 30, No. 136, pp. 703-723.
27. Griffin, M .D., Jones, E. and Anderson, J. D., 1979 "A computational fluid dynamic technique valid at the centerline for non-axisymmetric problems in cylindrical coordinates" *Journal of Computational Physics*, Vol. 30, pp. 352-360,1979.
28. Grosche, F.R., 1973 "Distributions of sound source intensities in subsonic and supersonic jets" *AGARD-CP*-131.
29. Hagstrom, T. and Hariharan, S. I., 1988 " Accurate boundary conditions for exterior problems in gas dynamics" *Math. Computation*, Vol.51, pp. 581-597.
30. Harper-Bourne, M. and Fisher, M.J., 1973 "The noise from shock waves in supersonic jets" *AGARD-CP*-131.
31. Hayder, M.E., Turkel, E., and Mankbadi, R.R., 1993 " Numerical simulation of a high Mach number jet" *AIAA* 93-0653
32. Hayder, M. E. and Turkel, E., 1995 "Nonreflecting boundary conditions for jet flow computations" *AIAA Journal*, Vol. 33, No. 12, pp. 2264-2270.
33. Hayder, M. E., 1996 "On buffer layers as non-reflecting computational boundaries" *AIAA* 96-0273.
34. Hayder, M. E., Hu, F.Q. and Hussaini, M.Y., 1997 "Towards perfectly absorbing boundary conditions for Euler equations" *ICASE report* No. 97-25.
35. Hedstrom, G. W., 1979 "Nonreflecting boundary conditions for nonlinear hyberbolic systems" *Journal of Computational Physics,* Vol. 30, pp. 222-237.
36. Hixon, R. and Shih, S. H., 1995a "Effect of input disturbance on linearized Euler equation prediction of jet noise" *AIAA* 95-0752.
37. Hixon, R., Shih, S. H. and Mankbadi, R. R., 1995b "Evaluation of boundary conditions for computational aeroacoustics" *AIAA Journal*, Vol. 33, No. 11, pp. 2006-2012.
38. Hixon, R., 1997 "On increasing the accuracy of McCormack schemes for aeroacoustic applications" *AIAA* 97-1586-CP.
39. Hixon, R. and Turkel, E., 1998 "High-accuracy compact McCormack-type schemes for computational aeroacoustics" *AIAA* 98-0365.
40. Ho, C. M and Huang, L. S, 1982 "Subharmonics and vortex merging in mixing layers" *Journal of Fluid Mechanics*, Vol. 119, pp. 443-473.
41. Hu, F.Q., 1995 "On absorbing boundary conditions for linearized Euler equations by a perfectly matching layer" *ICASE Report* 95-70.
42. Hu, F.Q., 1996 "On absorbing boundary conditions for linearized Euler equations by a perfectly matching layer" *Journal of Computational Physics*, Vol. 129, pp. 201-219.
43. Hurre, P. and Crighton, D. G., 1983 "Sound generated by instability waves in a low Mach number jet" *AIAA paper* 83-0661.

44. Joslin, R.D, Street, C.L., and Chang, C.L., 1992 " Validation of three-dimensional incompressible spatial direct numerical simulation code" *NASA technical paper* 3205.
45. Khorami, M.R., 1991 " Stability of a compressible swirling jet" *AIAA* 91-1770.
46. Kibens, V., 1980 "Discrete noise spectrum generated by an acoustically excited jet" AIAA Journal, Vol. 18, No. 4, pp. 434-441.
47. Laufer, J., Kaplan, R.E. and Chu, W.T., 1973 "On the generation of jet noise" *AGARD-CP*-131.
48. Laufer, J. and Yen, T-C., 1983 "Noise generation by a low-Mach-number jet" *Journal of Fluid Mechanics*, Vol. 134, pp.1-31.
49. Laurence, J. C., 1956 "Intensity scale and spectra of turbulence in mixing region of free subsonic jet" *NACA Rep.* No. 1292.
50. Lele, S. K., 1989 "Direct numerical simulation of compressible free shear flows" *AIAA* 89-0374.
51. Lele, S. K., 1992 "Compact finite difference schemes with spectral like resolution" *Journal of Computational Physics*, Vol. 103, pp. 16-42.
52. Lighthill, M. J., 1952 "On sound generated aerodynamically: I.-General theory" *Proc. R. Soc. London A* 211, pp. 554-587.
53. Lighthill, M. J., 1954 "On sound generated aerodynamically: II.-Turbulence as a source of sound" *Proc. R. Soc. London A* 222, pp. 1-32.
54. Lighthill, M. J., 1992 "Report on the final panel discussion on computational aeroacoustics" *ICASE Rep.* 92-53.
55. Lilley, G. M., 1974 "On the noise from jets" *AGARD CP*-131.
56. Malik, M. R., Chuang, S. and Hussaini, M. Y., 1982 "Accurate numerical solution of compressible, linear stability equations" *ZAMP*, Vol.33, No.2, pp. 189-201.
57. Malik, M. R., 1990 "Numerical methods for hybersonic boundary layer stability" *Journal of Computational Physics*, Vol. 86, No.2, pp. 376-412.
58. Mankbadi, R. R. and Liu, J. T. C, 1984 "Sound generated aerodynamically revisited: Large scale structures in a turbulent jet as a source of sound" *Phil Trans R. Soc. Lond. A* 311, pp. 183-217.
59. Mankbadi, R. R., 1990 "The self-noise from ordered structures in a low Mach number jet" *Journal of Applied Mechanics*, Vol. 57, pp. 241-246.
60. Mankbadi, R. R., 1992 "Dynamics and control of coherent structures in turbulent jets" *Appl. Mech. Review*, Vol. 45, pp. 219-248.
61. Mankbadi, R.R, Hayder, M.E, and Povinelli, L.A, 1994 " Structure of supersonic jet flow and its radiated sound" *AIAA Journal*, Vol. 32, No. 5, pp. 897-906.
62. Massier, P. F., Parthasarathy, S. P. and Cuffel, R. F., 1973 "Experimental evaluation of fluctuating density and radiated noise from a high-temperature jet" *AGARD-CP*-131.
63. Meecham, W.C. and Hurdle, P.M., 1973 "Use of cross-correlation measurements to investigate noise generating regions of a real jet engine and a model jet" " *AGARD-CP*-131.
64. Mitchel, B. E., Lele, S. K. and Moin, P., 1995 "Direct computation of the sound generated by vortex pairing in an axisymmetric jet" *AIAA* 95-0504.
65. Mitchel, B. E., Lele, S. K. and Moin, P., 1997 "The direct computation of Mach wave radiation in an axisymmetric supersonic jet" *AIAA Journal*, Vol. 35, pp. 1574-1580.

66. Mitchel, B. E., Lele, S. K. and Moin, P., 1999 "Direct computation of the sound generated by vortex pairing in an axisymmetric jet" *Journal of Fluid Mechanics*, Vol. 383, pp. 113-142.
67. Papamoschou, D., 1997 "Mach wave elimination in supersonic jets" *AIAA Journal*, Vol. 35, No. 10, pp. 1604-1611.
68. Poinsot, T. J. and Lele, S. K., 1992 "Boundary conditions for direct simulations of compressible viscous flows" *Journal of Computational Physics*, Vol. 101, pp. 104-129.
69. Pruett, C. D., Chang, C-L, 1993 "A comparison of PSE and DNS for high speed boundary-layer flows" *Symposium of the ASME Fluids Engineering Division*, Summer Meeting, Washington, D.C.
70. Ragab, S.A. and Sheen, S., 1991 "The Nonlinear Development of Supersonic Instability Waves in a Mixing Layer", *Phiscs of Fluids*, Vol. 4, pp. 553-566.
71. Rai, M. M., Gatski, T. B. and Erlebacher, G., 1995 "Direct simulation of spatially eVolving compressible turbulent boundary layers" *AIAA* 95-0583.
72. Ribner, L. S., 1995 "An extension of the Lighthill theory of jet noise to encompass refraction and shielding" *NASA Technical Memorandum* 110163.
73. Roe, P. L., 1989 "Remote Boundary conditions for unsteady multidimensional aerodynamic computations" *Computer and Fluids Journal*, Vol. 17, No. 1, pp.221-231.
74. Rudy, D. and Strikwerda, J. C., 1980 "Nonreflecting outflow boundary condition for subsonic Navier-stokes calculations" *Journal of Computational Physics*, Vol. 36, pp. 55-70.
75. Sankar, L. N., Reddy, N. N., and Hiriharan, N., 1993 "A comparative study of numerical schemes for aeroacoustic applications" *FED-VOL. 147, Computational aeroacoustics Aero- and Hydro-Acoustics, ASME*, pp. 35-40.
76. Sarkar, S. and Hussaini, M. Y., 1993 "Computations of the sound generated by isotropic turbulence" *ICASE Rep* 93-74.
77. Scott, J.N., 1992 "Acoustic analysis using numerical solutions of the Navier-Stokes equations" *AIAA* 92-0506.
78. Scott, J.N., 1993 "Accuracy consideration in the computational analysis of jet noise" *AIAA* 93-0146.
79. Scott, J.N, 1994 "A comparison of numerical and experimental results for unsteady flow associated with jet noise" *AIAA* 94-0459.
80. Seiner, J. M. and Gilinsky, M. M., 1997 "Nozzle thrust optimization while reducing jet noise" *AIAA Journal*, Vol. 35, No. 3, pp. 420-427.
81. Shih, S. H. and Hixon, D. R., 1995 "A zonal approach for prediction of jet noise" *CEAS/AIAA*-95-144.
82. Shih, S. H. and Hixon, R. and Mankbadi, R.R., 1995 "Three dimensional structure in a supersonic jet: behavior near centerline" *AIAA* 95-0508.
83. Shih, S.H. and Hixon, D.R., 1996 " prediction of flow and acoustic fields of a supersonic jet" *AIAA* 96-0751
84. Soh, W. Y., 1994 "Unsteady jet flow computation towards noise prediction" *AIAA* 94-0138.
85. Street, C. L. and Macaraeg, M. G., 1989 "Spectral multi-domain for large-scale fluid dynamics simulations" *Int. Journal Appl. Numer. Math.*, Vol. 6, pp. 123-139.

86. Ta'asan, S. and Nark, D. M., 1995 "An absorbing buffer zone technique for acoustic wave propagation" *AIAA* 95-0164.
87. Tam, C. K.W. and Morris, P. J., 1980 "The radiation of sound by instability waves of a compressible plane turbulent shear layer" *Journal of Fluid Mechanics*, Vol. 98, pt.2, pp. 349-381.
88. Tam, C. K. W., 1986 "On broadband shock associated noise" *Recent advances in Aeroacoustics*, Edited by Krothapalli, A. and Smith, C. A., Springer-Verlag, pp. 25-51.
89. Tam, C. K. W. and Webb, J. C., 1993 "Dispersion relation preserving schemes for computational acoustics" *Journal of Computational Physics*, Vol. 107, pp. 262-281, 1993.
90. Tam, C. K.W. and Dong, Z. 1994 "Wall boundary conditions for high-order finite difference schemes in computational aeroacoustics" *AIAA* 94-0457.
91. Tam, C. K.W., 1995 "Computational aeroacoustics issues and methods" *AIAA* 95-0677.
92. Tam, C. K. W. and Dong, Z, 1995 "Radiation and outflow boundary conditions for direct computation of acoustic and flow disturbances in a nonuniform mean flow" *CEAS/AIAA* 95-007.
93. Thompson, K. W., 1987 "Time-dependent boundary conditions for hyperbolic systems" *Journal of Computational Physics*, Vol. 68, pp. 1-24.
94. Thompson, K. W., 1990 "Time-dependent boundary conditions for hyperbolic systems II" *Journal of Computational Physics*, Vol. 89, pp. 439-461.
95. Trefethen, L.N., 1982 "Group velocity in finite difference schemes" *SIAM Review*, Vol. 24, No.2.
96. Troutt, T. R. and McLaughlin, D. K, 1982 "Experiments on the flow and acoustic properties of a moderate-Reynolds-number supersonic jet" *Journal of Fluid Mechanics*, Vol. 116, pp. 123-156.
97. Vichnevetsky, R., 1986 " Invariance theorems concerning reflections at numerical boundaries" *Journal of Computational Physics*, Vol. 63, pp. 268-282.
98. Viswanathan, K., Sankar, L. N. and Reddy, N. N., 1994 "A fluid/Acoustic coupled simulation of supersonic jet noise" *AIAA* 94-01347.
99. Viswanathan, K. and Sankar, L. N., 1995 "Toward the direct calculation of noise: Fluid/Acoustic coupled simulation" *AIAA Journal*, Vol. 33, No. 12, pp.2271-2279.
100. Wells, V. L. and Renaut, R. A., 1997 "Computed aerodynamically generated noise" *Ann. Rev. Fluid Mechanics*, Vol. 20, pp. 161-199.

VITA

Farouk Owis was born on September 1, 1966 in Egypt. He joined the Mechanical Engineering Department, Cairo University in 1983 where he earned his Bachelor's Degree with distinction in 1988. After graduation, he was appointed to the Aerospace Engineering Department, Cairo University as an administrator. He worked in the Propulsion Group with his advisor Prof. Ali Hashem. He received his Master's Degree from the same department in 1993. He earned a research assistantship at Old Dominion University to continue his Ph.D in August, 1995. Under the supervision of Prof. P. Balakumar, he started his Ph.D program in the Fluid Dynamics Group, Aerospace Engineering Department.

Currently, he occupies a postdoctoral position at Virginia Polytechnic Institute of Technology, Blacksburg, Virginia where he works closely with Prof. Ali Nayfeh and Prof. Dean T. Mook.